Université de Lille

UNIVERSITÉ DE LILLE

Doctoral school, **ED SMRE**
University Department **Laboratoire de Physique des Lasers, Atomes et Molécules (PhLAM)**

Thesis defended by

Corentin NAVEAU

on 11th October 2019

In order to become a Doctor from Université de Lille

Academic Field **Physics**
Speciality **Diluted Media and Optics**

Modulation instability and Fermi-Pasta-Ulam-Tsingou recurrences in optical fibres

Thesis supervised by	Arnaud MUSSOT	Supervisor
	Pascal SZRIFTGISER	Supervisor

Committee members

Referees	Hervé MAILLOTTE	Université de Franche-Comté - CNRS
	Benoît BOULANGER	Université Grenoble Alpes
Examiners	Camille-Sophie BRES	EPFL
	Stefano TRILLO	Università degli studi di Ferrara
	Matteo CONFORTI	Université de Lille - CNRS
President	Alexandre KUDLINSKI	Université de Lille
Supervisors	Arnaud MUSSOT	Université de Lille
	Pascal SZRIFTGISER	Université de Lille - CNRS

Université de Lille

UNIVERSITÉ DE LILLE

Ecole doctorale, **ED SMRE**
Unité de recherche **Laboratoire de Physique des Lasers, Atomes et Molécules (PhLAM)**

Thèse présentée par

Corentin NAVEAU

le 11 Octobre 2019

En vue de l'obtention du grade de docteur de l'Université de Lille

Discipline **Physique**
Spécialité **Milieux dilués et optique**

Instabilité de modulation et récurrences de Fermi-Pasta-Ulam-Tsingou dans les fibres optiques

Thèse dirigée par	Arnaud MUSSOT	Directeur
	Pascal SZRIFTGISER	Directeur

Composition du jury

Rapporteurs	Hervé MAILLOTTE	Université de Franche-Comté - CNRS
	Benoît BOULANGER	Université Grenoble Alpes
Examinateurs	Camille-Sophie BRES	EPFL
	Stefano TRILLO	Università degli studi di Ferrara
	Matteo CONFORTI	Université de Lille - CNRS
Président	Alexandre KUDLINSKI	Université de Lille
Directeurs de thèse	Arnaud MUSSOT	Université de Lille
	Pascal SZRIFTGISER	Université de Lille - CNRS

À mes parents,

Abstract: This work deals with the investigation of the modulation instability process in optical fibres and in particular its nonlinear stage. This process can induce a complex coupling dynamics between the pump and sidebands waves, with a single or multiple returns to the initial state if it is seeded. This phenomenon is referred as Fermi-Pasta-Ulam-Tsingou recurrences. In this thesis, we describe the implementation of a novel experimental technique based on heterodyne optical time-domain reflectometry and active compensation of losses. It allows fast and non-invasive distributed characterisation along a fibre of the amplitude and phase of the main frequency components of a pulse. Furthermore, we detail a simple post-processing method which enable us to retrieve the complex field evolution in the time domain. Using these tools, we reported the observation of two Fermi-Pasta-Ulam-Tsingou recurrences and their symmetry-breaking nature, both in the frequency and time domain. Then, we quantitatively studied the influence of the initial three-wave input conditions on the recurrence positions, in regards with recent theoretical predictions. Finally, we investigated the dynamics of higher-order nonlinear structures, namely second-order breathers.

Keywords: nonlinear fiber optics; modulation instability,
Fermi-Pasta-Ulam-Tsingou recurrences, breathers

Résumé: Ce travail porte sur l'étude du processus d'instabilité de modulation dans les fibres optiques et notamment son étape nonlinéraire. Ce procesus peut induire une dynamique complexe de couplage nonlinéaire entre une onde de pompe et des bandes latérales, notamment un, voire de multiples, retours à l'état initial si il est amorcé activement. Ce phénomène est connu sous le nom de récurrences de Fermi-Pasta-Ulam-Tsingou. Dans cette thèse, nous décrivons la mise en place d'un montage expérimental se basant sur la déctection hétérodyne d'un signal rétrodiffusé et une compensation active des pertes. Il permet une caractérisation distribuée rapide et non-invasive tout le long d'une fibre de l'amplitude et la phase des principales composantes spectrales d'une impulsion. En outre, nous détaillons une méthode de post-traitement qui nous permet de retrouver l'évolution du champ complexe dans le domaine temporel. Mettant en oeuvre ces outils, nous avons rapporté l'observation de deux récurrences de Fermi-Pasta-Ulam-Tsingou et leur brisure de symétrie, à la fois dans les domaines fréquentiel et temporel. Suite à cela, nous avons quantitativement examiné l'influence des conditions initiales des trois ondes envoyées dans la fibre sur la position des récurrences, en comparaison avec de récentes prédictions théoriques. Finalement, nous avons étudié la dynamique de structures nonlinéraies d'ordre supérieur, à savoir les breathers du deuxième ordre.

Mots-clés: optique nonlinéaire fibrée; instabilité de modulation; récurrences de Fermi-Pasta-Ulam-Tsingou, breathers

Remerciements

Je souhaite en premier lieu remercier Marc Douay, directeur du laboratoire PhLAM de l'Université de Lille, pour m'avoir permis d'effectuer cette thèse et veiller à son bon déroulement. J'y associe Majid Taki et Christian Focsa, respectivement ancien et actuel directeur d'études doctorales. Je souhaite aussi remercier Marc Lefranc concernant le co-financement de ma thèse par le Labex CEMPI.

Mes remerciements sont ensuite adressés aux membres du jury qui ont accepté d'évaluer mes travaux, tout d'abord les rapporteurs de cette thèse, Hervé Maillotte, directeur de recherche CNRS à l'Université de Franche-Comté et Benoît Boulanger, professeur à l'Université Grenoble Alpes (que je remercie également pour son excellent cours de physique des lasers, une des principales raisons pour laquelle je me suis ortienté vers l'optique nonlinéaire) ainsi que les examinateurs/trices Stefano Trillo, professeur à l'Université de Ferrara et Camille Sophie-Brès, professeure associée à l'EPFL.

Merci tout particulièrement à Arnaud Mussot et Pascal Szriftigser, qui ont encadré cette thèse ces trois dernières années et qui ont fait en sorte que je puisse travailler dans des conditions optimales, notamment matérielles, ce qui est crucial pour une thèse expérimentale (j'en profite pour remercier le personnel de l'atelier d'électronique, notamment Hervé et Michel, dont les réalisations ont été précieuses). Outre l'aspect matériel, je vous remercie de m'avoir accordé votre confiance, pour votre suivi au quotidien et vos encouragements. Vous avez toujours su me pousser à aller plus loin et j'ai énormément appris grâce à vous. Je remercie également Matteo Conforti et Alexandre Kudlinski pour leur disponibilté, étant toujours présents pour répondre à mes questions, aussi futiles soient-elles. Je souhaite aussi remercier Stefano Trillo pour l'ensemble des échanges que nous avons pu avoir, qui se sont toujours révélés enrichissants.

Un grand merci à Gilbert Martinelli, qui m'a offert la possibilité d'enseigner.

Mes remerciements sont ensuite dirigés vers l'ensemble de mes collègues du groupe Photonique pour la bonne ambiance reignant au travail et en particulier à l'équipe non-linéaire (aka Zobicon). Merci à Karim, qui ne peut désormais plus se "moquer" de mon statut de thésard ainsi qu'à Gang et Tomy pour tout ces moments passés ensemble, notamment les repas au RU et plus récemment à Guillaume. Je te souhaite bonne chance pour la suite ! Merci au vénérable François Copie, pour ses nombreux conseils mais surtout pour sa spectacualire mise en pratique sur des pommes du légendaire adage: "the thumbs are used for gripping, not for ripping" (Bob Mortimer). Un grand merci à Carlos Mas Arabí et Florent Bessin pour les moments passés au laboratoire, mais surtout en dehors à explorer la culture flamande, à savoir la bière et la carbonade ansi que le très mystérieux "triangle". Merci au Mac Ewan's qui nous a longtemps servi de QG.

Bien sûr, je n'oublie pas la reine du self-defense (et peut-être du char à voile, qui sait?) Maryna Kudinova ainsi que Madame la Présidente Marie Fournier.

Je remercie ensuite mes autres comparses Lillois. Merci à mes colocs de cette dernière année, Emilien, Marion (et Bérenger) et surtout Axelle pour sa cuisine "arrogante" et toutes nos discussions. Merci à Fabien, Amandine, Cécile, Valentin et Lysa pour ces mutilples soirées et friteries.

Vient le moment de remercier mes amis en dehors de Lille, que je ne peux pas tous nommer. Merci à Pichopi pour nos aventures celtiques. J'espère que nous continuerons à nous réunir autour d'une bonne vieille Guiness ! Mille mercis à Dylan, mon "cousin" et Clémentine, dont je suis fier d'être le "prinse sharman". J'ai maintenant hâte de témoigner ! Enfin, un grand merci à Léa pour les innombrables heures passées sur Skype, les séjours en Bretagne et les voyages (#Kúty).

Pour terminer je souhaite remercier l'ensemble des membres de ma famille pour leur éternel support et bienveillance. Un grand merci notamment à mon frère, ma belle-soeur, à ma nièce et filleule mais surtout à mes parents, qui n'ont jamais cessé de m'encourager à poursuivre mon propre chemin.

Contents

Acronyms and abbreviations

3WM three-wave mixing

AB Akhmediev breather

AO acousto-optic

AWG arbitrary wave generator

CW continuous wave

DC direct current

DOF dispersion oscillating fibre

DSF dispersion shifted fibre

EDFA erbium-doped fibre amplifier

FFT fast Fourier transform

FPUT Fermi-Pasta-Ulam-Tsingou

FSR free spectral range

FWHM full width at half maximum

FWM four-wave mixing

GVD group velocity dispersion

IM intensity modulator

ISO isolator

IST inverse scattering transform

KM Kuznetsov-Ma

LNA low-noise amplifier

MI modulation instability

MUX multiplexer

NLSE nonlinear Schrödinger equation

OSA optical spectrum analyser

OTDR optical time-domain reflectometry

PBS polarisation beam splitter

PC polarisation controller

PID proportional-integral-derivative controller

PM phase modulator

PS Peregrine soliton

RF radio frequency

SFB soliton on finite background

SMF single mode fibre

SOA semiconductor optical amplifier

SPM self-phase modulation

SVEA slow varying envelope approximation

TIR total internal reflection

XPM cross-phase modulation

ZDW zero-dispersion wavelength

Introduction

Since 1960 and the pioneered work of Theodore Maiman [1] (following the development of masers a few years earlier [2]) laser have revolutionised the field of nonlinear optics. Indeed they are able to deliver coherent light intense enough to impact the optical properties of the propagating medium, thus giving rise to nonlinear effects. As soon as 1961, Franken *et al* [3] were then able to demonstrate second-harmonic generation in a quartz crystal. Five years later, Kao and Hockam [4] highlighted the potential of glass waveguides for telecommunication purposes. Based on this work, physicists from Corning managed to fabricate "low-loss" optical fibres in 1970 [5]. Low-loss optical fibres were not only an interesting platform for telecommunication perspectives but also for nonlinear investigations. Indeed, they allow a high confinement of intense light over long distances, which is suitable to trigger nonlinear processes. The 70's decade revealed then to be very rich for nonlinear optics, with the observation by Stolen and coworkers of many fundamental nonlinear phenomena, namely Raman [6] and Brillouin scattering [7], Kerr effect [8], four-wave mixing [9, 10] and self-phase modulation [11].

During the 80's, the first observation in optical fibres of soliton propagation [12] and modulation instability [13] contributed to the development of ultra-sort pulses generation. Modulation instability (MI) consists in the exponential growth of spectral sidebands related to the perturbation on a continuous wave background [14]. It is not restricted to optical fibres and can appear in many other physical frameworks such as plasmas [15], Bose-Einstein condensates [16] or hydrodynamics [17]. In fibre optics it has found many applications, among which is parametric amplification [18]. MI can arise from noise but can also be coherently seeded. In the latter case, it presents a very interesting dynamics, in particular in its nonlinear stage. Indeed, it is accompanied by the amplification of multiple harmonics of the modulation sidebands via four-wave mixing, leading eventually to a triangular shape

spectrum [19]. In the time domain, this corresponds to a train of high-amplitude pulses. However, the process can further reverse, leading the system back to its initial state. This phenomenon, which can be periodic or quasi-periodic is often referred as Fermi-Pasta-Ulam-Tsingou (FPUT) recurrence. To understand the origin of this name, one has to go back to the mid 50's. Back then, in Los Alamos, four researchers, Enrico Fermi, John Pasta, Stanislaw Ulam and Mary Tsingou were aiming to numerically investigate the behaviour of a chain of mechanical oscillators with nonlinear couplings between them. Little they knew that their work would pave the way for a revolution of the broad field of nonlinear science [20]. Starting their simulations with the excitation of a single mode of the system, they intended to study how the energy would transfer from the initial mode to higher-order ones, eventually reaching an equirepartition of the energy between all the possible modes. However, they observed something completely different: *"Let us say here that the results of our computations show features which were, from the beginning, surprising to us....Instead of gradual increase of all the higher modes, the energy is exchanged, essentially, among only a certain few. It is, therefore, very hard to observe the rate of "thermalization" or mixing in our problem, and this was the initial purpose of the calculation."* [21]. Indeed, they observed after a short time that almost all the energy flowed back into the initial mode, the system almost coming back to its initial state. Published in an internal report in 1955 [21], their results would acquire a great importance only ten years later. Indeed, in an extension of this work and in an attempt to explain this recurrent process, Zabusky and Kruskal introduced in 1965 [22] a solution of nonlinear equations that can maintain its form along time, which they named "soliton". Since then, the FPUT recurrence process have especially been investigated for his role in chaos [23] and for its relation with the nonlinear stage of MI, in the framework of nonlinear systems whose dynamics can be described by the nonlinear Schrödinger equation. In particular, it led to the development of breathers theory [24], which play an important role in the emergence of rogue waves [25–29] and the generation of supercontinuum [30].

Although MI have been observed in optical fibres in the mid-80's [13], the observation of FPUT recurrence in optics was only reported in 2001 by Van Simaeys and coworkers [31]. In fact, observing such recurrence is not so easy. It has previously be done in a few physical settings such as hydrodynamics [32] and electric transmission line [33]. One of the most limiting factor is dissipation, which progressively kills

the recurrent process, even in optical fibre with very low linear attenuation (<0.2 dB/km at 1.55 μm). Moreover, one has to propagate long enough for the recurrence to happen, but the propagation is often affected by detrimental effects such as stimulated Brillouin scattering [34] in optical fibres. The solution found by Van Simaeys was to launch at the input of a fibre an initial weakly modulated pump wave (to seed the MI process and trigger FPUT recurrences, the optical Fourier modes playing the same role than the mode of vibrations of the oscillators chain from the original experiment) but to operate in a quasi-CW regime by using square pulses, in order to mitigate SBS. Via an indirect measurement method they were then able to characterise one recurrence, which attracted a lot of attention from the nonlinear science community [35].

Nowadays, most experimental investigations on FPUT recurrences and breathers occurs in hydrodynamics with experiments in water tank [36, 37] and nonlinear optics [28, 38–41], in particular in fibre optics experiments. Indeed, fibres constitute a suitable testbed for the investigation of such processes as they offer an easy tuning of initial conditions and control of fibre parameters. However, conversely to water tank experiments for which there is no intrinsic difficulty to perform distributed measurements of the complex amplitude of the field of the waves, it is far more complicated to get insights on the dynamics taking place when light propagate along a fibre, in particular on the phase. The work presented in this thesis focused then on the implementation of a novel experimental setup allowing a non-invasive distributed characterisation of the amplitude and phase of the main frequency components of a pulse. Based on this, we report in particular the characterisation of multiple FPUT recurrences and breather propagation in optical fibres.

The present manuscript is divided in 6 chapters, followed by two appendices. Chapter 1 provides a brief overview of the main linear and nonlinear effects experienced by light along the propagation, ending up with the introduction of the nonlinear Schrödinger equation. In Chapter 2, we discuss more in depth the original Fermi-Pasta-Ulam-Tsingou problem and then the theory of modulation instability. In particular, we consider two models to describe the nonlinear stage of MI, namely the three-wave mixing model and the Akhmediev breather theory and introduce the phase-plane configuration that we are going to use all along this thesis. Chapter 3 is dedicated to the implementation and description of an experimental setup that allows to characterise FPUT recurrences and breather propagation. Using this setup,

we report in Chapter 4 the first experimental observation of two FPUT recurrences in optical fibres, as well as their symmetry-breaking nature, both in the frequency and time domain [42, 43]. We particularly emphasise the conditions inducing separatrix crossing. In Chapter 5, we characterise quantitatively the impact of the input modulation sidebands amplitude and relative phase (compared to the pump) on the first two recurrence positions [44]. The results are compared with recent analytical predictions developed by Grinevich and Santini [45]. Whereas Chapter 4 and 5 were related to first-order breathers, we focused in Chapter 6 on second-order breathers, their control, and their distributed characterisation. In Appendix A, we recall the exact first-order breather solutions of the nonlinear Schrödinger equation originally derived by Akhmediev *et al* [24]. Finally, we describe in Appendix B a new experimental setup which enables the round-trip to round-trip characterisation in amplitude and phase of seeded modulation instability in passive optical fibre-ring cavities.

Chapter 1

Generalities on light propagation in optical fibres

Contents

The aim of this chapter is to list and describe briefly the main phenomena involved in the propagation of light in an optical fibre and encountered during this PhD thesis. In the first section, we will discuss the guiding mechanism. Then, the second and third sections will introduce the main linear and nonlinear effects, respectively, which affect the propagation of light waves. Finally, we will end up in the last section with the equation allowing the description of the propagation dynamics, namely the nonlinear Schrödinger equation.

1.1 Guiding mechanism in optical fibres

An optical fibre is a dielectric waveguide, usually made of fused silica and composed of a core surrounded by a cladding. Thanks to the use of dopants, the refractive index can be modified in order to get a refractive index of the core slightly higher than the one of the cladding. Light can then propagate inside the core via total internal reflection (TIR) [46]. This type of fibre, which presents cylindrical symmetry, is commonly referred as step-index fibres. Depending on the core diameter, the wavelength of the light and the refractive index of the core and the cladding, they can support one or several transverse modes [47]. In this manuscript the fibre used for all the experiments is a standard SMF-28 fibre for which the propagation is single-mode at 1.55 μm.

1.2 Linear effects

1.2.1 Linear attenuation

The losses that affect the propagation can mainly find their source in two phenomena : molecular absorption, especially from OH ions [48] and Rayleigh scattering. Rayleigh scattering results from small inhomogeneities in the propagating medium. The propagating field can induce a polarisation of the electronic cloud of these inhomogeneities by transferring some of its energy which is then retransmitted isotropically. A part of the scattered waves co-propagates then with the original propagating field while the other part is either not guided (as it does not fulfill the condition for TIR) or contra-propagates, which explains the losses. Though it is at first detrimental for almost all applications, the backscattering gives actually rise to many interesting applications among which is optical time-domain reflectometry (OTDR) [49]. OTDR will be the basis of the experimental setup described in Chapter 3. Indeed, the analysis of the backscattered wave allows to perform distributed characterisation of the propagating wave as their power are directly proportional so one can write $P_{BS} = B \times P_{in}$ where P_{BS} is the power of the backscattered wave, P_{in} is the input power and B is the Rayleigh backscattering factor. (see Ref. [50] for an explicit relation between the parameter B and the parameters of the fibre and light). For a SMF-28 from Corning [51], $B = -82\,dB$ at 1.55 μm for a 1 ns incident pulse.

To give a more precise illustration, in the experiments presented in this manuscript we will use 50 ns pulses and $P_{in} \backsimeq 450\,mW$, which gives $P_{BS} \backsimeq 140\,nW$.

In a SMF-28 fibre, the minimum of losses is located around 1.55 µm. The global losses of the fibre are usually expressed in the form of a coefficient α, called linear attenuation and calculated using the following relation : $P_{out} = P_{in} exp\,(-\alpha L)$ with P_{out} the output power, and L the length of the fiber. In our case $\alpha \backsimeq 4.6 \times 10^{-5} m^{-1}$ or 0.2 dB/km (the lowest recorded linear attenuation in a single mode silica fibre is, to date, 0.142 dB/km [52]).

1.2.2 Chromatic dispersion

When an electromagnetic wave propagates inside a dielectric medium, the refractive index n usually depends on the angular frequency of the light ω. This effect is called chromatic dispersion. As the different spectral components of a polychromatic wave experience their own refractive index, they do not travel at the same velocity, which leads to distortions of the wave shape. This effect is usually taken into account by means of the propagation constant $\beta(\omega)$ expanded as a Taylor series around the carrier angular frequency ω_0:

$$\beta(\omega) = \frac{\omega}{c} n(\omega) = \beta_0 + \beta_1 (\omega - \omega_0) + \frac{\beta_2}{2} (\omega - \omega_0)^2 + \frac{\beta_3}{3!} (\omega - \omega_0)^3 + ... \tag{1.1}$$

where

$$\beta_k = \left(\frac{d^k \beta}{d\omega^k} \right)_{\omega = \omega_0} (k = 0, 1, 2, 3...) \tag{1.2}$$

β_1 corresponds to the inverse of the group velocity and β_2 to the group velocity dispersion (GVD). Two types of regimes can be defined in relation to the sign of the GVD. If the GVD is positive, short wavelengths travel slower than long wavelengths and the dispersion regime is called normal while, if it is negative, short wavelengths travel faster than long wavelengths and the regime is called anomalous. The wavelength for which the GVD is zero is referred as the zero-dispersion wavelength (ZDW). In SMF-28 it is around 1.3 µm [51] but it can be tuned from the visible to the infrared by using in particular different structures of fibres [53, 54]. At 1.55 µm, which is the wavelength around which we will work later on, $\beta_2 \backsimeq -19 \times 10^{-27} s^2/m$ so we are in the anomalous regime. The main impact of GVD is the temporal broad-

ening or compression of optical pulses, which is for example used in chirped pulse amplification [55].

1.3 Nonlinear effects

1.3.1 The Kerr nonlinearity

The interaction of light with the dielectric medium induces a polarisation described by the polarisability vector **P** (bold letters refer to vectors) which can be expressed as power series of the electric field **E**:

$$\mathbf{P} = \epsilon_{\mathbf{0}}(\chi^{(1)} \cdot \mathbf{E} + \chi^{(2)} \cdot \mathbf{EE} + \chi^{(3)} \cdot \mathbf{EEE} + ...) \tag{1.3}$$

where ϵ_0 is the vacuum permitivity and $\chi^{(k)}$ is the k-th order susceptibility. The first-order term is related to the refractive index of the medium via the relation $n(\omega) = \sqrt{1 + Re(\chi^{(1)}(\omega))}$ and does account for the linear propagation. When the light intensity is high enough, one has to take into account higher-order terms into the polarisability expression. In optical fibres made of fused silica, the second-order susceptibility $\chi^{(2)}$ vanishes due to the centro-symmetry of the medium and the expansion of the polarisabilty can be stopped at the third-order term, since higher-order terms are usually negligible. The third-order susceptibility will in particular induce a dependence of the refractive index on the light intensity such as $n(\omega) = n_L + n_2 |E|^2$ with n_L the linear refractive index introduced previously and n_2 the nonlinear refractive index which can be expressed as $n_2 = \dfrac{3Re(\chi^{(3)}(\omega))}{8n_L}$. For silica fibres $n_2 \backsimeq 2.6 \times 10^{-20}\, m^2/W$ [47]. The intensity-dependence of the refractive index is commonly referred as Kerr effect. In optical fibres, the strength of the Kerr effect can be evaluated via the nonlinear coefficient defined as $\gamma = n_2\omega_0/cA_{eff}$ where c is the light velocity in vacuum and A_{eff} is the effective area of the transverse mode. For SMF-28, $\gamma = 1.3/W/km$ and $A_{eff} = 80\,\mu m^2$. Note that γ three-order of magnitude higher can be obtained in microstructured fibres or fibres with other types of materials [47]. Several phenomena result from Kerr effect such as self-phase modulation (SPM), cross-phase modulation (XPM) and four-wave mixing (FWM) [47]. These processes will be discussed in the next chapter.

1.3.2 Raman scattering

Raman scattering (from the name of Chandrashekhara Venkata Râman, who was the first to highlight the process in 1928 [56]) is an inelastic scattering process which results from the interaction of an electromagnetic wave and the vibration modes of the molecules of the structure in which it propagates. Its first experimental observation in optical fibres was reported in 1972 by Stolen *et al*. [6]. To get a clear understanding of the process one can look at it from a quantum mechanical point of view, as illustrated in Fig. 1.1(a). First, a pump photon ω_p excites a virtual state. Then it decays to a vibrational state of silica by emitting a signal photon ω_S and the system goes back to the ground state by emitting a phonon Ω_R. For energy conservation, the signal photon has then a frequency $\omega_s = \omega_p - \Omega_R$ lower than the pump photon. It can extend over more than 40 THz (relatively to the pump photon frequency) because of the amorphous nature of silica which leads to a continuum of vibrational state rather than discrete levels of energy as usually encountered in crystals, gazes or liquids. The gain associated to Raman scattering for amorphous silica is displayed in Fig. 1.1(b) and presents a maximum for a frequency detuning of -13.2 THz. Note that compared to the Kerr effect which is considered as instantaneous, Raman scattering is a retarded effect, with a typical timescale of 60 fs [47]. The use of Raman scattering to provide distributed amplification along an optical fibre, a technique commonly used in telecommunication optics [57], will be discussed in Chapter 3.

1.4 The nonlinear Schrödinger equation

Under the assumption of the slowly varying envelope (SVEA), which means that the spectral bandwidth $\Delta\omega$ of a signal is very small compared to the carrier frequency ω_0, one can derive from Maxwell equations an equation describing the propagation evolution of the field envelope E which accounts for all the effects, linear and nonlinear, described previously. This equation is called extended nonlinear Schrödinger equation and reads [47]:

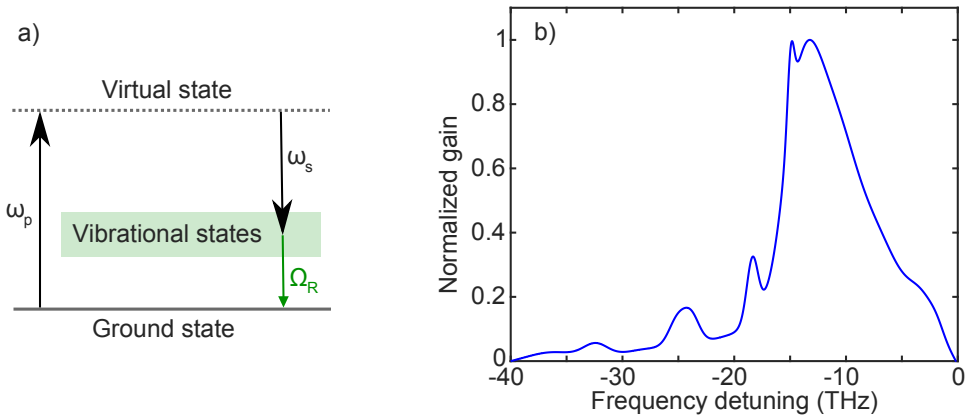

Figure 1.1: Raman scattering. (a) Energy diagram of the Raman scattering process. (b) Gain (normalised to its maximum) associated to the process (from the data of Ref. [58]).

$$\frac{\partial E\left(z,T\right)}{\partial z}=i\sum_{k\geqslant 2}^{\infty}i^{k}\frac{\beta_{k}}{k!}\left(\frac{\partial^{k}E\left(z,T\right)\right)}{\partial T^{k}}\Bigg)-\frac{\alpha}{2}E(z,T)+i\gamma E(z,T)\int R(T')\left|E(T-T')\right|^{2}dT' \tag{1.4}$$

where $T=t-\beta_1 z$ is the time defined in the reference frame traveling at the group velocity $1/\beta_1$ of the carrier frequency, the time t being the reference frame of the laboratory. The first term of the right-hand side of equation (1.4) corresponds then to chromatic dispersion, the second one to the linear attenuation and the last one to nonlinear effects, with $R(T)$ the nonlinear response of the fibre (it includes both the Kerr and Raman effects). Note that others terms can still be added to this equation to described effects such as self-steepening [47], which accounts for the intensity dependence of the dispersion for ultra-short pulses. Equation (1.4) can be reduced to a simpler form under several assumptions [47]. First, if the width of the pulse is larger than 5 ps, Raman effect can be neglected. Secondly, if the pulse does not propagate in the vicinity of the ZDW, higher-order dispersion terms can be removed. Finally, for short propagation distance or if the losses are compensated in a distributuve way (as we will see in Chapter 3) the linear attenuation can also be removed. The propagation equation is then called the nonlinear Schrödinger equation (NLSE) and only accounts for group velocity dispersion and Kerr effect :

$$\frac{\partial E}{\partial z} = -i\frac{\beta_2}{2}\frac{\partial^2 E}{\partial T^2} + i\gamma |E|^2 E \tag{1.5}$$

Equation (1.5) is one of the most ubiquitous equation in physics as it models part of the dynamics in many fields of physics such as plasma, cold atoms, hydrodynamics or nonlinear optics (see Ref. [28] for the optical-ocean analogy). Although it presents analytical solutions (which will be discussed in chapter 2), it is commonly solved numerically using the split-step Fourier method, which is easy to implement [47]. It consists in solving the equation in different steps, one accounting only for the linear effects in the frequency domain and the other one for the nonlinear effects in the time domain. All the numerical integration of equation (1.5) reported in this dissertation have been performed using this method.

Chapter 2

Basic concepts of Fermi-Pasta-Ulam-Tsingou recurrences in optical fibres

Contents

In this chapter we describe the process referred as Fermi-Pasta-Ulam-Tsingou (FPUT) recurrences, from the names of its first investigators [59]. This process depicts the ability of a multimodal nonlinear system to come back to its initial state after experiencing complex coupling dynamics, exhibiting multiple recurrences or a quasi-periodic behavior. In the first section we will briefly report the story of the discovery of this famous effect and highlight its importance in nonlinear physics. In optics, this recurrent process can be triggered by an ubiquitous nonlinear phenomenon called modulation instability (MI) [14]. Hence, the second section of

this chapter will introduce and discuss in the framework of the NLSE the theoretical tools which allow to describe this MI process. Note that the formulas reported here have already been reported in the literature and do not constitute an original study from the author. Finally, we will discuss in the last section the impact of several parameters on the recurrent process such as noise and linear attenuation.

2.1 Historical context and universal nature of Fermi-Pasta-Ulam-Tsingou recurrence process.

The study of FPUT recurrences finds its origin in a numerical experiment performed by Enrico Fermi, John Pasta, Stanislaw Ulam and Mary Tsingou in 1953 in Los Alamos, USA, for which results have been reported in 1955 in an internal report [21, 60]. Using one of the first computer called MANIAC (for MAthematical Numerical Integrator And Computer, originally designed for the H-bomb development), the aim of their work was to investigate the long term evolution of a linear system perturbed by a weak nonlinear perturbation with the expectation to observe a progressive equirepartition of energy among the modes of the system. Note that this equirepartition will also be referred later as thermalisation. As a system, they choose a finite chain of 16, 32 or 64 elements linked by springs and fixed at its extremities. The force between two neighbour elements consists in the classic force linked to linear displacement and a weak higher-order term which could be quadratic, cubic or take a more complex form (the equations can be found in Ref. [21]). The initial condition for the simulation was either the first mode or a combination of a few low-order modes, (note that the modes we referred to correspond to the base of stationary solution of the linear problem thanks to which one can describe the vibration of the string) and the computing time was chosen to be far greater than the characteristic period of the first mode. If we look at the cubic problem (the conclusions are similar for other types of nonlinearities), which implies a third-order nonlinearity (such as the Kerr nonlinearity) the observations were the following. At the beginning, the energy of the first mode gradually decreases while the energy of higher-order modes increases, which was expected. But, after a certain time, the energy of these higher-order modes is no longer increasing. Instead, it starts to flow back into the first mode, which almost recover its initial energy. As stated by the

authors, this phenomenon was "surprising". Indeed, the dynamic involved only a small number of modes and the system almost recover its initial state (which we will call recurrence) instead of reaching thermalisation. This is the reason why this phenomenon has been for a long time called a paradox. This original problem being still investigated today, it was recently shown that the expectations of the authors were not totally wrong, the system will experience recurrences or quasi-periodic behaviour but will in fact reach thermalisation after a long time due to discrete six-waves resonant interactions [61, 62].

While the FPUT experiment confirmed the potential of numerical experiments, it also has had a profound impact on nonlinear physics [20, 23]. Indeed it triggered many works, the most famous being probably the theory of solitons in plasma by Zabusky and Kruskal [22] which is one of the pillar of nonlinear science. Furthermore, analogs of FPUT recurrences can be observed in a large range of physical frameworks and not only in mechanical systems, which explains why the process is often described as universal. For example FPUT recurrences play a role in electric transmission line [33], hydrodynamics [32,37], nematic liquid crystals [63], bulk photorefractive crystals [64] and nonlinear optical fibres [31, 38, 65–67] to name a few. In optics, which is our field of interest, its first experimental observation is quite recent, as it was reported in 2001 by Van Simaeys *et al* [31, 35, 65] in the context of modulation instability in optical fibres. In fact, when such an instability is seeded, FPUT recurrence cycles of amplification and back-conversion can occur. In the next section we will then focus on the theory of MI.

2.2 Theory of the linear stage of modulation instability

Modulation instability (or Benjamin-Feir instability) is an ubiquitous phenomenon which consists in the exponential growth of spectral sidebands related to the perturbation on a CW background [14]. This process has been studied and observed in various physical frameworks such as plasma physics [15], hydrodynamics [17], Bose-Einstein condensates [16], optics and many others, the first observation in fibre optics being reported in 1986 [13]. In systems described by the NLSE, the MI process can be investigated by performing a linear stability analysis of a perturbed

steady-state solution of the NLSE such as :

$$E = (\sqrt{P_p} + \epsilon) exp(i\gamma P_p z) \tag{2.1}$$

where P_p is the input pump power and $\epsilon = \epsilon_1 + i\epsilon_2$ with $|\epsilon|^2 \ll P_p$. By injecting (2.1) in (1.5), linearising in ϵ and identifying the real and the imaginary parts one obtains the following system of two coupled equations :

$$\frac{\partial \epsilon_1}{\partial z} = \frac{\beta_2}{2} \frac{\partial^2 \epsilon_2}{\partial T^2} \tag{2.2a}$$

$$\frac{\partial \epsilon_2}{\partial z} = -\frac{\beta_2}{2} \frac{\partial^2 \epsilon_1}{\partial T^2} + 2\gamma P_p \epsilon_1 \tag{2.2b}$$

In the frequency domain, this system can then be rewritten in the following matrix form :

$$\frac{d}{dz} \begin{pmatrix} \hat{\epsilon}_1 \\ \hat{\epsilon}_2 \end{pmatrix} = \begin{pmatrix} 0 & -\frac{\beta_2}{2}\Omega^2 \\ \frac{\beta_2}{2}\Omega^2 + 2\gamma P_p & 0 \end{pmatrix} \begin{pmatrix} \hat{\epsilon}_1 \\ \hat{\epsilon}_2 \end{pmatrix} \tag{2.3}$$

where $\hat{\epsilon}_{1,2}$ correspond to the Fourier transforms of $\epsilon_{1,2}$ and Ω is the angular frequency shift relative to the pump angular frequency. The eigenvalues of the matrix (2.3) read as :

$$K = \pm \sqrt{\frac{\beta_2}{2}\Omega^2 \left(\frac{\beta_2}{2}\Omega^2 + 2\gamma P_p \right)} \tag{2.4}$$

K is the propagation constant of the weak perturbation at angular frequency $\pm\Omega$ such as

$$\epsilon = A \times exp[i(Kz - \Omega T)] + B \times exp[-i(Kz - \Omega T)] \tag{2.5}$$

where A and B are real constants. We then introduce the parametric gain $g(\Omega) = 2Im(K)$. Looking at equation (2.4) one can see that K is always real for $\beta_2 > 0$ which means $g(\Omega) = 0$. Thus, in the normal dispersion regime, a continuous wave is stable. For $\beta_2 < 0$ (anomalous regime), K is purely imaginary for $\Omega^2 < \Omega_c^2 = 4\gamma P_p / |\beta_2|$ and a continuous wave is said to be modulationally unstable. Figure 2.1 shows the MI

gain spectrum for $P_p = 450\,mW$, $\beta_2 = -19 \times 10^{-27} s^2/m$ and $\gamma = 1.3 \times 10^{-3}/W/m$ (typical parameters of our experiments in a SMF-28 at $1.55\,\mu m$). This spectrum is symmetric relatively to the pump frequency and reaches its maximum $g_{max} = 2\gamma P_p$ at $\Omega_{max} = \pm\sqrt{2\gamma P_p/|\beta_2|} = \pm\Omega_c/\sqrt{2}$. The latter relation can also be written in the form $\frac{1}{2}\beta_2\Omega_{max}^2 + 2\gamma P_p = 0$ which corresponds to a phase-matching relation between the linear phase due to dispersion and the nonlinear one due to the Kerr effect. Thus, the maximum gain is obtained when the linear term is perfectly compensated by the nonlinear one. Very high gain (up to 70 dB [68]) or very broadband gain (more than $100\,nm$ [18, 69, 70]) has been demonstrated in optical fibres using this process (also called degenerate three modes parametric instability).

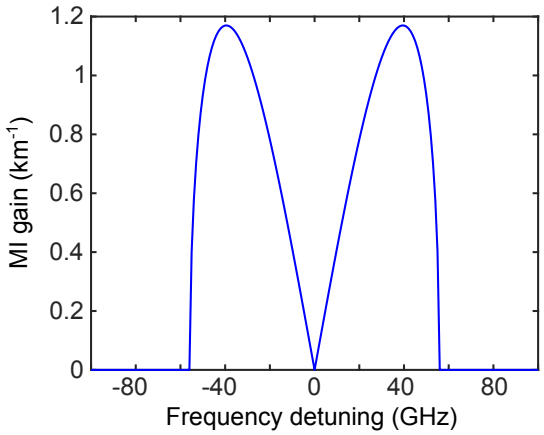

Figure 2.1: Gain spectrum of modulation instability. Parameters: $P_p = 450\,mW$, $\beta_2 = -19 \times 10^{-27} s^2/m$ and $\gamma = 1.3 \times 10^{-3}/W/m$.

While we limited ourselves to the simple case of a system described by the pure NLSE and in the anomalous dispersion regime, MI can also occur in different configurations, even in the normal dispersion regime. In this case, it is necessary to add a degree of freedom in order to fulfill the phase-matching condition. This can be done for example by operating near the ZDW and accounting for a negative fourth-order dispersion [71], by using the birefringency of fibres [72], by modulating longitudinally the dispersion profile of the fiber [73] or by using properties of multimode fibres such as the self-imaging [74] or the dispersion of the waveguide modes [10].

We have detailed here the linear stage of MI where the pump wave is undepleted and have shown that a seed at angular frequency $|\Omega| < \Omega_c$ will experience gain. However, this growth cannot obviously be unlimited, the process starting to saturate

when the seed power is no longer negligible compared to the pump power. The process then enters its nonlinear stage.

2.3 Theory of the nonlinear stage of modulation instability

The nonlinear stage of MI is illustrated by the false color plots in Figs. 2.2(a,b) which represent the spatio-temporal [Fig. 2.2(a)] and spatio-spectral [Fig. 2.2(b)] power evolutions of the field of a modulationally unstable wave for which the MI process is seeded by symmetrical sidebands (called signal for the higher-frequency one and idler for the lower-frequency one) set 20 dB below a 450 mW pump at frequencies $\pm f = \pm 35\,GHz$ (note that f corresponds to the frequency detuning and is simply related to Ω via the relation $f = \Omega/(2\pi)$), which is slightly lower than the maximum gain frequency $f_{max} = 40\,GHz$ (note that the input phase of each of the three spectral components is zero). Theses evolutions are obtained by numerically integrating the NLSE with the method described in Chapter 1. We can clearly see in the frequency domain that harmonics of the modulation sidebands (falling out of the MI gain range) appear very early in the propagation due to degenerate four-wave mixing (FWM) and that the pump power depletes, becoming even smaller than the the first and second-order sidebands around about 5 km. This discrete spectral broadening leads to a train of very short pulses in the time domain. By further propagating, we observe a return to the initial state (i.e. three-wave in the frequency domain and a weakly modulated pump wave in the time domain) before the process starts to reiterate which confirms the previous stated fact that seeded MI can induce several FPUT recurrence cycles. In this section, we will discuss several models allowing the description of this behaviour. First, we will introduce a truncated three-wave mixing (3WM) model [75, 76].

2.3.1 The three-wave mixing model

Derivation of the model

If the MI process is seeded at an angular frequency Ω such as $\frac{\Omega_c}{2} < \Omega < \Omega_c$, only the signal and idler sidebands will experience modulation instability gain, their

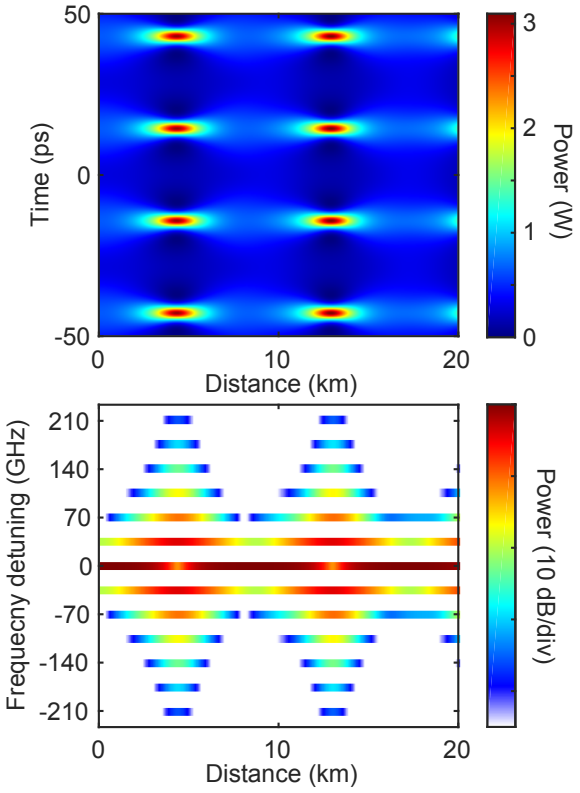

Figure 2.2: (a) Spatio-temporal and (b) spatio-spectral evolution of a modulationally unstable wave. Parameters: $P_p = 450\ mW$, $\beta_2 = -19 \times 10^{-27} s^2/m$, $\gamma = 1.3 \times 10^{-3}/W/m$, $f = 35 GHz$ and the initial signal/idler (symmetric sidebands) to pump ratio is -20 dB.

harmonics (which appears because of subsequent FWM) falling out the MI gain range. Hence, it is worth to derive a truncated model accounting only for the pump, signal and idler waves such as the total electric field can be written as the following ansatz :

$$E(z) = E_p(z) + E_s(z) exp\,(i\Omega T) + E_i(z) exp\,(-i\Omega T) \tag{2.6}$$

where the subscripts p, s, i denote for the pump, signal and idler, respectively, the signal and idler waves being detuned by an angular frequency $\pm\Omega$ compared to the pump. By substituting equation (2.6) in the NLSE (1.5) one obtains a set of three coupled equations :

$$\begin{aligned}
\frac{dE_p}{dz} &= \gamma\left[|E_p|^2 + 2\left(|E_s|^2 + |E_i|^2\right)\right]E_p + 2\gamma E_s E_i E_p^* \\
\frac{dE_s}{dz} &= i\frac{\beta_2}{2}\Omega^2 E_s + \gamma\left[|E_s|^2 + 2\left(|E_p|^2 + |E_i|^2\right)\right]E_s + 2\gamma E_p^2 E_i^* \\
\frac{dE_i}{dz} &= i\frac{\beta_2}{2}\Omega^2 E_i + \gamma\left[|E_i|^2 + 2\left(|E_p|^2 + |E_s|^2\right)\right]E_i + 2\gamma E_p^2 E_s^*
\end{aligned} \tag{2.7}$$

The first term on the right-hand side of the second and third equation of the system is related to the GVD, the second term between square bracket is responsible for SPM and XPM while the last term accounts for the exchange of energy between the waves. By introducing the pump, seed and idler power $P_{p,s,i} = |E_{p,s,i}|^2$and nonlinear phase $\varphi_{p,s,i}$ such as $E_p(z) = \sqrt{P_p(z)}exp(i\varphi_p(z))$, $E_s(z) = \sqrt{P_s(z)}exp(i\frac{\beta_2}{2}\Omega^2 z + i\varphi_s(z))$, $E_i(z) = \sqrt{P_i(z)}exp(i\frac{\beta_2}{2}\Omega^2 z + i\varphi_i(z))$ the previous set of equations can be rewritten:

$$\begin{aligned}
\frac{dP_P}{dz} &= 4\gamma P_p\sqrt{P_s P_i}sin(2\Delta\Phi) \\
\frac{dP_s}{dz} &= -2\gamma P_p\sqrt{P_s P_i}sin(2\Delta\Phi) \\
\frac{dP_i}{dz} &= -2\gamma P_p\sqrt{P_s P_i}sin(2\Delta\Phi) \\
\frac{d\Delta\Phi}{dz} &= -\frac{1}{2}\left[\beta_2\Omega^2 + \gamma(2P_p - P_s - P_i) + \gamma\left[P_p\sqrt{\frac{P_i}{P_s}} + P_p\sqrt{\frac{P_s}{P_i}} - 4\sqrt{P_s P_i}\right]cos(2\Delta\Phi)\right]
\end{aligned} \tag{2.8}$$

where the relative phase $\Delta\Phi$ reads:

$$\Delta\Phi = \frac{1}{2}\left[2\varphi_p - \varphi_s - \varphi_i - \beta_2\Omega^2 z\right] \tag{2.9}$$

If we consider symmetric sidebands initially then $\Delta\Phi = \varphi_p - \varphi_s - \frac{1}{2}\beta_2\Omega^2 z$ and $\Delta\Phi_{init} = \Delta\Phi(z=0) = \varphi_p - \varphi_s$. Furthermore, if necessary, the fibre losses can be taken into account by including the terms $-\alpha P_p$, $-\alpha P_s$ and $-\alpha P_i$ in the right-hand side of the first, second and third equation of the system (2.8), respectively. One can clearly notice the crucial role played by $\Delta\Phi$, which is at the core of important applications such as phase-sensitive parametric amplification [18, 77, 78]. Noteworthy, $sin(2\Delta\Phi_{init}) < 0$ implies that the system starts with parametric amplification of the seeds and attenuation of the pump whereas $sin(2\Delta\Phi_{init}) > 0$ implies the

opposite. Moreover, the second and third equations give that the maximum growth rate of the seeds is obtained for $\Delta\Phi_{init} = -\pi/4$. In this case, the last equation of the system (2.8) reads:

$$\frac{\Delta\Phi}{dz} = -\frac{1}{2}\left[\beta_2\Omega^2 + \gamma(2P_p - P_s - P_i)\right] \approx -\frac{1}{2}\left[\beta_2\Omega^2 + 2\gamma P_p\right] \tag{2.10}$$

by assuming $P_{s,i} \ll P_p$ (which is a relevant assumption over a short distance if the sidebands are initially weak compared to the pump). Hence, to keep a constant $\Delta\Phi = -\pi/4$, the angular frequency detuning has to be $\Omega = \pm\sqrt{2\gamma P_p/\left|\beta_2\right|}$, which corresponds to Ω_{max} derived in the previous section (2.2), for which the modulation instability gain is maximum.

This set of four coupled equations can easily be solved numerically. Examples of the power and relative phase evolutions are displayed in Fig. 2.3, with the following parameters (close to those used in experiments): $P_p = 450\ mW$, $\beta_2 = -19 \times 10^{-27} s^2/m$, $\gamma = 1.3 \times 10^{-3}/W/m$, initial signal/idler to pump ratio of -20 dB, $f = 35GHz$ and $\Delta\Phi_{init} = 0$ for Figs. 2.3(a-d) and $\Delta\Phi_{init} = -\pi/2$ for Figs. 2.3(e-h). Figs. 2.3(a,e) show the relative (compared to the total power) pump (blue line) and signal (red line) power evolutions and Figs. 2.3(c,g) their relative phase evolutions. Moreover, the black lines and the right vertical axis in Figs. 2.3(c,g) correspond to the sign of $sin(2\Delta\Phi)$. Looking at the power evolutions, we can clearly observe the exchange of energy between the pump and the signal waves and the correlation of the direction of this energy flow with the sign of $sin(2\Delta\Phi)$. Three recurrences in power can be observed for the two cases but it is in particular interesting to point out that, while the power evolutions seem very similar, their corresponding relative phase evolutions are drastically different, the first one exhibiting growth and decreasing in the range of $[-\frac{\pi}{4}, -\frac{\pi}{4}]$ while the second one is only increasing and span the entire $[0, 2\pi]$ range. This difference is outlined by looking at the evolution in the phase plane $(\eta_s cos(\Delta\Phi), \eta_s sin(\Delta\Phi))$ where $\eta_s = P_s/P_0$ with $P_0 = P_p + P_s + P_i$ the total power. Thus, in the case where $\Delta\Phi_{init} = 0$, we notice that the trajectory stays on one side of the plane and presents a single loop orbit while for the other case we observe a double loop orbit, the trajectory going on both sides of the phase-plane. This difference in phase-plane trajectories can also be observed by plotting the spatio-temporal evolution obtained by numerically integrating the NLSE [Fig. 2.3(d,h)]. We observe recurrences for both cases, the initially modulated continuous

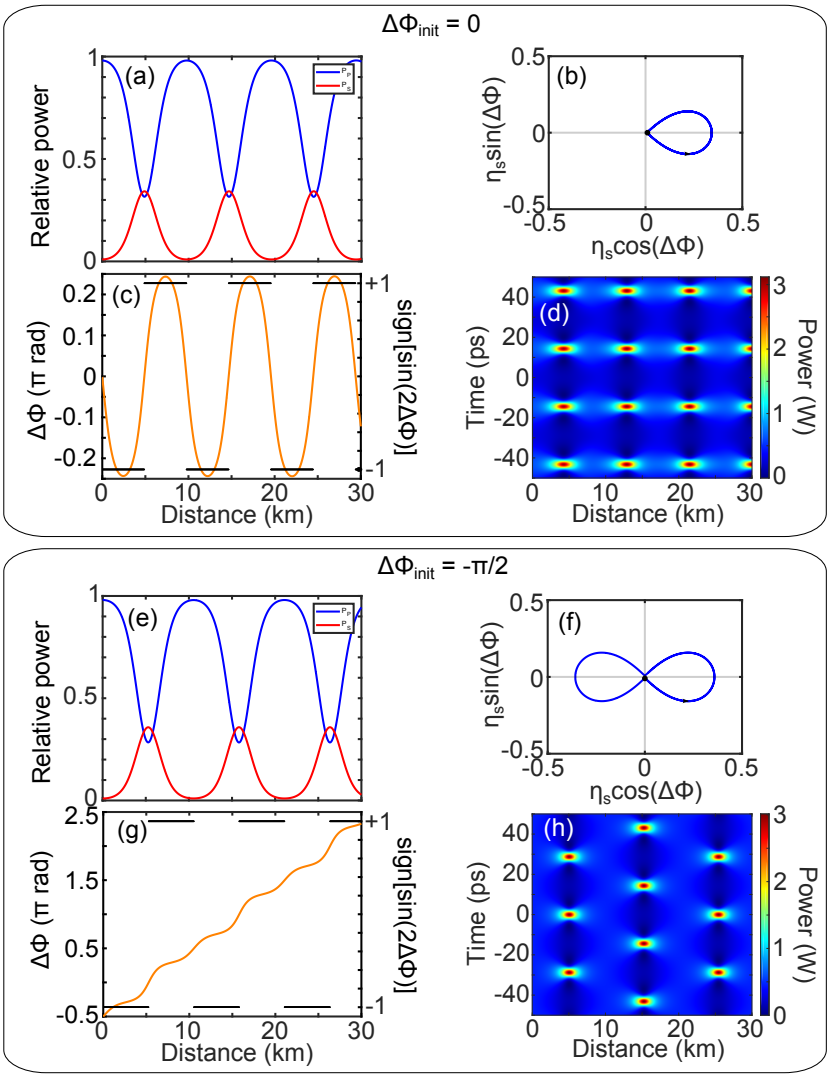

Figure 2.3: (a) Relative pump (blue) and signal (red) power evolutions for $\Delta\Phi_{init} = 0$, (c) the corresponding relative phase evolution and (b) the associated phase-plane evolution from the 3WM model. (d) Spatio-temporal evolution from the NLSE for the same three-wave input. (e-h) Same but for $\Delta\Phi_{init} = -\frac{\pi}{2}$.

wave progressively transforming into a pulse train before almost returning to its initial state. However, for $\Delta\Phi_{init} = -\pi/2$ [Fig. 2.3(h)] it presents a temporal shift of half a period between each recurrences, a feature which is not observed in the case where $\Delta\Phi_{init} = 0$ [Fig. 2.3(d)]. This illustrates what we will refer as the symmetry breaking of modulation instability, which can be simply explained by an Hamiltonian approach of the 3WM model.

Hamiltonian approach of the 3WM model

Considering a symmetric input and the conservation of the total energy, the system (2.8) can be reduced to a set of two equations involving the following Hamiltonian [42, 75, 76]:

$$H = \eta(1-\eta)cos(2\Delta\Phi) + (1-\omega^2/2)\eta - 3\eta^2/4 \tag{2.11}$$

where $\eta = 2\eta_s$ is the power fraction of the first-order sidebands and $\omega = 2\frac{\Omega}{\Omega_c}$ is a normalised frequency (i.e. $\omega_{max} = \sqrt{2}$ and $\omega_c = 2$). H corresponds to the Hamiltonian of a one-dimension oscillator and is similar to the one describing the motion of a rigid pendulum [79]. While the potential V associated with this system is a single well for $\omega > 2$, the transition to $\omega < 2$ induces this potential to undergo a symmetry-breaking to a double-well (see Ref. [76] for the expression of V, which is a quartic function of η). Evolution of the system can then be studied from two equivalent approaches. Fig. 2.4(a) displays the phase portrait of the system obtained by plotting the level curves of H in the plane $(\eta \times cos(\Delta\Phi), \eta \times sin(\Delta\Phi))$ and Fig. 2.4(b) shows a sketch of the double-well potential. We notice two types of trajectories separated by a separatrix or homoclinic loop (magenta line). The thick green line consists in inner trajectories (single-loop orbit) surrounding only one of the stable points C_0 or C_π, which corresponds to an evolution confined into only one of the well of the potential while the thick cyan curve consists in an outer trajectory (double-loop orbit) surrounding both stable points and corresponding to a double-well evolution. Note that these stables points correspond to invariant modulated wave (in the 3WM model) with opposite sideband phase $\Delta\Phi = 0$ and $\Delta\Phi = \pi$ relatively to the pump. Whereas maximum conversion is obtained for either $\Delta\Phi = 0$ or $\Delta\Phi = \pi$ in the case of inner trajectories, it is obtained by alternation between these two relative phases for outer trajectories, which correspond in the time domain to maximum compression points shifted by half a period [see Fig. 2.3]. Note that the critical phase of the separatrix is frequency-dependent and can be expressed as follows: $\Delta\Phi_C = cos^{-1}(\omega/2)$. An exhaustive discussion on the conditions of separatrix crossing will be done in Chapter 4, where we report the experimental observation of the symmetry-breaking of the nonlinear stage of MI.

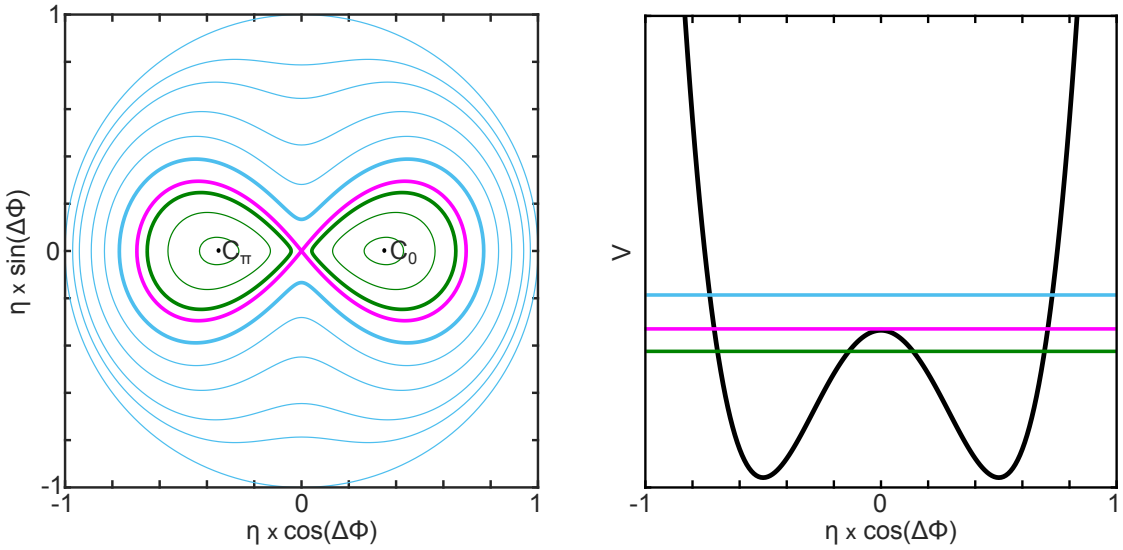

Figure 2.4: (a) Phase-plane evolutions in the plane $(\eta \times cos(\Delta\Phi), \eta \times sin(\Delta\Phi))$. (b) Sketch of the equivalent double-well potential associated with the 3WM process when $\omega < 2$.

Relevance of the 3WM model

We discuss here the relevance of the 3WM model which is suitable to get a simple qualitative description of the physics behind the nonlinear stage of MI but which still presents limitations, due to the fact that higher-order modes are neglected. The main discrepancy is related to the level of the local minima of the pump power as shown in Fig. 2.5(a) which displays the pump and signal relative power (compared to the total power) evolutions for $P_p = 450\,mW$, $\beta_2 = -19 \times 10^{-27} s^2/m$, $\gamma = 1.3 \times 10^{-3}/W/m$, initial signal/idler to pump ratio of -20 dB, $f = 35\,GHz$ and $\Delta\Phi_{init} = -\pi/2$ from the 3WM model (dashed lines) and from the NLSE (solid lines). We observe a 95% depletion of the pump with the NLSE against a 70% depletion with the 3WM model. The disagreement is due to energy transfer into higher-order modes as illustrated by Fig. 2.5(c) which shows the spectrum at the position for which the pump is minimal. As we can see from NLSE simulations (solid blue lines), while more than 70% of the total energy is encompassed in the pump and first-order sidebands, dozens of sidebands are involved in the process. Moreover, we also observe in Fig. 2.5(a) discrepancies concerning the position of these local minima (this particular subject will be discussed in Chapter 5 where we

investigate the position of the recurrences). However, we see that the 3WM model gives a good estimate of the local maxima of the signal power. The disagreement between the 3WM model and the NLSE increases for stronger input modulation, as illustrated by Figs. 2.5(b,d), which displays the level of the first local minimum of the pump power [Fig. 2.5(b)] and maximum of the signal power [Fig. 2.5(d)] versus the input signal to pump ratio (stars accounts for the 3WM model and diamonds for the NLSE). Indeed, the NLSE serving as a reference, the accuracy of the 3WM model is estimated by introducing the following relative error parameter:

$$error = \frac{|P_{extremum,NLSE} - P_{extremum,3WM}|}{P_{extremum,NLSE}} \tag{2.12}$$

where *extremum* refers to the minimum of the pump or the maximum of the signal. We observe a big increase of this error [crosses in Figs. 2.5(b,d)] when the input modulation power increases, from 500% for a signal to pump ratio of $-30\,dB$ to 5600% for a ratio of $-8\,dB$, which corresponds to a factor of more than 10. These high values are due in particular to the large depletion of the pump predicted by the NLSE. For example, for an signal/idler to pump ratio of $-10\,dB$, the pump power minima for the 3WM model is about $86\,mW$ (16% of the the total power), while it is about $5.4\,mW$ (1% of the total power) for the NLSE, leading to an error of $\sim 1500\%$. As explained previously, the error for the maximum of signal is far smaller, ranging from about 0% to 18%. All this calls for another theoretical approach which accounts for the higher-order modes.

2.3.2 Exact solutions of the nonlinear Schrödinger equation

In 1972, Zakharov and Shabat showed that the NLSE could be solved using the inverse scattering transform (IST) method [80–82], which is often described as a nonlinear equivalent of the Fourier Transform, and derived the well-known soliton solution which consists in a pulse with a secant hyperbolic shape which preserves its shape along the propagation, both in the time and frequency domains. Other classes of exact solutions can be derived using the IST such as the so-called first-order breathers or solitons on finite background (SFB) [83] which presents an interest in our case as some of them are intrinsically related to the growth and decay dynamics of the MI process [28].

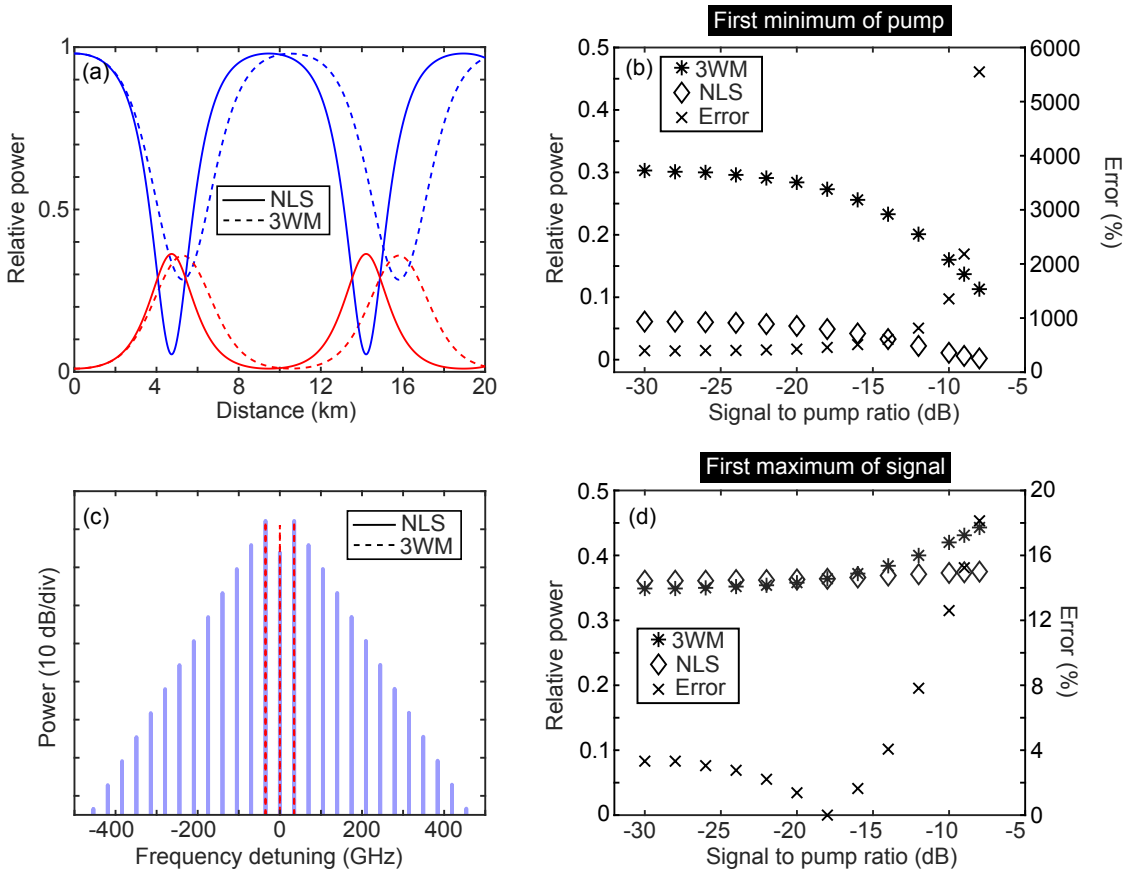

Figure 2.5: Comparisons between the 3WM model and NLSE simulations. (a) Relative pump (blue line) and signal (red line) power evolutions from the 3WM model (dashed lines) and NLSE simulations (solid lines) for $P_p = 450\,mW$, $\beta_2 = -19 \times 10^{-27} s^2/m$, $\gamma = 1.3 \times 10^{-3}/W/m$, initial signal/idler to pump ratio of -20 dB, $f = 35\,GHz$ and $\Delta\Phi_{init} = -\pi/2$. Pump and signal powers are normalised to the total power in the system. (b) First local minimum of pump power versus initial signal to pump ratio from the 3WM model (stars) and from the NLSE (diamonds) and associated error defined by Eq. (2.12) (crosses). (d) Same than (b) but for the first local maximum of signal power. (c) Optical spectrum when the pump power is minimal, from the 3WM model (dashed red lines) and from the NLSE (solid lines).

We introduce here the dimensionless NLSE which will be useful to discuss these solutions :

$$i\frac{\partial \Psi}{\partial \xi} + \frac{1}{2}\frac{\partial^2 \Psi}{\partial \tau^2} + |E|^2 E = 0 \tag{2.13}$$

where $\xi = z \times L_{NL}^{-1}$ [$L_{NL} = (\gamma P_p)^{-1}$ is called the nonlinear length] is the dimensionless distance, $\tau = T/T_0$ (with $T_0 = \sqrt{|\beta_2|\, L_{NL}}$) the dimensionless time and $\Psi = E/\sqrt{P_p}$ the dimensionless envelope. .

First-order breathers: focus on the Akhmediev breather

Solitons on finite background correspond to solitonic structures traveling on and interacting with a plane wave background. They are ruled by the following expression [84]:

$$\Psi(\xi,\tau) = exp(i\xi)\left[1 + \frac{2(1-2a)cosh(b\xi) + ibsinh(b\xi)}{\sqrt{2a}cos(\omega\tau) - cosh(b\xi)}\right] \tag{2.14}$$

where $a = \frac{1}{2}(1-\omega^2/4)$ and $b = \sqrt{8a(1-2a)}$. Because of these relations, there is only one governing parameter, let's say a, whose value determines the behaviour of the solution. Three qualitative types of evolution can then be distinguished by their periodicity and localisation properties depending on the value of this parameter a:

- for $0 < a < 0.5$ (which corresponds to $0 < |\omega| < 2$ the MI frequency range), b is the growth rate of MI and the solution is periodic in time and localised in space, experiencing growth and decay along ξ. This type of solution is known as Akhmediev breather (AB) and was first derived in the middle of the 1980's [84].

- for $a = 0.5$ the solution is localised both in time and space and is referred as the Peregrine soliton (PS) [39, 85].

- for $0.5 < a < \infty$ the solution is periodic in space and localised in time and is known as Kuznetsov-Ma breathers (KM) [40, 86, 87].

These solutions have attracted a great interest in the last decades as they play a key role in many complex nonlinear phenomena such as supercontinuum generation [30] or are identified as potential analytical formulation for rogue wave description [27–29, 88]. Here, we will focus on the AB, for which $0 < a < 0.5$, as it allows to describe analytically the MI process. The AB represents a separatrix orbit emanating and returning at infinite distance to the pump wave though experiencing a

phase shift [89] (its equivalent in the 3WM model corresponds to the thick magenta curve in Fig. 2.4). Experimentally, it is practical to study seeded MI by using a weakly-modulated continuous pump wave (i.e. a three-wave input) and Erkintalo *et al*. have shown [90] that the AB constitutes a good analytical framework to do so as it can asymptotically be approximated by a pump wave with a weak (ideally vanishing) cosine modulation (three-wave input with weak sidebands in the spectral domain). In particular Ref. [90] gives the initial relative phase of the first-order sidebands of the AB which can be expressed as $\Phi_{AB} = tan^{-1}(b/(2-4a))$. Note that simple trigonometric transformations allow to show that this formula is equivalent to the one of the critical phase in the 3WM model (section 2.3.1). We illustrate the performance of the AB framework by comparing in Fig. 2.6 to the AB the simulated evolution from the NLSE of a three-wave input with the following parameters: $P_p = 450\,mW$, $\beta_2 = -19 \times 10^{-27} s^2/m$, $\gamma = 1.3 \times 10^{-3}/W/m$, initial signal/idler to pump ratio of -20 dB, $\omega = 1.25$ (i.e. $f = 35\,GHz$) and $\Delta\Phi_{init} = -\Phi_{AB} \approx -0.284\pi$. As we can see, the AB is periodic in time and presents a single growth and decay cycle in space [Fig. 2.6(a)] with a maximum compression point around 4 km. Conversely, the simulation results in Fig. 2.6(c) shows the appearance of a second cycle with a second maximum compression point at about 19 km. Despite the use of a weak initial modulation, this is due to the deviation of the cosine input from the asymptotic AB. However, Figs. 2.6(b,d) show that the agreement is almost perfect for the first cycle. Indeed Fig. 2.6(b) displays the temporal profile at the maximum compression point for the cosine input (cyan solid lines). We observe very sharp and short structures with zero-point values on both sides, in almost perfect agreement with the AB (black dashed lines). Concerning Fig. 2.6(d), it shows the longitudinal evolution of the pump wave and the three first-order sidebands which present two back and forth conversion cycles. Again, the agreement with AB is almost perfect but it is limited to the first cycle. However, this agreement is obtained for relatively weak modulation (the initial modulation sidebands contain only about 2% of the total energy) and as the input modulation strength increases, discrepancies will appear. In Ref. [90] it is estimated that the agreement is relatively good up to initial signal to pump ratio of -20 dB.

The black dashed curves in Fig. 2.6(d) were obtained via the following analytical expressions of the AB spectral components [66]:

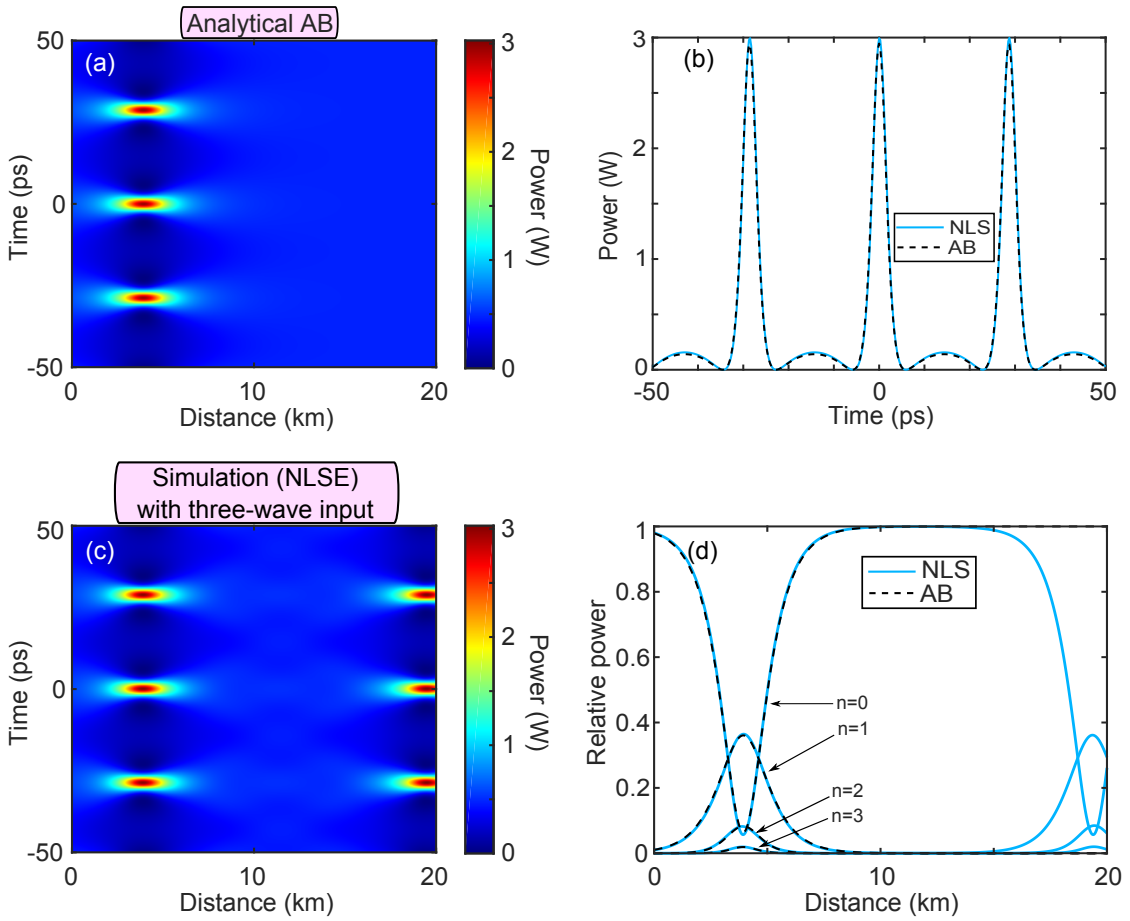

Figure 2.6: Spatio-temporal evolution of (a) the AB given by Eq. (2.14) and of (c) the three-wave input (cosine modulation) obtained by numerically integrating the NLSE. (b) Temporal profile at the maximum compression point ($z \backsimeq 4\,km$) for the initial cosine modulation (cyan solid lines) and for the AB (black dashed lines). (d) Longitudinal evolution of the pump and the three-first order sidebands for the initial cosine modulation (cyan solid lines) and the AB (black dashed lines). The index n refers to the sideband order. Note that Eq. (2.14) gives a maximum compression point at $z = 0\,m$. Hence, the AB solution in (c,d) have been longitudinally shifted so that the distance of the maximum compression points correspond.

$$\Psi_0(\xi) = -1 + \frac{ibsinh(b\xi) + 2(1-2a)cosh(b\xi)}{\sqrt{cosh^2(b\xi) - 2a}} \tag{2.15}$$

$$\Psi_n(\xi) = \frac{ibsinh(b\xi) + 2(1-2a)cosh(b\xi)}{\sqrt{cosh^2(b\xi) - 2a}} \left[\frac{cosh(b\xi) - \sqrt{cosh^2(b\xi) - 2a}}{\sqrt{2a}}\right]^{|n|} \tag{2.16}$$

where the subscript 0 corresponds to the pump and n to the $n^{th} - order$ sideband. Taking $\xi = 0$, one obtains a simple logarithmic relation between the amplitude of the sidebands which explains the triangular shape spectra which is universally observed at maximum compression points in MI experiments [19] as shown in the simulation displayed in Fig. 2.5(c).

As we have seen, the AB framework is suitable to describe the first cycle of MI recurrence. However, it suffers from several limitations. In fact, it does not allow to account for the initial relative phase between the pump and the sidebands, while it can have a strong impact on the dynamics as shown previously with the 3WM model and NLSE simulations. Moreover, recent experiments in bulk photorefractive crystal [64], water tanks [37] and optical fibres [42–44] reported the observation of two or more recurrence cycles. A broader and more insightful theoretical approach is then required. One could then use general doubly periodic solutions of the NLSE developed by Akhmediev *et al.* [24] which encompassed the previous breather solution. These complex solutions involve Jacobian elliptic functions and do not reduce to simple formulas such as equation (2.14). They are divided into two types, one corresponding to unshifted recurrences in the time domain and another corresponding to shifted recurrences. Both types of solutions are reported in Appendix A. In general, these solutions do not reduce to three waves, leading to discrepancies with experiments for which a three-wave input is mostly used. Comparison between numerical simulations and these analytical solutions is also discussed in Appendix A. Recently, a significant step forward has been made by Grinevich and Santini [45] which improved the matching theory with the AB. They derived simple formulas depending on the three-wave input parameters to predict the position of the first maximum compression point and the spatial recurrence period, which will be studied in details in Chapter 5. Note that another theoretical approach using the finite-gap theory of the NLSE was investigated by the same authors [91] but it reveals to be

very challenging and not convenient to use.

Higher-order breathers

Other classes of solutions of the NLSE consist in higher-order breathers which correspond to the nonlinear combination of first-order solutions described previously. These higher-order solutions are of great interest to describe the nonlinear stage of MI when the perturbation is more complex than a single set of sidebands, allowing in particular a more thorough description of the origin of rogues waves [41, 92–96] but they are often quite involved. Breather collisions and the second-order breather formalism will be discussed in Chapter 6.

2.4 Impact of other parameters

We have considered until now FPUT recurrences in the context of the "pure" nonlinear Schrödinger equation, thus accounting only for GVD and Kerr effects. Because we work at $1.55\,\mu m$ which is far from the ZDW of the SMF-28 used in experiments, higher-order terms do no affect the propagation. This has been checked numerically by including a third and fourth-order dispersion terms: $\beta_3 = 1.2 \times 10^{-40} s^3/m$ and $\beta_4 = -1 \times 10^{-55} s^4/m$ (note that, in the case of low-dispersion regime, it has been shown that the third-order dispersion can cause the disappearance of FPUT recurrences due to irreversible losses related to Cherenkov radiations [38]). The linear losses, however, have a strong influence as illustrated in Fig. 2.7, which displays the pump and signal power evolutions for an initial signal to pump ratio of -10 dB and for $\Delta\Phi_{init} = 0$ (a) or $\Delta\Phi_{init} = -\pi/2$ (b). In both cases, one can see that the losses strongly influence the recurrences, by reducing the amplitude of both pump and signal waves. Moreover, while we still distinguish two "pseudo-recurrences" in the case of $\Delta\Phi_{init} = -\pi/2$, we observe only one in the case of $\Delta\Phi_{init} = 0$. Thus, the impact of the attenuation on the recurrent process is more or less pronounced depending on the initial relative phase, which is intrinsically linked to the complex nonlinear dynamics of the system (see Eqs. 2.8). Note that losses also impact the relative phase evolution, leading eventually to separatrix crossing [37]. This will be discussed in Chapter 4.

Linear attenuation is not the only process which can lead to the disappearance

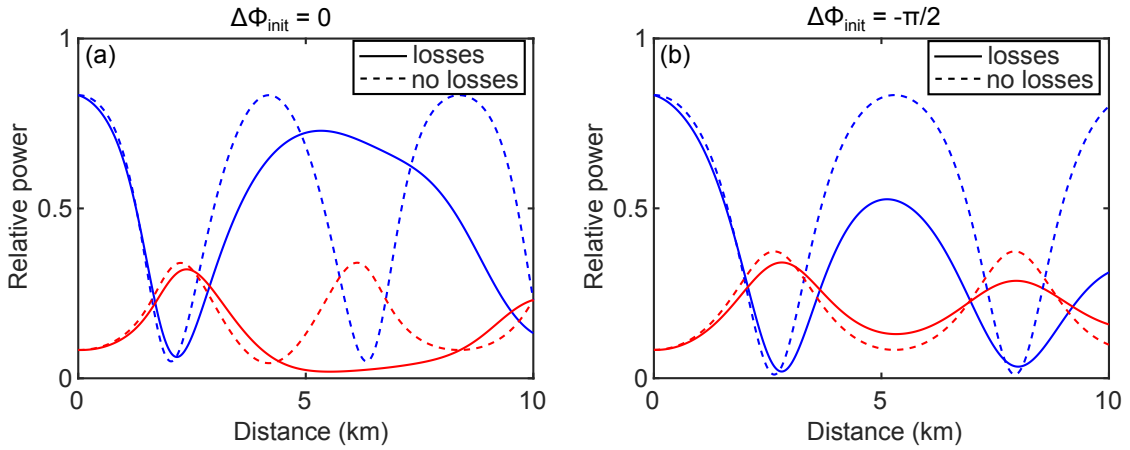

Figure 2.7: Influence of the linear attenuation on the recurrent process. (a) Pump (blue lines) and signal (red lines) power evolutions for $\Delta\Phi_{init} = 0$. Solid lines correspond to the case with losses ($\alpha = 0.2\,dB/km$) and dashed ones to the case without losses. (b) Same for $\Delta\Phi_{init} = -\pi/2$. Other parameters : $P_p = 450\,mW$, $\beta_2 = -19 \times 10^{-27} s^2/m$, $\gamma = 1.3 \times 10^{-3}/W/m$, initial signal/idler to pump ratio of -10 dB, $f = 35\,GHz$.

of the recurrences. Indeed, up to this point, we have considered noiseless three-wave input which is not realistic in experiments, as there is always at least a quantum level noise. The amplification of this noise due to MI will irreversibly lead to a continuum, killing then the recurrences [97]. This noise-induced thermalisation of the recurrences is illustrated in Fig. 2.8 for which we introduced a noise floor about 75 dB below the pump (note that this is higher than the quantum level noise). We clearly notice the amplification of the noise in Figs. 2.8(c,d,e) and the killing of the recurrence process after two recurrences in Fig. 2.8(b).

Note that many other physical effects can cause the break-up of FPUT recurrences but they were not an issue in our case. For instance, it has been shown that non-instantaneous Kerr nonlinearity exhibited by some media can inhibit the recurrent process [98].

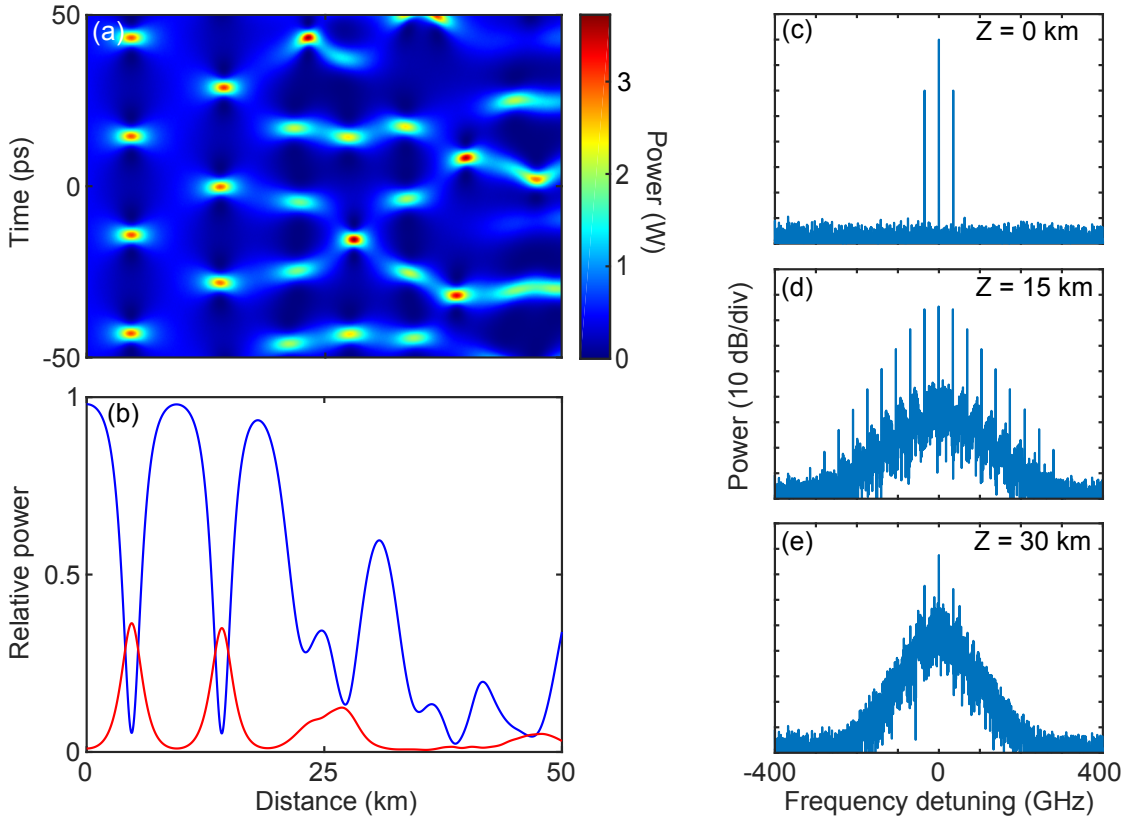

Figure 2.8: Influence of the initial noise. (a) Spatio-temporal evolution of the field power and (b) evolution of the pump (blue) and signal (red) powers. (c,d,e) show the spectrum at three different distances of propagation. Same parameters than in Fig. 2.7, except for the additional noise and an initial signal/idler to pump ratio of -20 dB.

Summary

- We summarised briefly the origin of the FPUT recurrence problem and highlighted its universal character.
- We provided then the theoretical framework to describe the linear and nonlinear stage of seeded MI, FPUT recurrences being associated to the latter in nonlinear optics. Several models were reported with an emphasis on the truncated 3WM model which is suitable to describe the physics behind the process investigated. Other models based on a class of exact solutions of the NLSE were reported with a focus on the Akhmediev breather.
- We highlighted the importance of parameters which are not included in the pure NLSE, in particular the linear attenuation, as well as the impact of noise on the recurrence process.

Chapter 3

Distributed measurements of modulation instability

Contents

We focus in this chapter on the implementation of an experimental setup allowing the non-invasive distributed characterisation in phase and in intensity of the main discrete frequency components of a pulse (i.e the pump and signal/idler waves) in order to observe at least two FPUT recurrences. In the first section we discuss the state of the art about distributed measurements of modulation instability in optical fibres. We then explain in details the novel experimental technique that we developed, which consists in a heterodyne time-domain reflectometer (HOTDR) associated to an active loss compensation scheme based on Raman amplification [42].

3.1 State of the art on distributed measurements.

In optical fibre experiments, it is obvious to say that one can often access easily to the input and the output of the fibre under test but it is much more complicated to get insights on the dynamics inside the fiber. In this section we will list and detail the pros and cons of several techniques which have already been used to perform distributed characterisation of processes related to modulation instability and which could be suitable for our measurements. We will talk about cut-back measurements, scaling laws and scattering processes-related techniques.

Cut-back

In order to perform distributed measurements the easiest technique is to change the length of fibre. To do that, one can either use fibres of different lengths or cut-backs, which consists in cutting a piece of fibre to reduce its length, and then splice a connector or use a rapid connector at its output in order to perform a measurement. This technique was for example used by Hammani *et al.* [66] to perform distributed characterisation of ABs (which are related to FPUT as explained in the previous chapter) in the frequency domain or by Mussot *etal.* [38] to characterise the impact of the third-order dispersion on the FPUT process. Despite the ease of implementation, this technique suffers from several drawbacks. First, it is of course an invasive technique, the fibre used being destroyed, which can be costly and which prevents to redo the experiment in the same conditions. Furthermore, to get a good resolution (which is required in our case to observe for example sharp phase jumps) the fibre might have to be cut by very short steps, which is time consuming. This can be very detrimental, as it increases the possibility that the input conditions change during the process and we have seen in the previous chapter that a small change of $\Delta\Phi_{init}$ can have a big impact on the dynamic. Nonetheless, it is worth mentioning that Xu *et al.* [99] recently reported the distributed characterisation in intensity and phase of Peregrine-like structures using a similar method (fibres of different lengths instead of cut-backs).

Scaling law

As we have seen in Chapter 2 with the normalised form of the NLSE, the dimensionless distance reads $\xi = \gamma P_p z$. One can then use a fibre of fixed length and perform indirect distributed measurements by varying P_p instead of the distance z. This method was used for the first observation of Peregine soliton [39] and in particular for the first observation of FPUT recurrence in optics by Van Simaeys *et al.* [31,65]. However, varying P_p also changes the MI frequency which scales in $\sqrt{P_p}$ so the frequency detuning of the seed has also to be varied to keep a normalised frequency detuning constant, which is not really convenient.

Scattering processes

Another approach to perform distributed measurements is the use of scattering processes, either elastic (Rayleigh) or inelastic (Raman and Brillouin), which present the advantage of being non-invasive and offer a good resolution [100]. Although they are mainly used to perform measurements of external parameters such as temperature or distributed strain, these techniques revealed to be also useful for the characterisation of nonlinear optical processes. As examples, Brillouin optical time-domain reflectometry have been used [101, 102] to characterise fibre optical parametric amplifiers. Concerning OTDR based on Rayleigh scattering, it enabled for example the distributed measurement of Raman gain spectrum [103], modulation instability [104] or supercontinuum in highly-nonlinear fibres [105] and in particular the observation of one FPUT recurrence via the distributed characterisation of the pump and low-orders sidebands intensity, reported by Hu *et al.* [67].

Summary

While phase measurements could have been implemented in most of these techniques, it has never been done in the context of FPUT recurrences. Moreover, in these studies, the number of recurrences observed were limited to a single recurrence, due to the intrinsic losses of the fibre. Table 3.1 recaps the performances of the main techniques mentioned and introduces the technique that we will implement and describe thereafter which consists in a heterodyne optical time-domain reflectometer (based on Rayleigh scattering) associated with a loss compensation scheme based on Raman amplification.

Paper/Technique	Intensity	Phase	Loss compensation	Non-invasive	Number of recurrences
Van Simaeys *et al.* Phys. Rev. Lett. 87 (2001) / Scaling law	✓	✗	✗	✓	1
Hammani *et al.* Opt. Lett. 36 (2011) / Cut-back	✓	✗	✗	✗	1
Mussot *et al.* Phys. Rev. X 4 (2014) / Cut-back	✓	✗	✗	✗	1.5
Hu *et al.* IEE Phot. Tech. Lett. 30 (2018) / OTDR	✓	✗	✗	✓	1
Mussot *et al.* Nat. Phot. 12 (2018) / HOTDR + Raman amplification	✓	✓	✓	✓	≥2

Table 3.1: Performances of the main experimental techniques used for the characterisation of FPUT recurrences.

3.2 The experimental setup

As mentioned before, the setup that we implemented is based on a heterodyne optical time-domain reflectometer. Here, we recall rapidly the principle of heterodyne detection, which is a common technique used in particular to perform coherent detection in optical fibre systems [106]. Indeed, this is the heterodyne nature of the setup which allows us to perform phase measurements.

Let's consider the following monochromatic signal of amplitude A_1, frequency Ω_1 and phase Φ_1:

$$E_1(t) = A_1 cos[\Omega_1 t + \Phi_1] \tag{3.1}$$

For a signal at 1550 nm, $\Omega_1 \backsimeq 193\,THz$ which far exceeds the bandwidth of photodetectors (a few dozens of GHz maximum). Thus, a photodetector would average the signal and give an output signal with the following intensity:

$$I \propto \frac{1}{2} A_1^2 \tag{3.2}$$

In this case I is not time-dependent and the information on the phase is then lost. This issue can be fixed by mixing previously to the photodetector the signal we want to measure with a reference signal called "local oscillator":

$$E_{OL}(t) = A_{OL}cos[\Omega_{OL}t + \Phi_{OL}] \tag{3.3}$$

The intensity I at the output of the photo-detector is then:

$$I(t) \propto |E_1(t) + E_{OL}(t)|^2 \tag{3.4}$$

Developing Eq. (3.4) gives terms in Ω_1, Ω_{OL}, $\Omega_1 + \Omega_{OL}$ and $\Omega_1 - \Omega_{OL}$. If Ω_{OL} is chosen close enough to Ω_1, only the term $\Omega_1 - \Omega_{OL}$ can lie within the bandwidth of the photodetector and the other terms are averaged so:

$$I(t) \propto \frac{1}{2}A_1^2 + \frac{1}{2}A_{OL}^2 + \frac{1}{2}A_1A_{OL} + A_1A_{OL}cos[(\Omega_1 - \Omega_{OL})t + \Phi_1 - \Phi_{OL}] \tag{3.5}$$

Using a simple high-pass filter, one can filter out the DC (direct current) terms, to only keep the time-dependent term. One can then retrieve the variation of A_1 and Φ_1 if A_{OL} is fixed, as well as Φ_{OL} (this requires initial phase-locking). In this section, we will then describe how we implemented this method to measure the intensity and phase of Rayleigh backscattered signals. First we give a complete schematic of the experimental setup. Secondly, we detail how we generate the suitable three-wave input to trigger the MI and FPUT processes. Then we discuss about the phase-locking of the local oscillator before describing the procedure implemented to suppress a detrimental effect called fading phenomenon, which is linked to Rayleigh backscattering. Next, we introduce the Raman amplification scheme used in order to compensate for the intrinsic losses along the propagation. Finally, we discuss the performance, stability and limitations of the setup.

3.2.1 Implementation

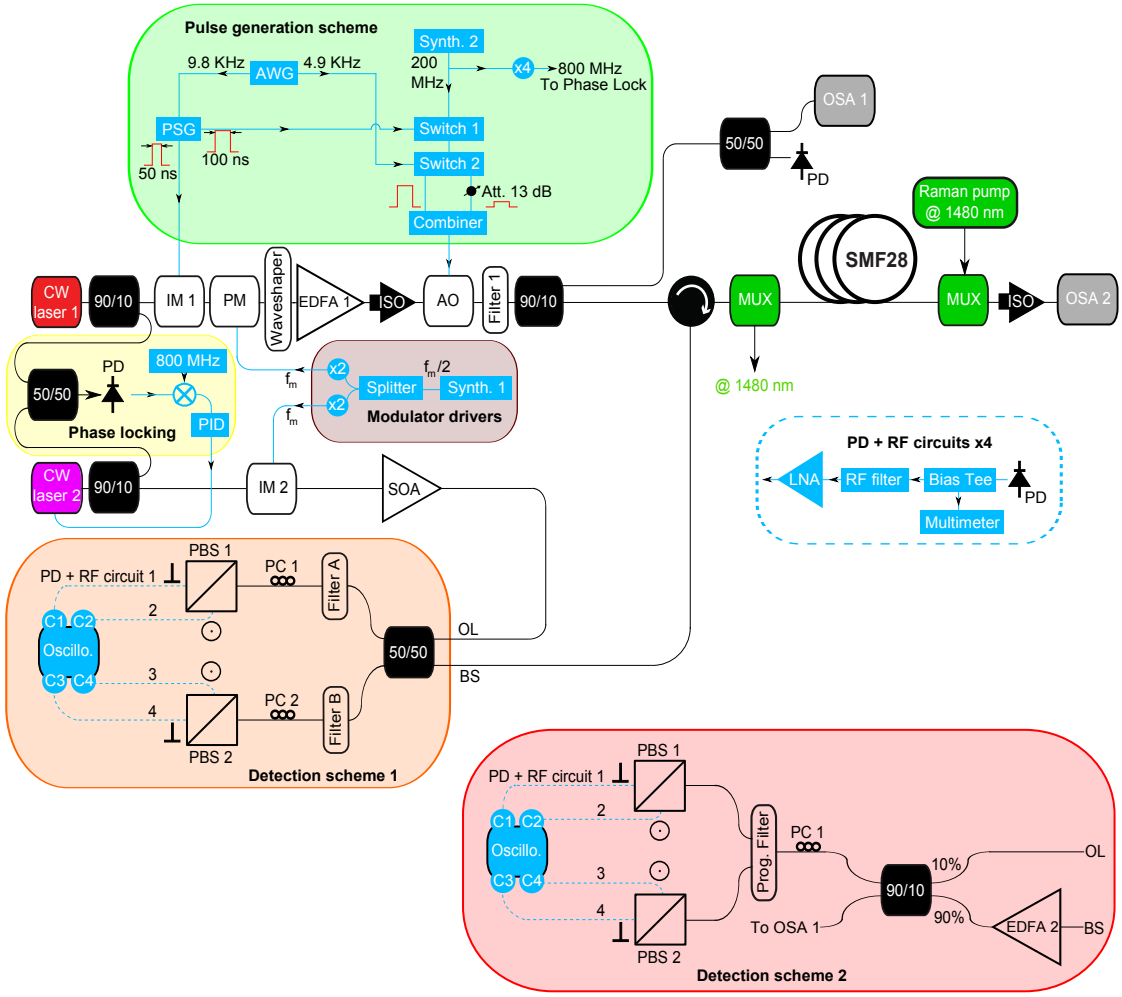

Figure 3.1: Experimental setup. Laser 1 is a narrow linewidth (100 Hz at FWHM) CW laser and laser 2 is a continuous distributed feedback laser diode. IM(1,2): intensity modulator, PM: phase modulator, PSG: pulse signal generator, AWG: arbitrary waveform generator, EDFA(1,2): erbium-doped fibre amplifier, ISO: isolator, AO: acousto-optic modulator, MUX: multiplexer or de-multiplexer, SOA : semiconductor optical amplifier, PID: proportional, integral, derivative controller, PD: photo-detector, PC: polarisation controller, PBS: polarisation beam splitter, RF: radio frequency, LNA: low-noise radio frequency amplifier. All the instruments of the setup (including the oscilloscope) are referenced to the same 10 MHz clock.

3.2.2 Input generation

The first step to design and generate a suitable three-wave input consists in the intensity modulation of the CW beam delivered by laser 1 in order to generate 50 ns square-shaped pulses [Fig.3.2(a)] at a 9.8 KHz (∼102 µs) repetition rate. To do so, an arbitrary waveform generator generates a clock at 9.8 KHz to trigger a pulse generator that delivers the RF signal driving the intensity modulator (IM1). Then, the optical pulses pass through a phase modulator (PM) to generate a frequency comb with a 35 GHz line spacing. A programmable optical filter (Waveshaper) with a filter bandwidth of 10 GHz allows then to tailor the frequency comb to keep only the pump, signal and idler waves and to control their relative phases. Figure 3.2(b) shows the spectrum at the output of the Waveshaper when we do not apply any filters (blue line) and when a filter is applied to get a symmetric three waves input. As can be seen, the unwanted harmonics are effectively filtered. Following the Waveshaper, the pulses are amplified via an erbium-doped amplifier (EDFA 1) to reach the desired peak power (usually around 450 mW) and goes through an acousto-optic modulator with a high extinction ratio (typically superior to 50 dB) to reduce the CW background between the pulses in order to mitigate stimulated Brillouin scattering (SBS). Finally, a filter with a 1 nm bandwidth (Filter 1) removes

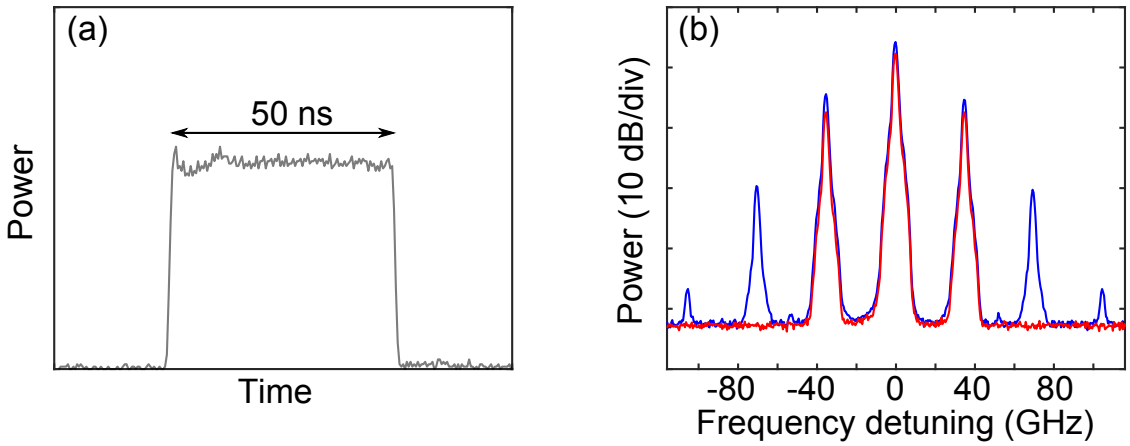

Figure 3.2: (a) Temporal profile of the pulse. (b) Spectral profile of the pulses at the output of the Waveshaper without any correction filter applied (blue) and with a filter applied (red).

the amplified spontaneous emission in excess. For the 4 GHz OSA resolution (this resolution is the same for all the optical spectra reported in this thesis) it allows to

get a signal to noise ratio of about 50 dB for the pump and 40 dB for the signal and idler [see Fig. 3.2(b)]. Note that because the pulses have a flat top whose duration is far greater than the MI period (50 ns to be compared to about 30 ps) we can consider that we operate in the CW regime of MI.

3.2.3 Local oscillator and phase-locking

In order to perform phase measurements via heterodyning, the local oscillator (laser 2) has to be initially phase-locked with laser 1. To do so, we used the method described in Ref. [107] based on laser difference-frequency. A 5 GHz bandwidth photodiode receives the beat note of laser 1 and 2 which is then mixed with a 800 MHz RF reference signal provided by a stable synthesizer. In order to have a beat note close to 800 MHz, the frequency of laser 2 can be coarsely tuned via its power supply. The resulting intermediate frequency goes then through a PID controller (with a response time less than 15 ns) which drives the phase of the local oscillator. Efficiency of the phase-locking can be monitored by looking at the beat signal of laser 1 and 2 on a signal analyser as shown in Figs. 3.3(a,b), which display the RF spectrum (with a 100 Hz resolution) of the beat signal when the locking is turned off and on, respectively. Once the lasers are phase-locked, the locking can last up to several hours.

As we intend to perform measurements not only on the pump component but also on the signal/idler one, laser 2 is modulated in intensity by IM2 to create sidebands spaced by 35 GHz so that each frequency component of interest have its own local oscillator. The RF signal driving IM2 is delivered by the same microwave source driving the previous phase modulator in order to ensure a fixed phase relation between them. The local oscillator is then amplified by a semiconductor optical amplifier (SOA) and the amplitude of its three main sidebands are roughly equalised by tuning the DC bias voltage of IM2 to get similar local oscillators, as can be seen in Fig. 3.3(c), which shows the spectrum of the local oscillator after the SOA.

3.2.4 Fading suppression technique and signal processing

In optical time-domain reflectometry, it is known that a random noise in amplitude and phase is superimposed on the backscattered signal [108]. This noise, which is

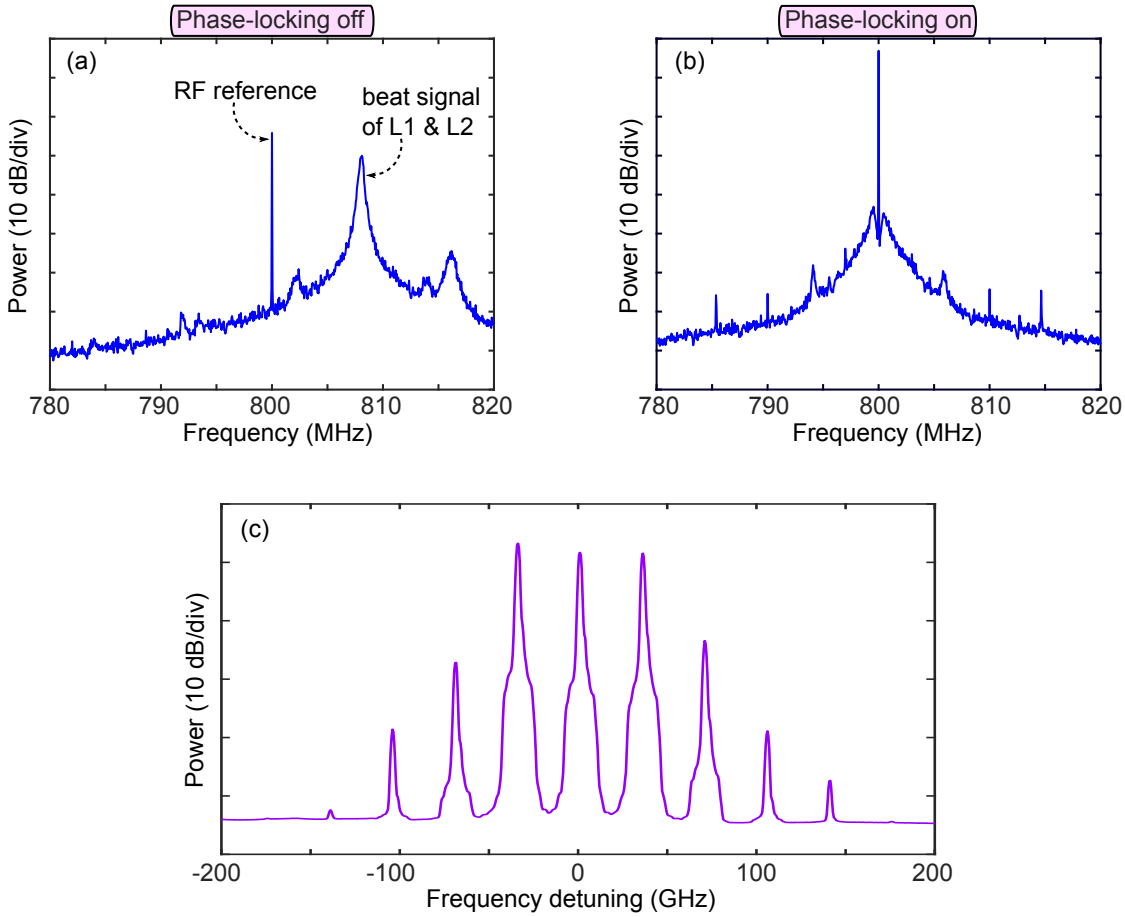

Figure 3.3: RF spectra of the mixing of the beat signal of L1 and L2 with the 800 MHz reference when the system is (a) not phase-locked and (b) phase-locked. (c) Optical spectrum of the local oscillator.

detrimental as it leads to jagged measurements, finds its origins in the random state of polarisation of the backscattered light and a speckle-like phenomenon due to huge number of scattered waves involved in the process and/or in the thermo-mechanical fluctuations of the propagating medium. In order to avoid it, many techniques have been developed such as averaging over a huge number of backscattered signal and polarisation scrambling [109,110]. However, none of theses techniques have been proven to be effective and compatible with accurate distributed phase measurements in our case. Thus, we have developed a novel method which allows to remove effectively this additional source of noise. In fact, we make the assumption that the fading phenomenon is a purely linear effect and that the thermo-mechanical

fluctuations have a characteristic time of a few milliseconds.

Therefore, we propose the following post-processing treatment to suppress the fading. We first launch a strong 50 ns pulse (450 mW peak power) into the fibre which will experience both linear and nonlinear dynamics. Then, 102 µs later, a weak pulse, attenuated by 13 dB, follows and we assume that it experiences only linear effects. The attenuation is obtained via the acousto-optic modulator which is driven at half-rate clock (4.9 KHz) so that one pulse over two is attenuated as it is displayed in the schematic in Fig. 3.4(a). Note that the 102 µs delay between two consecutive pulses is long enough to avoid any overlapping between two backscattered signals but very short compared to the response time of the thermo-mechanical fluctuations which ensures that the linear fading effects experienced by both backscattered waves (from the strong and weak pulses) are strongly correlated. To illustrate the difference of dynamic experienced by the two types of pulses we create sequences of strong or weak pulses only and look at their spectra at the input and output of the fibre as displayed in Figs. 3.4(b,c). We observe that the strong pulses (magenta lines) at the output of the fibre are not anymore composed of only three waves (the two very weak harmonics in the input, 30 dB below the signal and idler waves, results from residual four-wave mixing between the Waveshaper and the input of the fibre and are considered as negligible) but of 11 waves in the 400 GHz spectral window analysed in this typical example. These multiple harmonics are due to modulation instability and four-waves mixing, which are nonlinear effects. At the opposite, we do not observe this for the weak pulses (cyan lines). One can notice really small harmonics of the signal/idler waves but more than 25 dB lower so they can be considered as negligible. Moreover, the signal/idler to pump power ratio is conserved between the input and output which is a signature that the weak pulses do not seem to experience nonlinear effects whatsoever. In fact, for the weak pulses $P_p \approx 20\,mW$ which implies a cutting frequency of the MI gain range of $\Omega_c \approx 12\,GHz$. Thus, the signal and idler at $\pm 35\,GHz$ fall out of the range of MI gain and, moreover, the FWM efficiency is weak due to the large dispersion. Note that we analyse each states of polarisation of every backscattered signal independently (which are later recombined in post-processing) thanks to the use of polarisation beam splitters, thus avoiding the need of polarisation scrambling.

Once the heterodyned signals are logged with the four channels of the oscilloscope (two channels for each polarisation of the pump and two for those of the signal

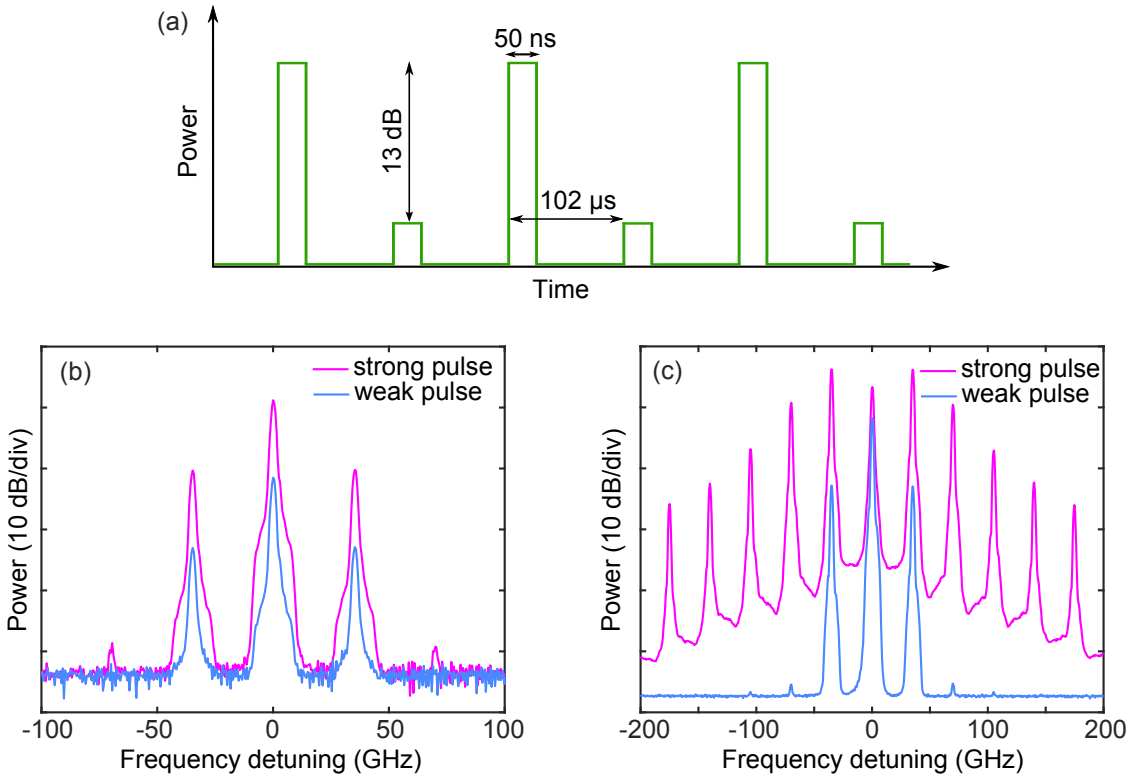

Figure 3.4: (a) Schematic of the sequence of pulses launch into the fibre. (b) Spectrum of the strong (magenta lines) and weak (cyan lines) pulses at the input of the fibre and (c) at the output of the fibre.

sideband) the measurement construction operates as follows. We will refer to each traces observed on the oscilloscope as $E_{Pow,Pol,Channel}(z)$ with z being the distance along the fibre (obtained simply by converting the time of flight of the backscattered wave into a distance), Pow can either be $Strong$ (for the nonlinear pulse) or $Weak$ (for the reference), Pol is either 1 or 2 for each polarisation state and $Channel$ refers to $Pump$ or $Signal$. The ratios $\frac{E_{Strong,1,Pump}(z)}{E_{Weak,1,Pump}(z)}$ and $\frac{E_{Strong,2,Pump}(z)}{E_{Weak,2,Pump}(z)}$ are calculated (the procedure is similar for the signal sideband) in order to remove all linear contributions and to cancel the fading effect in amplitude and phase[1]. Then, we perform demodulation with a short time fast Fourier transform (FFT). The

[1]Unfortunately, this removed also the linear phase due to the group velocity dispersion acquired during the propagation, which cannot be neglected as it directly impacts the dynamics of the system. The following phase term $\frac{1}{2}\beta_2(2\pi f)^2 z$ is then added later on to the measured pump-signal phase difference to get $\Delta\Phi$.

vectors composed by the previous ratios are sliced into segments made of 512 or 1024 samples. Each segments has a 50% overlap with the previous one to optimise the resolution. After application of a Hamming window, the power and the phase at 600 MHz are evaluated with a FFT. The demodulation is performed at this frequency and not 800 MHz because one has to take into account the 200 MHz shift induced on laser 1 by the acousto-optic modulator. The pulse width being 50 ns, the ultimate resolution achievable by our system is about 5 meters. However, due to the 512/1024 points segments length and considering the 2500 MHz sampling rate of the oscilloscope, the resolution is around 10 m/20 m. This is to be compared with the 7.7 km fibre length and to the 2-3 km recurrence period. All the demodulated traces are then averaged over at least one hundred shots to remove the noise and filtered afterward, by two-types of filters : a median filter and a Savitzky-Golay filter. Performance of our measurement technique is illustrated in Fig. 3.5. Fig. 3.5(a) and (e) show a single-shot of the pump and signal power evolutions (normalised to their respective maxima) and their relative phase without calibration with the reference (weak pulse). One can distinguish the exchange of energy between the pump and the signal but the measurement is very noisy and the relative phase evolution does not agree at all with the one expected. Fig. 3.5(b) and (f) show the same measurements but this time with the calibration (fading removed). Although the measurements are still very noisy, one can notice almost two recurrences by looking at the power evolutions and a specific relative phase evolution with jumps around 2 km and 6 km which are approximately the positions where the direction of the power flow between the pump and the sideband reverses. After averaging over one hundred shots, we observe an important reduction of the noise as displayed in Fig. 3.5(c) and (g). We obtain then cleans traces after filtering as shown in Figs. 3.5(d) and (h). Moreover we display in Figs. 3.5(i,j) the phase portraits of the signal filtered and averaged over one hundred shots without (i) and with (j) the calibration. While we observe a trajectory going on both sides of the phase-plane in Fig. 3.5(i), its shape is not at all an “eight” shape as expected and as observed in Fig. 3.5(j). This shows that averaging and filtering are not enough and illustrates the importance of the calibration.

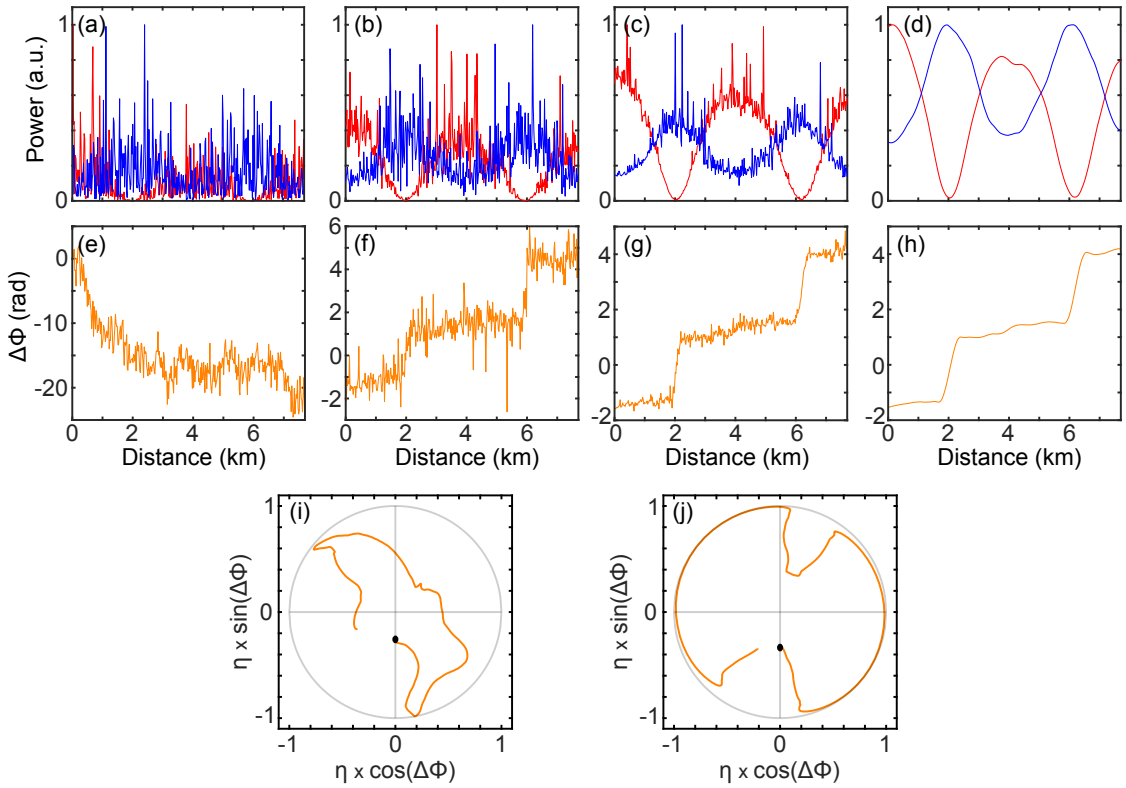

Figure 3.5: (a) Single-shot of the pump (red line) and signal (blue line) power evolutions along the fibre when the calibration is off and (b) when the calibration is on. (c) Averaging over a hundred shots of the pump and signal power evolution when the calibration is on and (d) same after filtering. (e,f,g,h) show the relative phase evolutions corresponding to (a,b,c,d) respectively. (i) Filtered and averaged phase portrait of the signal with the calibration off. (j) Same with the calibration on. All powers plot are normalised to their respective maxima.

3.2.5 Loss compensation scheme : Raman amplifier

As explained in Chapter 2, the intrinsic linear losses of a fibre, even small, are detrimental as it kills the FPUT recurrences and affects the dynamics. The experimental impact of the losses is illustrated in Figs. 3.6(a,c,e,g) which show the signal power evolution without any compensation of the strong (a,c) and weak (e,g) pulse for two different initial relative phase, $\Delta\Phi_{init} = -\pi/2$ and $\Delta\Phi_{init} = 0$. We observe a general decreasing of the weak pulse of 3 to 5 dB which is to be compared to the 2.88 dB ($2 \times 7.7\,km \times 0.2\,dB/km$) minimum intrinsic losses expected. This decreasing has a direct impact on the measurements in Fig. 3.6(a) and (e) as we perform a ratio

to get them (calibration procedure to remove the fading). This explains why the second maximum (around z = 6 km) appears bigger than the first one (around z = 2 km) in Fig. 3.6(a). Moreover we see that we are not able to observe a second recurrence for the case where $\Delta\Phi_{init} = 0$, which confirms the previously stated fact in Chapter 2 that the power evolutions in this case are more sensitive to losses than for $\Delta\Phi_{init} = -\pi/2$.

Hence, we introduced a Raman amplification scheme in our system in order to compensate for the linear attenuation of the SMF-28 fibre used in experiment. This idea, borrowed from the telecommunication field where distributed Raman amplification is commonly used [57], has been recently implemented successfully in a handful of nonlinear fiber optics experiments [42, 43, 111, 112]. In our case, the Raman laser source is located at 1480 nm and contra-propagates in order to minimize the relative intensity noise transfer compared to the co-propagative case. The ideal location of the Raman laser would be 1450 nm (i.e. -13.2 THz detuning) in order to benefit from the maximum gain and "flatness" of the Raman response as explained in Chapter 1. However, even at the maximum compression point, the spectrum is not larger than about 1 THz so we can assume that every spectral components experiences almost the same gain. This is verified by the fact that we do not observe any asymmetry (relatively to the pump) on the spectrum at the output of the fibre as displayed in Fig. 3.4(c) (magenta line) where the Raman pump was on. A realistic simulation of this distributed Raman amplifier is very complex as one has to take into account the depletion of the Raman pump, the contra-propagation architecture and the polychromatic nature of the pulse we want to amplify. Thus, the Raman pump power was set empirically as follows. We choose the configuration where $\Delta\Phi_{init} = \pm\pi/2$ and increase the Raman pump power until the level of signal sideband power at the second peak of conversion is similar to the first one [Fig. 3.6(b)]. Note that the decreasing trend of the weak pulse is then not observable anymore [Fig. 3.6(f,h)]. With this compensation, the second peak of conversion for the case with $\Delta\Phi_{init} = 0$ clearly appears and its amplitude is slightly below the amplitude of the first peak [(Fig. 3.6(d)]. This is not detrimental as we will point out in Chapter 4 that the recurrences with a three-wave input are not perfect, especially for $\Delta\Phi_{init} \neq \pm\frac{\pi}{2}$.

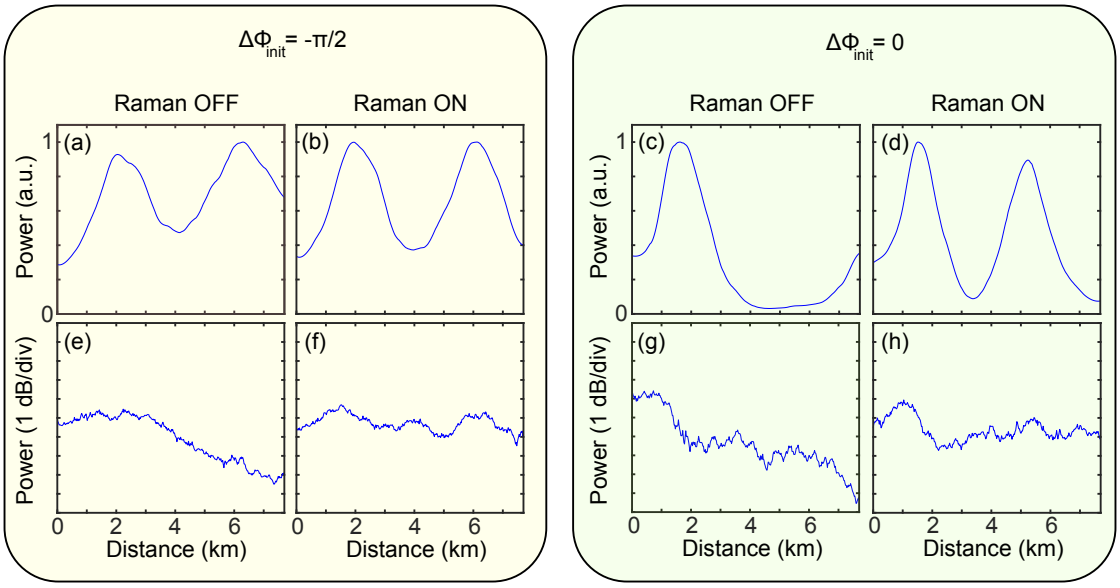

Figure 3.6: Losses compensation via Raman amplification. Power evolution of the signal component of the strong (a) and weak (e) pulse when the Raman amplification scheme is off and for $\Delta\Phi_{init} = -\pi/2$. (b,f) Same with the Raman amplification turned on. The second panel shows similar figures but for $\Delta\Phi_{init} = 0$.

3.2.6 Stability of the setup and noise limitations

The stability of the experimental setup is a key point to perform reproducible and reliable measurements. As many parameters are involved, it is not easy to quantify this stability. However, some systematic procedures or methods have been implemented to ensure that key parameters such as the pump power do not vary much. First, most of the setup is computer driven. That allows us to perform a recording sequence (which corresponds to the averaging of at least one hundred single-shot recordings) in less than two minutes, a duration that also includes the post-processing time in order to display the power and relative phase evolutions and the associated phase-plane structure. To be sure that the input pump and sidebands powers stay the same during a sequence we use the following method. At the beginning of each new acquisition, the sidebands generation (via the phase-modulator) is first shut-off and a MI spectrum is recorded at the output of the fibre and compared to a reference. This spectrum is indeed highly dependent on the pump power as explained in section 2.2 (the cutoff frequency varies in $\sqrt{P_p}$ and the maximum gain varies exponentially with P_p). If needed, the power can be adjusted by tuning

the current of EDFA1 or thanks to the Waveshaper (it has a 0.01 dB attenuation resolution). Then, the sideband generation is switched-on and another spectrum is recorded. The hundreds of recording are then performed before that, at the end of the sequence, two other output spectra are recorded (sidebands on and off). This allows us to check that no measurable drift occurred during the sequence by comparing the spectra obtained at the end and at the beginning of it. We estimate that it allows a stabilisation of the input powers with a reproducibility of about 0.1 dB. Concerning the input relative phase, it is considered as stable with a resolution of less than 0.1 rad.

The backscattered signal being very weak (-82 dB for a 1 ns pulse according to the datasheet from Corning [51] which gives a backscattered power of about $140\,nW$ for a 50 ns pulse [see Chapter 1]), it is challenging to perform measurements with a good signal to noise ratio. Indeed, in Fig. 3.7, the blue line corresponds to the spectrum of a backscattered wave at the output of the circulator (with the Raman pump switched off) and one can notice that it is in fact below -40 dBm, which is very weak. With the detection scheme 2, we introduced an amplifier (EDFA 2) at the output of the circulator which is specifically designed for the amplification of very weak signal (typically around -40 dBm). The red dashed line in Fig. 3.7 corresponds then to the spectrum of the backscattered wave at the output of this amplifier. While this allows a gain of around 25 dB, we observe that the signal to noise ratio (SNR) is degraded. However this reduction of SNR is not too detrimental. In fact one has to remind that we perform heterodyne measurements. Without EDFA 2, the local oscillator power is then very big compared to the one of the backscattered signal and it seems to be the main contributor to the noise on our measurements while with amplification the main source of noise comes from the backscattered signal. Fig. 3.7 also shows the amplified backscattered signal (green line) when the Raman amplification is switched on and one can see that it almost does not affect the noise background, which increases by less than 1 dB. While we display in Fig. 3.7 the backscattered signal for a sequence of strong pulses only, the final SNR of our measurements will depend on the weak pulses. Moreover, the bandwidth of our detection at 600 MHz being around 10 MHz, it will further improves the SNR. For an input composed of three waves (a 450 mW pump and a signal/idler -20 dB below and detuned by 35 GHz from the pump) we achieve a SNR of about 25 dB for the pump and 5 dB for the signal/idler.

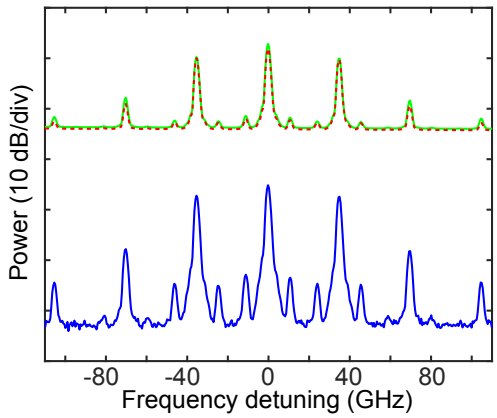

Figure 3.7: Spectrum of the backscattered signal at the output of the circulator with the Raman pump switched off (solid blue line) and at the output of EDFA 2 with the Raman pump switched off (red dashed line) and on (green line). Only strong pulses are launched into the fibre.

The spectra in Fig. 3.7 allow us to characterize the presence or not of any SBS [7, 34]. Indeed, we observe on these spectra two sidebands detuned by 10.9 GHz around each optical components involved in the FPUT process. These sidebands result mainly from spontaneous Brillouin scattering. One can notice that the amplitude of the Stokes sidebands is higher than the one of the anti-Stokes which is a sign of SBS but the difference is small (less than 1 dB). Moreover, if we focus for instance on the sidebands surrounding the pump, their level is about -16.5 dB lower, which is very weak when we recall that the backscattered pump is already lower by dozens of dB than the pump propagating forward. This means that SBS is negligible in our experiment. This was also checked by looking at the evolution of these sideband power when we increase the pump power, for which we get a linear relation, which confirms the mainly spontaneous nature of the scattering process.

Summary

- We recalled the state of the art concerning distributed measurements of MI in optical fibres and highlighted the advantages of OTDR-related techniques.
- We gave a general and detailed description of our experimental setup. We explained how the fading suppression technique and signal processing enable

clean measurements of the intensity and phase of the pump and signal components of the backscattered wave.

- We introduced and described a loss compensation scheme based on Raman amplification.

Chapter 4

Symmetry breaking of the Fermi-Pasta-Ulam-Tsingou recurrences

Contents

In chapter 2 we pointed out that the rich dynamics related to multiple recurrence cycles of MI such as spontaneous symmetry breaking is linked to separatrix (or homoclinic) crossing [75, 113, 114]. Yet, so far, such symmetry breaking has never been observed due to experimental limitations, the major one being the dissipation, which prevents the observation of multiple recurrences in fibre optics and which can also cause separatrix crossing, preventing the observation of both type of recurrences (inner and outer orbits in phase-planes or unshifted and shifted recurrences in the

time domain) as reported by Kimmoun *et al.* in a water tank experiment [37]. These limitations were lifted by the experimental setup we developed (described in Chapter 3). It allows us to perform distributed characterization in phase and in intensity of two FPUT recurrences thanks to an active compensation of the losses and to an heterodyne optical time-domain reflectometer. Hence, we report in this chapter the observation of symmetry-breaking of FPUT recurrences. In the first section we detail the conditions for separatrix crossing. Then, we present in the second section experimental results highlighting both types of recurrences through phase-plane structures. We finally introduce in the last section a technique to reconstruct the temporal evolution of the field intensity and phase, thus allowing the observation of the symmetry-breaking in the time-domain.

4.1 Conditions for separatrix crossing

In chapter 2, we introduced in the framework of the 3WM model the Hamiltonian which describes the evolution of the system. Similarly to Fig. 2.4 we plot in Fig. 4.1 the level curves of the Hamiltonian but this time in the polar coordinates $(\Delta\Phi, \eta)$[1] and for $\omega = 1.20$ [Fig. 4.1(b)], close to the perfect phase-matching frequency ($\omega = \sqrt{2}$). The separatrix is highlighted with a thick black solid line. Moreover the dashed line corresponds to the projection of the trajectory of the AB [Eqs. (2.14)] on this phase plane. We notice that for vanishing modulation ($\eta \to 0$) both the 3WM separatrix and the AB emanate from the same value of $\Delta\Phi = \pm\Delta\Phi_c \simeq \pm 0.295\pi$. $\Delta\Phi_{init} = -\Delta\Phi_c$ corresponds to the unstable manifold (i.e. entailing growing modulations) and $\Delta\Phi_{init} = \Delta\Phi_c$ constitutes the stable manifold (entailing asymptotic conversion from the sidebands to the pump). Starting with a very weak modulation, one can then expect to observe inner trajectories (unshifted recurrences) for $-\Delta\Phi_c < \Delta\Phi_{init} < \Delta\Phi_c$ or $\pi - \Delta\Phi_c < \Delta\Phi_{init} < \pi + \Delta\Phi_c$ and outer orbits (shifted recurrences) for $\Delta\Phi_c < \Delta\Phi_{init} < \pi - \Delta\Phi_c$ or $\Delta\Phi_c - \pi < \Delta\Phi_{init} < -\Delta\Phi_c$. The separatrix crossing can then be obtained by switching $\Delta\Phi_{init}$. However, one has to take into account that the value of $\Delta\Phi_c$ depends on the modulation frequency ω.

[1] Note that the phase-plane configurations with the polar coordinates $(\Delta\Phi, \eta)$ and the cartesian coordinates $(\eta \times cos(\Delta\Phi), \eta \times sin(\Delta\Phi))$ give similar information. However, when talking specifically about the separatrix, it is easier to operate with the polar coordinates to infer the crossing conditions.

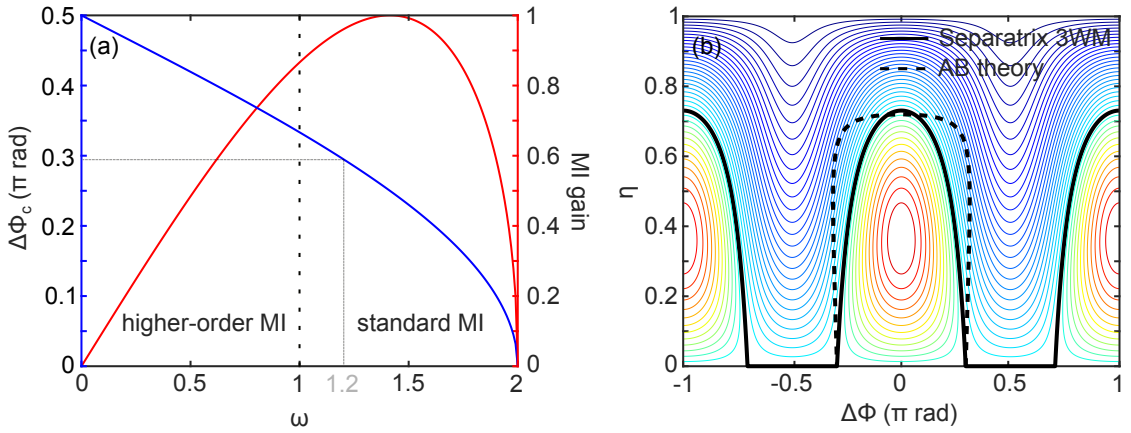

Figure 4.1: (a) Critical phase $\Delta\Phi_c$ versus normalised modulation angular frequency ω. (b) 3WM phase plane in polar coordinates $(\Delta\Phi, \eta)$. The thick black solid line corresponds to the 3WM separatrix and the dashed line corresponds to the Akhmediev breather theory.

In fact, as stated in Chapter 2 we have $\Delta\Phi_c = cos^{-1}(\omega/2)$. Hence, for $0 < \omega < 2$ (i.e modulation in the MI gain curve) $\Delta\Phi_c$ can range from 0 to $\pi/2$ as displayed in Fig. 4.1(a). Note that in this section we focus only on standard MI ($1 < \omega < 2$) and not on higher-order MI, which involves more complex separatrices. This means that, $\Delta\Phi_{init} = 0, \pm\pi$ always lead to inner orbits while $\Delta\Phi_{init} = \pm\pi/2$ always lead to outer orbits, fact we will use in the next section. This is true even for non-weak input modulation. In this case, the critical phase can only be obtained via numerical integration of the NLSE. The stronger is the modulation, the further away it is from analytical prediction. For instance, for the following parameters: $P_p = 490\,mW$, $\beta_2 = -19 \times 10^{-27} s^2/m$, $\gamma = 1.3 \times 10^{-3}/W/m$, initial signal/idler to pump ratio of -8.5 dB, $\omega = 1.20$ (i.e. $f = 35\,GHz$), the critical phase is $\Delta\Phi_{c-NLS} \backsimeq 0.337\pi$ (to be compared to 0.295π).

Instead of varying $\Delta\Phi_{init}$, another possibility to cross the separatrix is to change the initial sideband amplitude. Indeed, as can be seen in Fig. 4.1(b), at $\Delta\Phi = -\Delta\Phi_c$, the separatrix has a very high slope but which is not infinite. Thus, 3WM integration shows that for $\Delta\Phi_{init}$ superior but very close to $-\Delta\Phi_c$ it is possible to switch from inner to outer trajectories by increasing the initial sideband power fraction η_{init}. However, we notice that at the same point the slope of the AB has an opposite sign, which means that, in order to cross the separatrix by increasing

η_{init} one has to set $\Delta\Phi_{init}$ below $-\Delta\Phi_c$ and can expect to switch from outer orbits to inner orbits. Experimentally, this switching process is much more complicated than the previous one (by varying only $\Delta\Phi_{init}$) as it requires to be very close to the separatrix and large variations of η_{init}. Finally, we point out that the intrinsic losses along the propagation can also cause separatrix crossing. This was observed for the first time in a water tank experiment by Kimmoun *et al* [37]. Looking at multiple FPUT recurrences, they were only able to observe a phase-shifted recurrence as the attenuation strongly modifies the dynamics of the system, forcing the system to cross the separatrix. All these cases are illustrated with numerical simulations from the NLSE in Fig.4.2. Fig.4.2(a) shows a "reference" case of the spatio-temporal evolution of the field power for $\Delta\Phi_{init} = -0.32\pi$ (we remind that the critical phase in this case is $\pm 0.337\pi$). We clearly see that we observe unshifted recurrences is this case, associated to an inner trajectory in the phase plane [Fig.4.2(b)]. Starting from this reference we show that by varying $\Delta\Phi_{init}$ by a small amount (to -0.35π) we observe now π-shifted recurrences and an outer trajectory [Fig.4.2(c,d)]. The same observation can be made by decreasing η_{init} from 0.22 to 0.12 (i.e. changing the initial signal/idler to pump ratio from -8.5 dB to -11.5 dB) [Fig.4.2(e,f)]. Finally, separatrix crossing can also be induced by adding linear attenuation $\alpha = 0.2\,dB/km$ into the NLSE integrated numerically [Fig.4.2(g,h)]. In this case, the dissipation strongly modifies the dynamics of the system. In particular, we have seen with the 3WM model (see Eqs. 2.8) that the attenuation has a direct impact on the pump and sidebands power evolutions and thus on the accumulated nonlinear phase acquired by these waves.

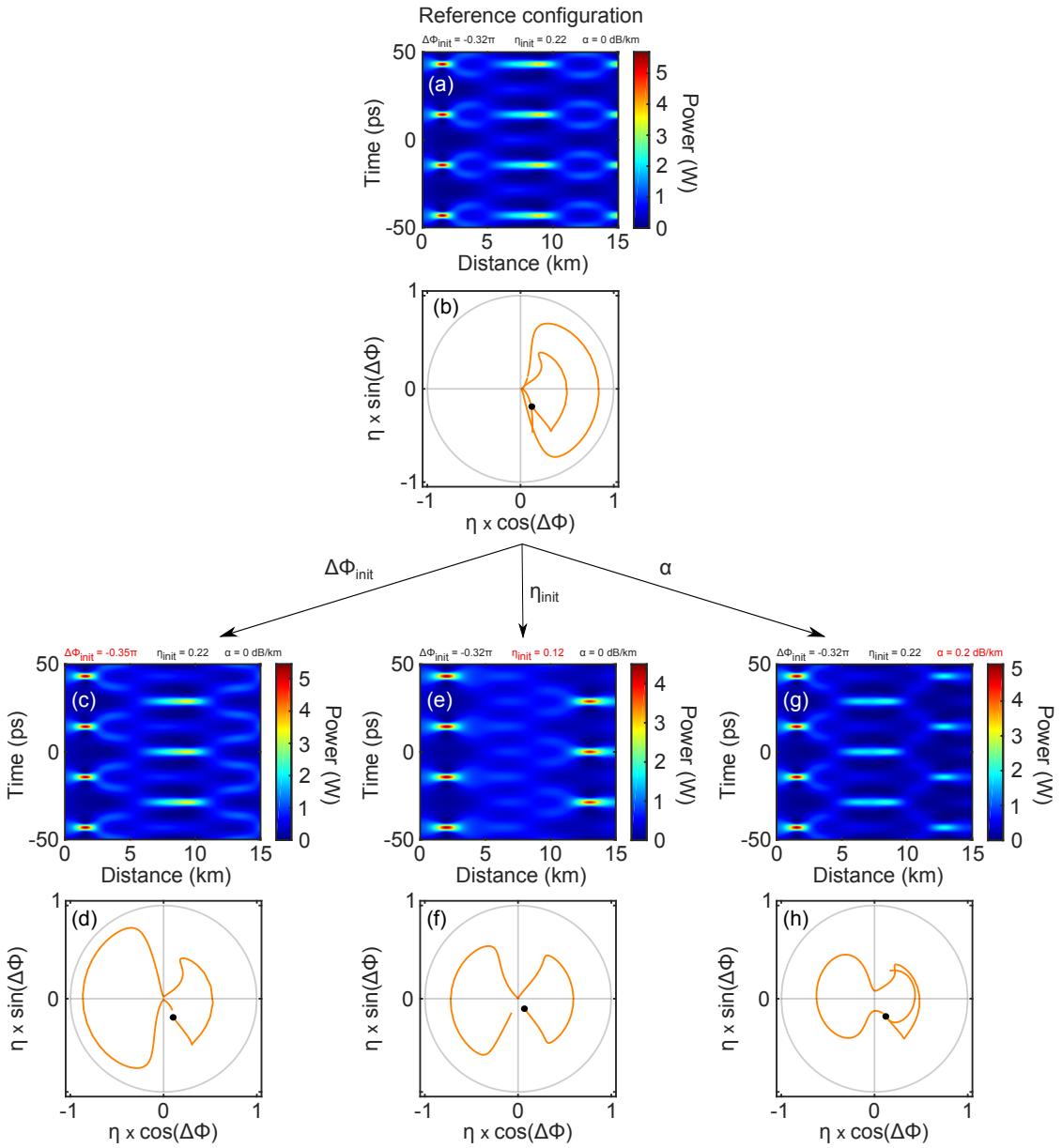

Figure 4.2: (a,b) Spatio-temporal evolution of the field power from numerical simulations from the NLSE and corresponding phase-plane with the following parameters: $P_p = 490\,mW$, $\beta_2 = -19 \times 10^{-27} s^2/m$, $\gamma = 1.3 \times 10^{-3}/W/m$, initial signal/idler to pump ratio of -8.5 dB ($\eta = 0.22$), $\omega = 1.20$ (i.e. $f = 35\,GHz$), $\Delta\Phi_{init} = -0.32\pi$. (c,d) Same but with $\Delta\Phi_{init} = -0.35\pi$. (e,f) Same than (a,b) but with an initial signal/idler to pump ratio of $-11.5\,dB$ ($\eta = 0.12$). (g,h) Same than (a,b) but adding the linear attenuation $\alpha = 0.2\,dB/km$.

4.2 Observation of symmetry-breaking via phase-plane structures

In this section we report the experimental observation of both type of recurrences via phase-plane structures.

4.2.1 Far from the separatrix

In the previous section we outlined the fact that that $\Delta\Phi_{init} = 0, \pm\pi$ always lead to inner orbits while $\Delta\Phi_{init} = \pm\pi/2$ always lead to outer orbits. Using the setup described in Chapter 3 we launched into a 7.7 km SMF-28 fibre a three-wave input with the following parameters : $P_p = 490\ mW$, $\beta_2 = -19 \times 10^{-27} s^2/m$, $\gamma = 1.3 \times 10^{-3}/W/m$, initial signal/idler to pump ratio of -8.5 dB, $\omega = 1.20$ (sideband detuning from the pump of 35 GHz) and $\Delta\Phi_{init} = 0$ or $\Delta\Phi_{init} = -\pi/2$. One can wonder why we did not chose, $\omega = \omega_{max} = \sqrt{2}$, which corresponds to the perfect phase-matching normalised frequency detuning. This is because the pump power we use in experiments ranges usually between 450 mW and 500 mW (in order to observe two FPUT recurrences in the 7.7 km fibre). This range of pump power entitles f_{max} ranging from 40 GHz to 42 GHz. Yet we recall that, experimentally, we generate the signal and idler sidebands via phase modulation [see Fig. 3.1]. The RF signal driving the PM is provided by a synthesizer which can deliver RF signal up to 20 GHz and is followed by a frequency doubler. Then, the maximum driving frequency we can deliver to the PM is 40 GHz. Because this constitutes an upper limit, we set f to 35 GHz to ensure a stable driving RF signal. Note that this is not a drawback as the processes studied in this thesis do not require an initial perfect-phase matching. Moreover, although one would ideally use very weak modulation, it entitles large recurrence distances (about 20 km to observe two recurrences for the previous parameters but with an initial signal/idler to noise ratio of -20 dB). This is not compatible with a good compensation of losses via our Raman compensation scheme which was designed for fibre length around 8 km which is the reason why we operate with an initial signal/idler to pump ratio of -8.5 dB. Figure 4.3 then displays the experimental recordings (solid lines) of the longitudinal pump, signal power and relative phase evolutions as well as the corresponding phase-plane trajectories for both value of $\Delta\Phi_{init}$. Note that we do not measure the evolution of

the idler component as it is similar to the signal one, the spectrum being symmetric relatively to the pump. For $\Delta\Phi_{init} = 0$, we observe more than two recurrences cycles

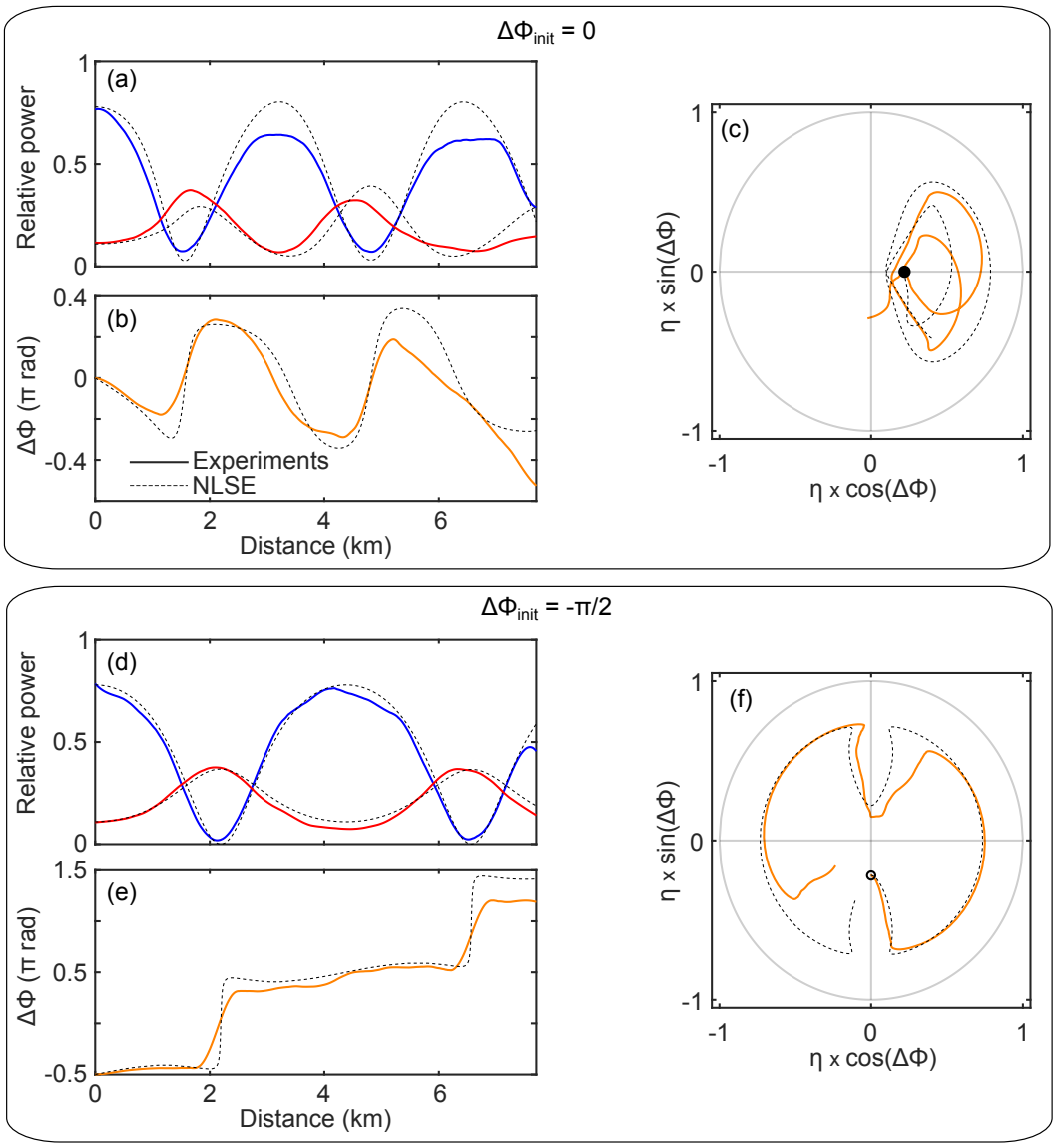

Figure 4.3: (a,d) Longitudinal evolution of the pump (blues lines) and signal (red lines) powers and (b,e) longitudinal evolution of the relative phase. (c,f) Projections in the 3WM phase-plane. Solid lines correspond to experimental recordings and dashed ones to numerical simulations from the NLSE. Initial conditions in (a-c) and (d-f) differ only in the initial relative phase $\Delta\Phi_{init} = 0$ or $\Delta\Phi_{init} = -\pi/2$, respectively.

in power [Fig. 4.3(a)] and almost two cycles for $\Delta\Phi_{init} = -\pi/2$ [Fig. 4.3(d)]. Both

cases show a good agreement with numerical simulations (dashed lines), with almost perfect recurrences for $\Delta\Phi_{init} = -\pi/2$. The discrepancies in the case $\Delta\Phi_{init} = 0$ can partly be attributed to the strong modulation used in the experiment. In particular, this is because the doubly periodic analytical solution of the NLSE describing "perfect" multiple recurrences do not reduce to only three waves, especially in the case $\Delta\Phi_{init} = 0$, thus leading to non-perfect recurrences in experiments and simulations (see Appendix A for more details). The relative phase evolutions [Figs. 4.3(b,e)] show also a good agreement with numerical simulation apart for the last hundred of meters for $\Delta\Phi_{init} = 0$. The phase-plane projections in Figs. 4.3(c,f) clearly reveal the two types of orbits expected. For $\Delta\Phi_{init} = 0$ [Fig. 4.3(c)] we observe an inner trajectory confined in the right semi-plane (if we neglect the small discrepancy at the end) while for $\Delta\Phi_{init} = -\pi/2$ [Fig. 4.3(f)] we observe an eight trajectory going on both sides of the phase-plane. This illustrates the homoclinic crossing and symmetry-breaking of the recurrence process.

4.2.2 Close to the separatrix

Here we give further evidence of homoclinic crossing by operating with the same parameters than the previous ones but with an initial relative phase $\Delta\Phi_{init}$ very close to the critical phase $\Delta\Phi_{c-NLS} = 0.337\pi$. Note that in this case the measurements are very challenging, as the spatial period of the recurrences tends to diverge when the critical phase is approached and the measurements become more sensitive to the stability of the experiment. Nonetheless, we obtained very good results as displayed in Figure 4.4 which shows the same kind of measurements than in Fig. 4.3 but with $\Delta\Phi_{init} = -0.32\pi$ [Figs. 4.3(a-c)], $\Delta\Phi_{init} = -0.34\pi$ [Figs. 4.3(d-f)] and $\Delta\Phi_{init} = -0.37\pi$ [Figs. 4.3(g-i)]. For $\Delta\Phi_{init} = -0.32\pi$ we observe a bit more than one recurrence and an inner trajectory in the phase-plane. By varying the initial relative phase of only 0.05π to $\Delta\Phi_{init} = -0.37\pi$ we clearly observe one and a half recurrence and an outer trajectory in the phase plane so the separatrix have effectively be crossed. Concerning the intermediate case with $\Delta\Phi_{init} = -0.34\pi$, one can hardly identify the type of trajectory from the phase plane as the second recurrence is almost out of the range of the fibre. This is because $\Delta\Phi_{init}$ is then almost equal to $\Delta\Phi_{c-NLS}$.

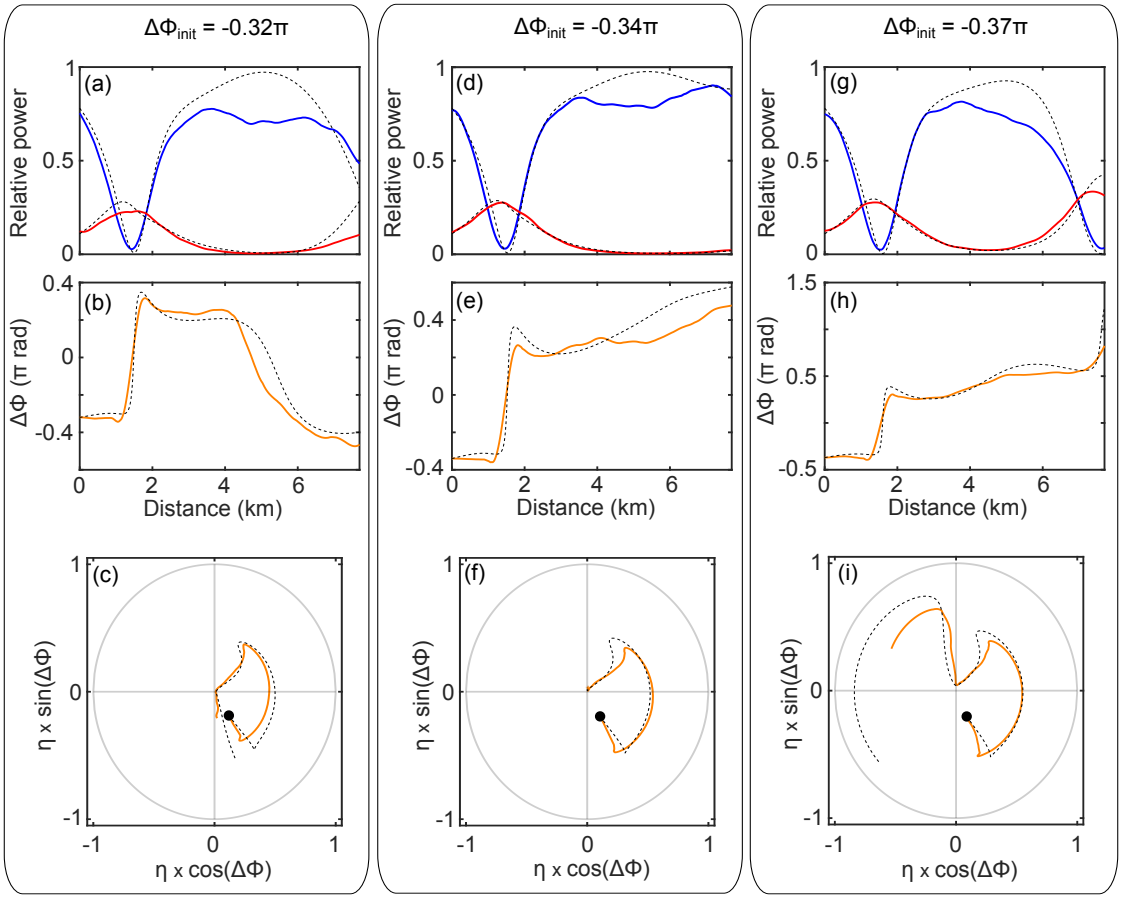

Figure 4.4: (a,d,g) Longitudinal evolution of the pump (blues lines) and signal (red lines) powers and (b,e,h) longitudinal evolution of the relative phase. (c,f,i) Projections in the 3WM phase-plane. Solid lines correspond to experimental recordings and dashed ones to numerical simulation from the NLSE. Initial conditions in (a-c), (d-f) and (g-i) differ only in the initial relative phase: $\Delta\Phi_{init} = -0.32\pi$, $\Delta\Phi_{init} = -0.34\pi$ and $\Delta\Phi_{init} = -0.37\pi$, respectively.

4.3 Observation of symmetry-breaking in the time domain

Although we were able to observe the symmetry-breaking of the FPUT recurrences via phase-plane structures, we wondered if, with a similar setup, it would be possible to do this observation in the time domain, which would be more meaningful. This is not an easy task as it would require to perform distributed characterization of structures which can be as short as a few picoseconds at the maximum compression points. This rules out the possibility to use direct photo-detection which is currently limited to intensity measurements with a resolution of tens of picoseconds. Nonetheless, numerous techniques have been developed in the last decades in order to measure such short pulses, the more famous being frequency-resolved optical gating [115] and spectral phase interferometry for direct-electric field reconstruction [116] (a review can be found in Ref. [117]). Apart from these now conventional techniques, new methods allowing real-time full-field characterisation have recently be developed, based in particular on time lens and/or dispersive Fourier transform [118–122]. For instance Tikan *et al*. [120] reported the full-field characterisation of 80 fs Peregrine soliton-like structures. However, all these previous techniques [115–117, 120–122] are limited to localised measurements and cannot be then implemented in our case. Note that Xu *et al*. [99] reported recently the longitudinal full-field characterisation of Peregrine-like structures using a combination of temporal and spectral measurements and a reconstruction algorithm but this technique suffers from the same limitations than the cut-back one described in Chapter 3. Based on our HOTDR setup, we implemented a new method to perform fast and non-invasive full-field characterisation of time-periodic pulses (i.e. with discrete line spectra) along the whole length of an optical fibre. In this section, we present the principle of this method and its setting up to observe the symmetry-breaking of FPUT recurrences in the time domain. The same technique will be used in Chapter 6 to characterise higher-order breathers.

4.3.1 Principle of reconstruction of the spatio-temporal field intensity and phase

We have shown previously that the HOTDR setup allows to perform a distributed

characterisation in the frequency domain. Because we have both intensity and phase measurements of frequency components, one could simply use the inverse Fourier transform to get the temporal evolution. However, in our case, we only measure a truncated spectrum as we focus on the three main spectral components (i.e the pump and signal/idler). To understand the impact of this truncation on the reconstruction we performed numerical simulations to get the full spectral evolution and then we calculate the spatio-temporal field intensity and phase via inverse Fourier Transform by taking into account a varying number of spectral components. In order to compare these results, we defined the following relative least square error parameter :

$$\epsilon = \sqrt{\frac{\sum_{i,j} |P_{Full}(z_i, T_j) - P_{Trunc}(z_i, T_j)|^2}{\sum_{i,j} |P_{Full}(z_i, T_j)|^2}} \tag{4.1}$$

where P_{Full} and P_{Trunc} are the matrix of the spatio-temporal power with the full spectrum accounted for or the truncation, respectively. Figure 4.5 shows then the evolution of ϵ as well as the spatio-temporal power plots for different number of waves accounted for in the reconstruction. As can be seen, ϵ follows an exponential decreasing. Increasing the number of waves from three to five reduced the error by a factor four. This has really a big impact on the spatio-temporal power profile as displayed in Figs. 4.5 (b) and (c). In fact, with the three-wave reconstruction we notice that we can observe the recurrence but it is of very poor quality, with maximum compression points split into two parts longitudinally [to be compared with the spatio-temporal power plot with the full spectrum accounted for in Fig. 4.5 (e)]. With five waves, the split disappears, and the reconstruction is far more accurate. Increasing to seven waves, the error can also be reduced by another factor four but we can see in Fig. 4.5 (d) that it makes less a difference.

4.3.2 Experimental implementation and results

We just saw that the distributed characterisation of at least fives waves (i.e. the pump, signal/idler and their first harmonics) is necessary to get a relatively accurate spatio-temporal profile. Hence, we had to modify our experimental setup which was designed to measure only three waves. Most major changes consist in the implementation of a new detection scheme as displayed in Fig. 3.1 (detection scheme 2 instead

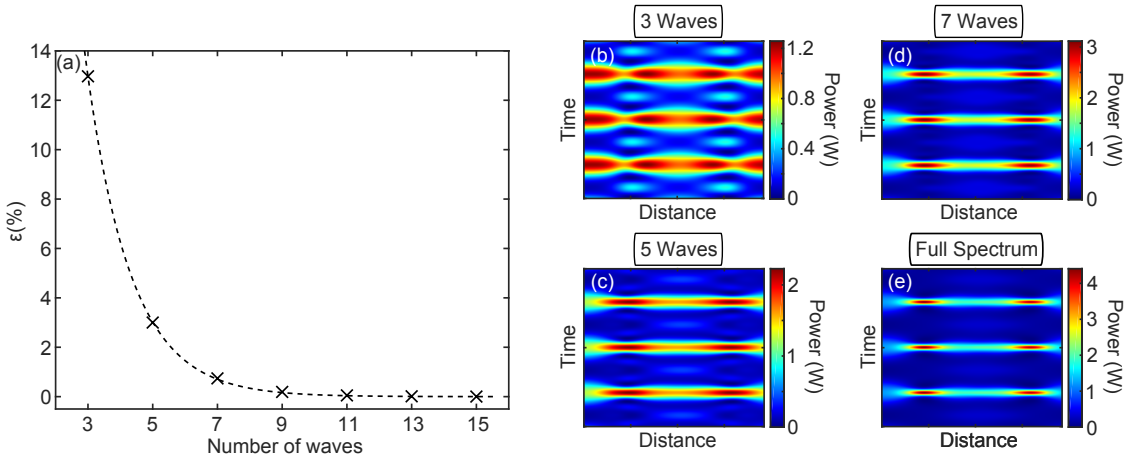

Figure 4.5: (a) Error on the spatio-temporal power field reconstruction versus number of waves accounted for in the reconstruction. The dashed line is an exponential fit. (b-e) Spatio-temporal evolution of the power field from numerical simulations from the NLSE, by accounting for three, five, seven waves and the full spectrum, respectively.

of detection scheme 1). In particular, detection scheme 2 introduced a new EDFA amplifier specifically designed to amplify very weak signals which is then suitable for the amplification of the Rayleigh backscattered signal (note that several minor changes on the setup are not reported in Fig. 3.1). These modifications have allowed an improvement of the SNR of our measurements by more than 10 dB compared to our first results on the symmetry-breaking reported in Ref. [42]. Thus, it enables the detection of a supplemental set of sidebands, harmonics of the signal and idler waves. However, in order to detect this supplemental set of sidebands we can no longer use a three-wave input. In fact, we explained in Chapter 3 that we use a sequence of strong and weak pulses to perform our measurements. Concerning the strong ones, with a three-wave input, the harmonics would be generated through nonlinear effects but for the weak pulses theses harmonics are not generated. Hence, we could not perform the necessary calibration for these frequencies (to eliminate the fading effect). To detect the spectral component it is then necessary that they are already present in the input condition that we launch in the fibre. Because the response time of the Waveshaper is too long compared to the duration between a strong and a weak pulse (a few seconds compared to $102\,\mu s$) we cannot design different input profiles for the strong and weak pulses. Both have then to be constituted

of five waves. The input parameters were then chosen as follows : $P_p = 460\,mW$, $\beta_2 = -19 \times 10^{-27} s^2/m$, $\gamma = 1.3 \times 10^{-3}/W/m$, initial signal/idler to pump ratio of -10 dB and harmonics to pump ratio of -20 dB, $\omega = 1.24$ (signal/idler detuning from the pump of 35 GHz and harmonics detuning from the pump of 70 GHz) and the initial phase of the five waves is set to 0. Here, the power of the first harmonics of signal/idler waves is chosen as small as possible in order to be the closest possible to a three-wave input. Like previously, we assume that the behaviour of sidebands symmetric to the pump is similar (the impact of odd-order dispersion terms and Raman effect being negligible). Thus, we only record the evolution of the pump, signal and its first harmonic as displayed in Fig. 4.6, which shows the simulated input spectrum [Fig. 4.6(a)] and the longitudinal power [Fig. 4.6(b)] and phase evolutions [Fig. 4.6(c)]. Note that the arbitrary phase of the local oscillator is set here to zero (we checked numerically that this phase has no consequence on the dynamics). As we can see in Fig. 4.6(b), the experimental power evolution exhibit two recurrences, in good agreement with numerical simulations.

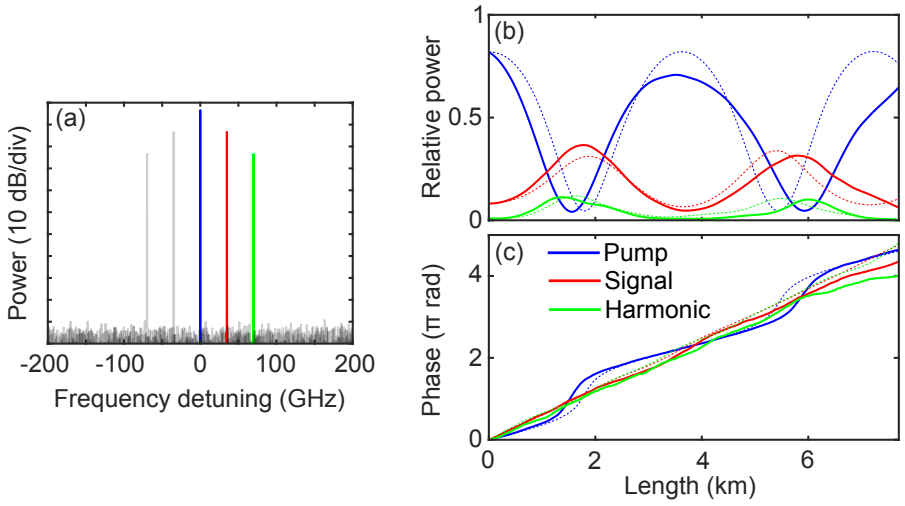

Figure 4.6: (a) Simulated input spectrum. Longitudinal evolution of the power (b) and phase (c). Blue, red and green correspond to the pump, signal and harmonic, respectively. In (b,c) the solid lines correspond to experiments and the dashed ones to numerical simulations from the NLSE. Parameters: $P_p = 460\,mW$, $\beta_2 = -19 \times 10^{-27} s^2/m$, $\gamma = 1.3 \times 10^{-3}/W/m$, initial signal/idler to pump ratio of -10 dB and harmonics to pump ratio of -20 dB, signal/idler detuning 35 GHz from the pump, harmonics detuning 70 GHz from the pump.

We then calculate the spatio-temporal evolution of the field via the inverse Fourier transform from the five waves. The intensity plot is displayed in Fig. 4.7(b) and exhibits two maximum compression points at about 1.5 km and 6 km, respectively, which are in phase with each other, as expected (here $\Delta\Phi_{init} = 0$). This is in good overall agreement with the results obtained from numerical simulations accounting for the full spectrum and displayed in Fig. 4.7(a). To get a more accurate comparison we plotted the temporal and longitudinal evolutions along the first maximum compression point [see magenta dashed lines in Fig. 4.7(a,b)] in Fig. 4.7(c) and 4.7(d), respectively. Experimental traces are displayed in red and numerical ones in blue and look very similar. The latter only exhibits higher amplitude and slightly sharper fronts (one can notice that the temporal profile is very similar to the one of a maximally compressed AB as shown in Fig. 2.6). The main cause for this discrepancy is the truncation which is confirmed by the black dashed lines in Fig. 4.7(c,d). They are obtained by only accounting for five waves in the inverse Fourier transform calculation in numerical simulations. We can clearly see that the agreement with the experiments is then pretty good. The inverse Fourier transform also gives us access to the spatio-temporal evolution of the phase of the field. They are displayed in Fig. 4.7(e,f). Experimental evolution is in very good agreement with numerical simulations, the impact of the truncation being less pronounced in this case, as confirmed by the phase evolutions along the first maximum compression point in Fig. 4.7(g,h). Noteworthy, in the temporal case [Fig. 4.7(g)], we observe a phase jump close to π between the center of the pulses and their wings and equal to π in simulations which is one of the characteristic feature of the AB and PS [28].

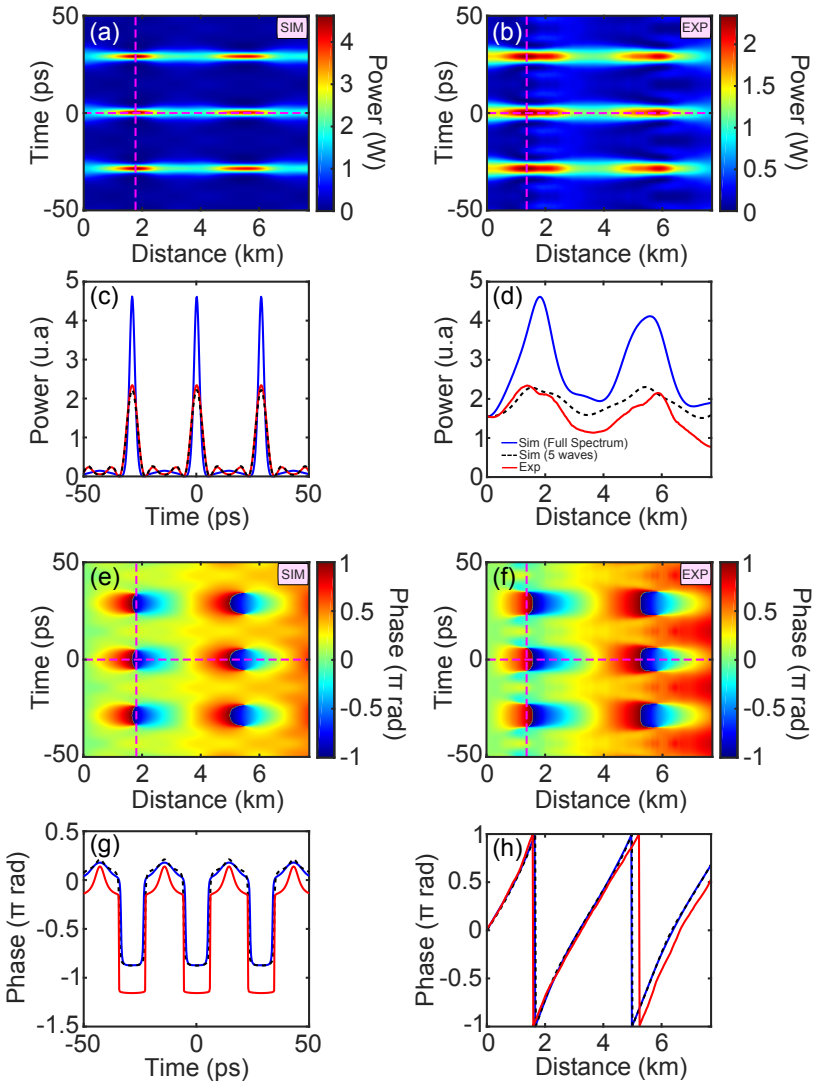

Figure 4.7: Spatio-temporal evolution of power [(a) numerical simulations, (b) experiments] and phase [(e) numerical simulations, (f) experiments)]. (d), (h) Longitudinal evolution of power and phase at the first maximum compression point (along the magenta dashed line). (c), (g) Temporal evolutions at this point. The red lines correspond to experiments, the blue ones to numerical simulations with the full spectrum accounted for in the inverse Fourier transform calculation and the black ones to numerical simulations with a truncated spectrum (5 waves). Parameters are similar to those in Fig. 4.6.

In a second set of experiments, we reproduced the experiment with the same five-wave input except for a phase of π (instead of zero) for the idler component in order to induce the separatrix crossing. Indeed in this case Eq. (2.9) gives $\Delta\Phi_{init} = -\pi/2$. Experimental results are displayed in Fig. 4.8(b,d). In this case, we still observe two maximum compression points but with a π phase shift between them, thus illustrating the symmetry-breaking of the recurrences in the time domain. The agreement with numerical simulations [Fig. 4.8(a,c)] is good.

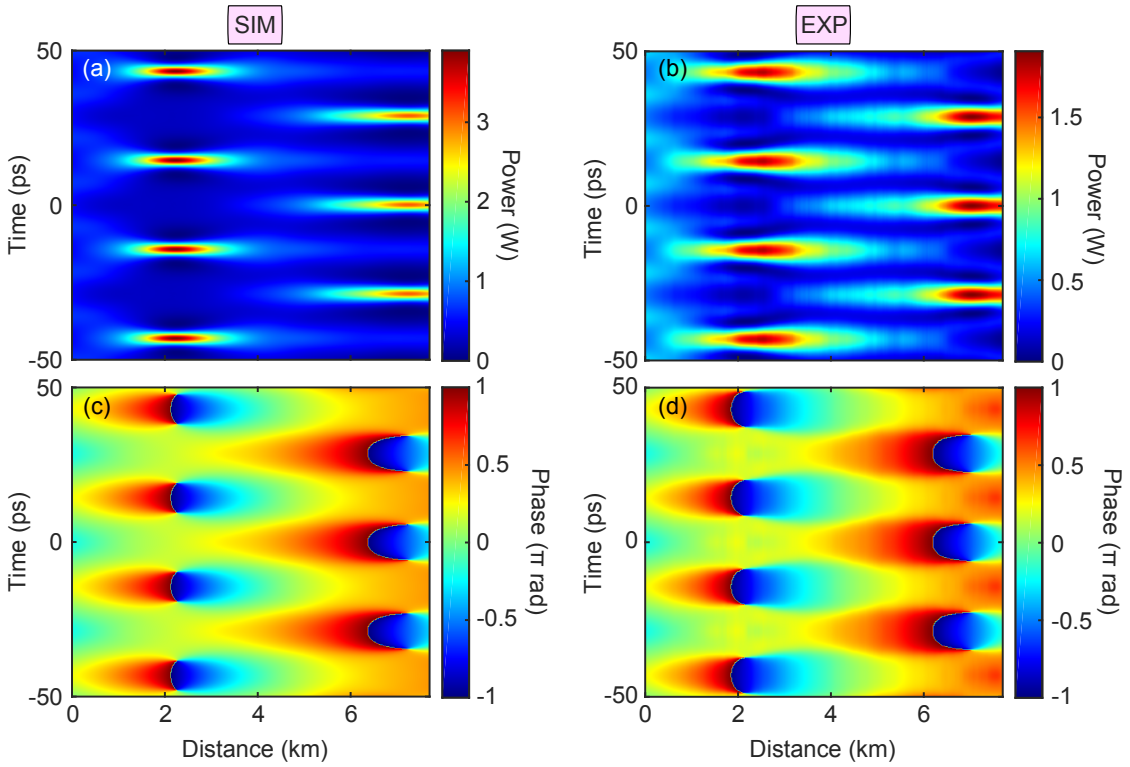

Figure 4.8: Spatio-temporal evolution of power [(a) numerical simulations, (b) experiemets] and phase [(c) numerical simulations, (d) experiments)]. Parameters are similar to the ones in Fig. 4.6 except for an inital phase of π for the idler wave.

Summary

- We discussed the conditions to observe the symmetry-breaking of the recurrences. We showed that separatrix crossing can be induced by varying the initial relative phase between the modulation sidebands and the pump, by varying the initial modulation amplitude and also by introducing dissipation.
- Using the setup described in the previous chapter we outlined the experimental observation of two recurrences and in particular of two types of qualitatively different phase-plane trajectories (inner and outer trajectories), thus illustrating experimentally the symmetry-breaking of FPUT recurrences.
- We described a method allowing the calculation of the spatio-temporal evolution (at the picosecond scale) of the field via measurements from our setup. To illustrate its performance we reported the observation of the symmetry-breaking of the recurrences in the time domain.

Chapter 5

Impact of initial conditions on Fermi-Pasta-Ulam-Tsingou recurrences

Contents

In chapter 4, we focused on the impact of the initial three-wave input parameters on the type of recurrence observed (unshifted or π-shifted recurrences). However, the modulation sidebands initial parameters have also an important influence on the position of these recurrences which we will describe in this chapter. In the first section we introduce a recent analytical model by Grinevich and Santini [45] which allows to estimate these positions. These predictions have recently been verified successfully in a spatial MI experiment using a bulk photorefractive crystal [64] but never in fibre optics. Then, in the second section we report the experimental investigation (using the setup described previously) of the impact of the initial conditions of the modulation sidebands, in comparison with the previous analytical model and numerical simulations.

5.1 Grinevich and Santini model

In chapter 2 we discussed several approaches allowing to describe the nonlinear stage of MI and the recurrences. Especially, we pointed out that the AB model is limited as it depicts only a single recurrence and does not allow to account for the initial relative phase. Recently, by applying asymptotic matching expansion techniques (in the framework of the AB theory), Grinevich and Santini [45] managed to derive simple formulas which allow to characterise the dependence of the first maximum compression point as well as the spatial period of the recurrence on the parameters of the three-wave input. In fact, considering a three-wave input as follow :

$$E(z=0,T) = \sqrt{P_p}\left(e^{i\varphi_p} + c_s e^{i\Omega T} + c_i e^{-i\Omega T}\right) \tag{5.1}$$

where P_p is the pump power, Ω the angular frequency detuning, $c_{s,i} = |c_{s,i}|\, e^{i\varphi_s}$, where $|c_{s,i}| \ll 1$ are the normalised amplitude of the signal and idler wave, respectively, and φ_s their phase, they derived the position Z_1 of the first maximum compression point and the spatial period Z_{rec}:

$$Z_1 = \frac{2}{g} ln\left(\frac{g^2}{2\,|\alpha|}\right) \times L_{NL} \tag{5.2}$$

$$Z_{rec} = \frac{4}{g} ln\left(\frac{g^2}{2\sqrt{|\alpha\beta|}}\right) \times L_{NL} \tag{5.3}$$

where $g = \omega\sqrt{4-\omega^2}$ (related to the parametric MI gain), $\alpha = c_s^* - e^{i2\Phi_\omega} c_i$ and $\beta = c_i^* - e^{-i2\Phi_\omega} c_s$ with $\Phi_\omega = cos^{-1}(\omega/2)$ and L_{NL} is the nonlinear length. Then the position Z_n of the n-th recurrence is given by $Z_n = Z_1 + n \times Z_{rec}$. Here, we recognize that Φ_ω corresponds to the critical phase of the 3WM model and phase of the AB. Note that the formula of Z_1 encompasses the one derived by Erkintalo *et al* [90] (which corresponds to the case $\Delta\Phi_{init} = -\Phi_\omega$). In the following, the position Z_n of the recurrences will be deduced from those of the pump power minima. In fact, as shown in Chapter 2, they nearly coincide with the position of the maximum compression points. Compared to the 3WM model, these formulas offer a better quantitative approximation of the recurrence positions, especially for weak modulations. To justify this, we plot in Figure 5.1 the positions of the first two lo-

cal minima of the pump power (green for the first one and magenta for the second) versus the initial signal/idler to pump ratio (varied from -30 dB to -5 dB) for the typical parameters used in experiments: $P_p = 470\,mW$, $\beta_2 = -19 \times 10^{-27} s^2/m$, $\gamma = 1.3 \times 10^{-3}/W/m$, $\omega = 1.22$ (sideband detuning from the pump of 35 GHz) and $\Delta\Phi_{init} = 0$. The positions were calculated using three different approaches.

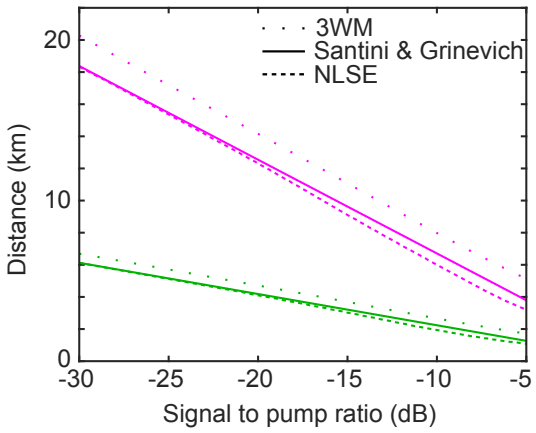

Figure 5.1: Position of the first (in green) and second (in magenta) pump minima versus signal/idler to pump ratio. Dotted and dashed lines correspond to numerical simulation from the 3WM model and the NLSE, respectively, and solid lines correspond to the theoretical model of Santini and Grinevich [Eqs. (5.2) & (5.3)].

Here, the solid lines correspond to Eqs. (5.2) & (5.3) while the dotted and dashed lines correspond to numerical simulations from the 3WM model (Eqs. 2.8) and the NLSE, respectively. In every cases we observe a logarithmic or quasi-logarithmic dependence of the position on the modulation intensity. Thus, the first and second minima ranges from about 1 km to 7 km or 3 km to 20 km, respectively. In particular, we observe an "error" almost constant between the NLSE and the 3WM model, the estimation from the latter on the first pump minima position being about 600 m larger for the whole range of signal to pump ratio considered. For the second minima, the discrepancy is even higher, about 1.9 km. Conversely, Eqs. (5.2) & (5.3) give very a good approximation of the positions with a maximum discrepancy of about 200 m and 750 m for the first and second minima, respectively. We notice a trend that the smaller the initial modulation, the better the estimate from (5.2) & (5.3), with almost a perfect agreement when the signal to pump ratio is -30 dB. This is consistent with the fact that the model of Grinevich and Santini have been

derived assuming a weak modulation.

5.2 Experimental study of the impact of initial conditions

5.2.1 Impact of the initial modulation phase

In order to characterise the impact of the initial relative phase on the recurrence positions, we used the following symmetric three-wave input: $P_p = 470\,mW$, $\beta_2 = -19\times10^{-27}s^2/m$, $\gamma = 1.3\times10^{-3}/W/m$, $\omega = 1.22$ (sideband detuning from the pump of 35 GHz) and a signal/idler to pump ratio of -10.4 dB. $\Delta\Phi_{init}$ was varied from $-\pi/2$ to $\pi/2$. Compared to previous experiments, the fibre length has been increased to 9.2 km in order to investigate the dynamics over a larger fibre length range. The results displayed in Fig. 5.2(a) show the positions of the first and second pump minima in green and magenta, respectively. Crosses account for experimental recordings, solid lines for the analytical predictions based on Eqs (5.2) & (5.3) and dashed ones to numerical simulations from the NLSE. As we can see, Eqs (5.2) & (5.3) predict that the positions Z_1 and Z_2 diverge both for $\Delta\Phi_{init} = \Phi_\omega = 0.29\pi$. As mentioned in section 4.1 this is because this particular phase corresponds to the stable manifold of the separatrix, which entails asymptotic conversion from the input sidebands to the pump. Conversely, Z_1 is minimum for $\Delta\Phi_{init} = -\Phi_\omega$, which entails the most rapid growth of the sidebands to the apex. Note that Z_2 still diverges for this phase value since backconversion still occurs asymptotically along the separatrix. The phase $\pm\Phi_\omega$ being the critical phase of the system, one could expect to observe transition from inner to outer trajectory across this phase. However, as discussed previously in Chapter 4, the relatively strong modulation used in our experiment and NLSE simulations (the sidebands contains about 15% of the total power) induces a shift of the critical phase which is here $\Delta\Phi_{c-NLSE} = \pm0.32\pi$. The yellow and cyan shaded areas correspond then to the range of $\Delta\Phi_{init}$ for which one could expect to observe outer and inner trajectory, respectively. The measured values of Z_1 are in excellent agreement with the numerical simulations and three different recordings are reported in Fig. 5.2(b-g) [solid lines correspond to experiments and dashed one to numerical simulations] to illustrate the dynamics. For an input phase of $\Delta\Phi_{init} = -0.42\pi$

[Fig. 5.2(b,c)] we observe then an outer trajectory. On the contrary, for $\Delta\Phi_{init} = -0.15\pi$ and $\Delta\Phi_{init} = 0.30\pi$ [Fig. 5.2(d,e) and (f,g), respectively], we observe inner trajectories. Note that another general comment can be done on the early stage of the propagation along the fibre. Indeed, initially, the power can either flow from the pump to the sidebands or the opposite, leading to an initial amplification or attenuation of the signal component. In Chapter 2 we stated that this is ruled by the sign of $sin(2\Delta\Phi_{init})$. This is confirmed here in all our experimental recordings and it can be observed in Fig. 5.2(b,d,f). In fact, for the cases shown in Fig. 5.2(b,d) ($\Delta\Phi_{init} = -0.42\pi$ and $\Delta\Phi_{init} = -0.15\pi$, respectively), $sin(2\Delta\Phi_{init})$ is negative, leading to an initial amplification of the signal and an attenuation of the pump. Conversely, for $\Delta\Phi_{init} = 0.30\pi$ [Fig. 5.2(f)] $sin(2\Delta\Phi_{init})$ is positive, inducing an initial attenuation of the signal and amplification of the pump. Finally, we notice that the measured values of Z_1(about $2\,km$ to $6\,km$) and Z_2 (about $7\,km$ to $9\,km$) agree relatively well with the estimates of Eqs (5.2) & (5.3), especially for

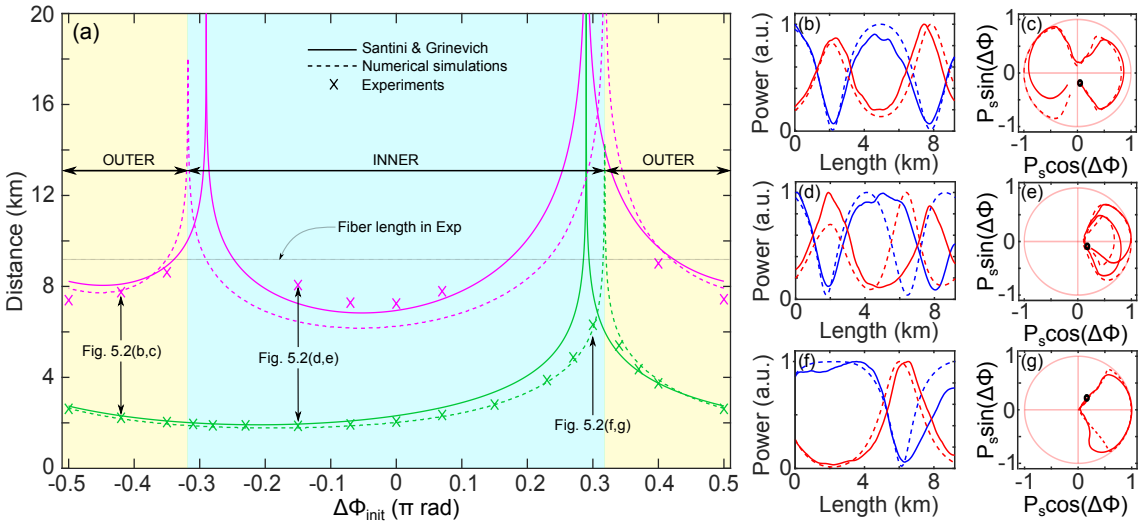

Figure 5.2: (a) Positions of the first (green) and second (magenta) pump minima. The crosses correspond to experimental recordings, dashed lines to numerical simulations from the NLSE and solid lines to the theoretical model [Eqs. (5.2) & (5.3)]. (b,d,f) Longitudinal evolution of the pump (blue) and signal (red) powers and (c,e,g) their corresponding phase plane trajectories, for $\Delta\Phi_{init} = -0.42\pi$, $\Delta\Phi_{init} = -0.15\pi$ and $\Delta\Phi_{init} = 0.30\pi$. Solid lines correspond to experiments and dashed ones to numerical simulations. The grey line indicates the length of the fibre used in experiments. All power plots are normalised to their maxima.

the position of the first pump minima. Concerning the second pump minima, the larger discrepancy between experiments and numerical simulations [magenta crosses and dashed lines in Fig. 5.2(a)] can be attributed to an imperfect compensation of the losses. Indeed, because the finite fibre length in our experiment fixes an upper bound to measurable distances [see grey line in Fig. 5.2(a)], we increased it to 9.2 km (to be compared to 7.7 km previously) to be able to observe more dynamics, at the expense of the compensation of the losses, which was designed and works better for a length of 7.7 km. Generally, improving the resolution would require a more complex loss compensation scheme, enabling in particular the use of longer fibre and then a better characterisation close to the separatrix.

5.2.2 Impact of the initial modulation amplitude

After investigating the influence of $\Delta\Phi_{init}$ on the recurrence positions, we set it to $\Delta\Phi_{init} = 0$ and studied the influence of the input sidebands amplitude, first in the symmetric case and then in the asymmetric one.

The symmetric case

In this case, the signal/idler to pump ratio was varied from -5 dB to -30 dB and we recorded the positions of the first and second pump minima, which are displayed in green and magenta in Fig. 5.3. Crosses accounts for experiments, dashed lines for numerical simulations from the NLSE and solid ones for theoretical predictions from Eqs (5.2) & (5.3). This figure is then similar to 5.1, except that the experimental results are added. Experimental recordings of Z_1 are found to be in very good agreement with numerical simulations and a quasi-logarithmic dependence of the position on the modulation intensity is indeed obtained. Note that, experimentally, we could not go lower than a signal/idler to pump ratio of about -26 dB as it constitutes the detection limit of our setup. Concerning Z_2, only two experimental points lied under the 9.2 km length of the fibre (marked by the grey line in Fig. 5.3) and they are in excellent agreement with numerical simulations.

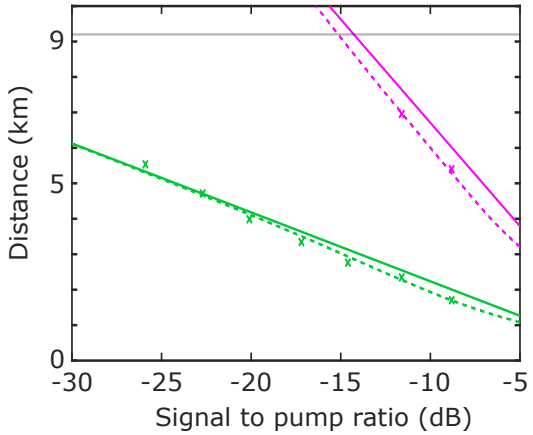

Figure 5.3: Position of the first (in green) and second (in magenta) pump minima versus signal/idler to pump ratio. Crosses correspond to experimental recordings, dashed lines to numerical simulation the NLSE, and solid lines to the theoretical model [Eqs. (5.2) & (5.3)]. The grey line indicates the fibre length used in experiments.

The asymmetric case

Secondly, the signal to pump ratio was set to -10.4 dB and the idler to pump ratio was varied from -10.4 dB to -30.4 dB. This corresponds to a power imbalance between the signal and idler ranging from 0 dB to 20 dB. The positions of the first and second pump minima versus the power imbalance are then displayed in Fig. 5.4(c) with crosses for experiments, dashed lines for numerical simulations and solid ones for theoretical predictions. Here Z_1 ranges from about 2 to 3 km and Z_2 from 6 to 9 km. We observe that the larger the asymmetry, the further the pump minima, most of the variation occurring while the idler and signal power are close (i.e. small imbalance), eventually reaching an asymptotic value for large imbalances. The agreement between experiments and numerical simulations is good for both $Z_1$and Z_2.

Moreover, we point out that this power imbalance between the signal and idler also induces a time drift between successive maximum compression point [41]. It differs from the symmetric case with equal sidebands power, for which one can only obtain unshifted maximally compressed pulse trains or shifted of half a period, depending on the the initial relative phase $\Delta\Phi_{init}$, as studied previously (see Chapter 4). This temporal drift can be calculated via formulas provided by Santini and Grinevich [45]:

$$T_1 = \frac{arg(\alpha) - \Phi_\omega + \pi/2}{\omega} \times T_0 \tag{5.4}$$

$$T_{rec} = \frac{arg(\alpha\beta)}{\omega} \times T_0 \tag{5.5}$$

where $T_0 = \sqrt{|\beta_2|\, L_{NL}}$. The time-shift between the first and second maximum compression points is then given by $T_{rec} - T_1$. The drift is illustrated in Figs. 5.4(a,b) which show the spatio-temporal evolution of the field power (from numerical simulations) for a zero imbalance [Fig. 5.4(a)] and a 20 dB imbalance [Fig. 5.4(b)]. While there is no drift for the zero imbalance we notice a drift of about 5.5 ps for the 20 dB imbalance, in good agreement with the prediction from Eqs. (5.4) & (5.5), which give 5.2 ps. Note that we were not able to measure accurately these drifts experimentally. Indeed, it requires to reconstruct the spatio-temporal evolution using the method described in Chapter 4 and we have seen that the reconstruction

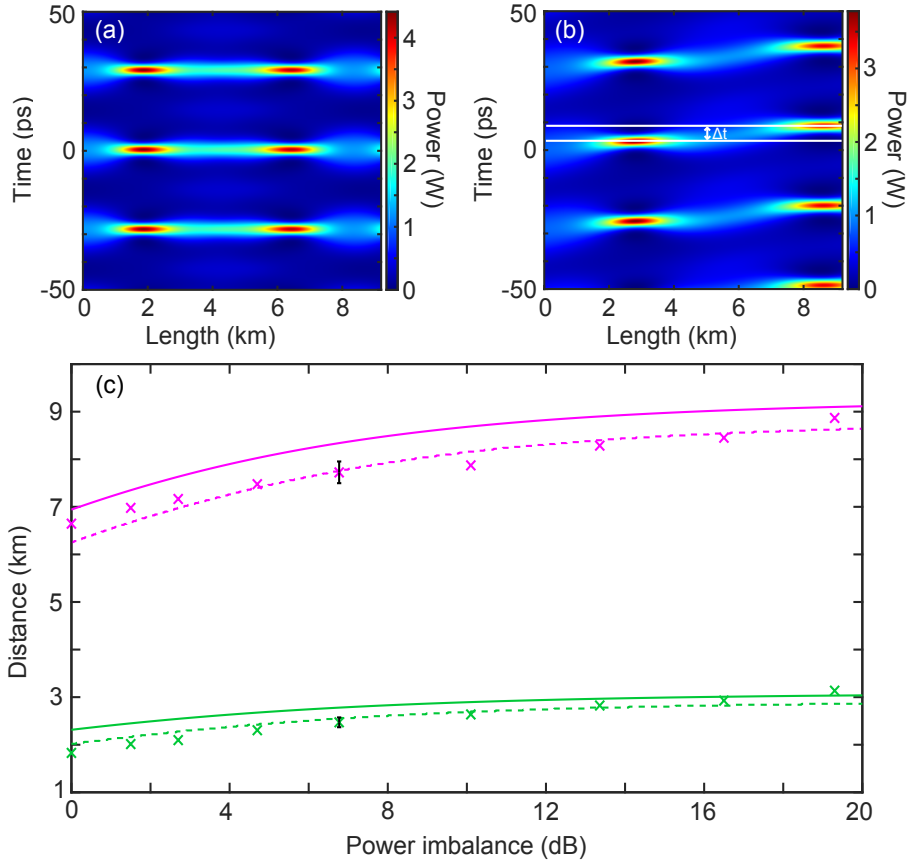

Figure 5.4: (a,b) Spatio-temporal evolution of the field power for a 0 dB and 20 dB imbalance, respectively. (c) Position of the first (green) and second (magenta) pump minima versus power imbalance between signal and idler. The crosses correspond to experimental recordings, dashed lines to numerical simulations from the NLSE and solid lines to theory [Eqs. (5.2) & (5.3)].

from only three waves does not give good results. One could suggest to add initially a supplemental set of sidebands as done previously to perform reconstruction from five waves. However this would be cumbersome to implement. Indeed, due to the initial spectrum asymmetry, we could not infer the evolution of the Stokes sidebands from the one of the anti-Stokes sidebands, doubling then the number of recordings to perform. Moreover, it would also strongly impact the dynamics when the power imbalance between the signal and idler is large. Indeed, the initial amplitude of this additional set of sidebands would be then of the same order of magnitude than the amplitude of the idler wave. Hence, the comparison with the predictions from

Grinevich and Santini would not be valid.

Summary

- We reported the experimental quantitative characterisation of the impact of the initial relative phase of the modulation sidebands on the first two recurrence cycles, in particular on the position of the first and second maximum compression points, and outlined the change of dynamics due to separatrix crossing.
- We also investigated the role of the modulation sidebands intensity, for equal and asymmetric sidebands.
- We compared our results to analytical estimates from a recent model by Grinevich and Santini [45], and found a good agreement despite the relatively strong input modulation intensity used in our experiments.

Chapter 6

Breathers collisions

Contents

In the previous chapters, we focused exclusively on first-order breathers and standard MI (i.e. $1 < \omega < 2$). However, as mentioned in Chapter 2, the nonlinear combination of first-order breathers can lead to higher-order breathers, which can present very high-amplitude peak at maximum compression point if the peaks of the first-order breathers coincide in time and space [41]. These solutions do not reduce to only three-waves asymptotically. In the first section we begin by describing the formalism of such solutions. In the second section we detail how one can generate these solutions experimentally. Finally we report the experimental characterisation of such solutions, with comparison to numerical simulations, via the distributed measurements in phase and intensity of their main frequency component and the calculation of the spatio-temporal evolution via the method described in Chapter 4.

6.1 Second-order breather formalism

Second-order breathers solutions (also called two breathers solution) describe the propagation of two elementary first-order breathers which can interact [123]. Taken independently, both of these breathers can be described by one governing parameter $a_{1,2} = \frac{1}{2}(1 - \omega_{1,2}^2/4)$ as explained in Chapter 2 when we described the AB. The formula for the field envelope of a second-order breather is reported in Ref. [93] and reads:

$$\Psi(\xi, \tau) = exp(i\xi)\left[1 + \frac{G + iH}{D}\right] \tag{6.1}$$

where

$$\begin{aligned} G = &-(\omega_1^2 - \omega_2^2)\left[\frac{\omega_1^2 b_2}{\omega_2} cosh(b_1\xi_{c1})cos(\omega_2\tau_{c2}) - \frac{\omega_2^2 b_1}{\omega_1} cosh(b_2\xi_{c2})cos(\omega_1\tau_{c1})\right. \\ &\left. - (\omega_1^2 - \omega_2^2)cosh(b_1\xi_{c1})cosh(b_2\xi_{c2})\right] \end{aligned}$$

$$\begin{aligned} H = &-2(\omega_1^2 - \omega_2^2)\left[\frac{b_1 b_2}{\omega_2} sinh(b_1\xi_{c1})cos(\omega_2\tau_{c2}) - \frac{b_2 b_1}{\omega_1} cosh(b_2\xi_{c2})cos(\omega_1\tau_{c1})\right. \\ &\left. - b_1 sinh(b_1\xi_{c1})cosh(b_2\xi_{c2}) + b_2 sinh(b_2\xi_{c2})cosh(b_1\xi_{c1})\right] \end{aligned}$$

$$\begin{aligned} D = &2(\omega_1^2 + \omega_2^2)\frac{b_1 b_2}{\omega_1\omega_2} cos(\omega_1\tau_{c1})cos(\omega_2\tau_{c2}) + 4b_1 b_2[sin(\omega_1\tau_{c1})sin(\omega_2\tau_{c2}) \\ &+ sinh(b_1\xi_{c1})sinh(b_2\xi_{c2})] - (2\omega_1^2 - \omega_1^2\omega_2^2 + 2\omega_2^2)cosh(b_1\xi_{c1})cosh(b_2\xi_{c2}) \\ &- 2(\omega_1^2 - \omega_2^2)\left[\frac{b_1}{\omega_1} cos(\omega_1\tau_{c1})cosh(b_2\xi_{c2}) - \frac{b_2}{\omega_2} cos(\omega_2\tau_{c2})cosh(b_1\xi_{c1})\right] \end{aligned}$$

where $b_{1,2} = \sqrt{8a_{1,2}(1 - 2a_{1,2})}$, Here $\tau_{c1} = \tau - \tau_1$ and $\xi_{c1} = \xi - \xi_1$ (same for the subscript 2) correspond to shifted normalised time and distance, (ξ_1, τ_1) being the space-time coordinate of the maximum compression point of the first-order breather.

To get a synchronous nonlinear superposition of the two breathers it is then necessary to have $(\xi_1, \tau_1) = (\xi_2, \tau_2)$. Thanks to our experimental setup we decided then to investigate how one can control the position of the highest-amplitude peak (or collision point) along a fibre by tuning the parameters ξ_1, ξ_2.[1]

6.2 Design of the input conditions

In order to design the experimental initial conditions to study second-order breather propagation we started from the previous analytical solution [Eq. (6.1)]. The sideband frequencies $\omega_{1,2}$ could not be chosen randomly. In fact, we remind that our inputs are obtained by tailoring a comb with equally spaced sidebands. Thus, it requires that ω_2 is a multiple of ω_1. In our case we chose ω_1 and ω_2 so that sidebands at these frequencies experience the same linear MI gain ($b_1 = b_2$). One can easily calculate that this corresponds to $\omega_1 = 2/\sqrt{5}$ and $\omega_2 = 4/\sqrt{5}$. For a total power of $P_0 = 500\,mW$, $\beta_2 = -19 \times 10^{-27} s^2/m$ and $\gamma = 1.3 \times 10^{-3}/W/m$ this corresponds to $f_1 = 26.6\,GHz$ and $f_2 = 53.2\,GHz$. Then we chose $\xi_1 = \xi_2 = -2.87$ (and $\tau_1 = \tau_2 = 0$). The nonlinear length L_{NL} being $1.54\,km$ this gives in physical units $z_1 = z_2 = -4.41\,km$. The position of the collision can then be expected to be $z = 4.41\,km$ which is in the range of our $7.7\,km$ fibre. The Fourier transform of $\Psi(\xi = 0, \tau)$ is then calculated in order to get the input spectrum. This spectrum is displayed in red in Fig. 6.1. As we can see, it is composed of many sidebands but only four falls within the MI gain band (the MI gain curve is superimposed in blue): the signal and idler at frequencies $\pm f_1$ and their first harmonics at $\pm f_2 = \pm 2 f_1$. Because these four sidebands and the pump are the most important components for the dynamic, we wanted to know if the dynamic of the propagation would be the same by launching a truncated five-wave input in the fibre (which is easier to do experimentally) or the full spectrum. This was checked by numerically integrating the NLSE for the truncated input and comparing the results to the calculation from Eq. (6.1). The comparison can be observed in Fig. 6.2(a,c) where we display the pump, signal and first harmonic (in blue, red and green respectively) power and phase evolutions obtained by numerically integrating the NLSE with the five-wave input and the dashed lines which correspond to the analytical solution. As we can

[1] Note that the first-order breather framework can still be valid for cases where there are more than two unstable modes (i.e. $0 < \omega < 1$). This corresponds corresponds to $a > 0.375$.

see, the agreement is almost perfect. This means that the higher-order solution modeled in Fig. 6.2 is very robust and while the initial conditions are slightly different from the theoretical model, a sharp and powerful second-order breather [see Fig. 6.2(e)] can be generated experimentally using a five-wave input.

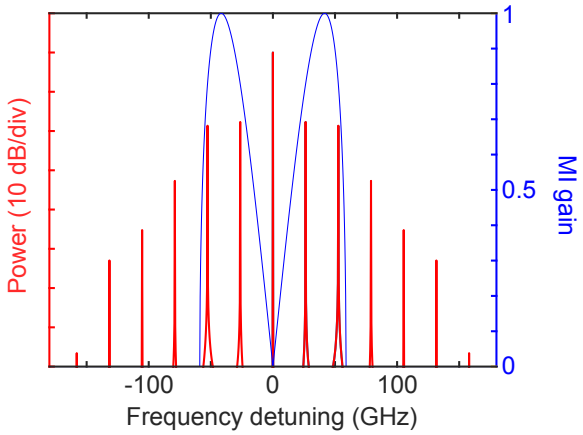

Figure 6.1: Spectrum at $\xi = 0$ from the Fourier transform of Eq. 6.1 for $\xi_1 = \xi_2 = -2.87$ and $P_p = 500\,mW$, $\beta_2 = -19 \times 10^{-27} s^2/m$, $\gamma = 1.3 \times 10^{-3}/W/m$, $\omega_1 = 2/\sqrt{5}$ and $\omega_2 = 4/\sqrt{5}$. The linear MI gain, normalised to its maximum, is superimposed in blue.

6.3 Experimental results

6.3.1 $\xi_1 = \xi_2 = -2.87$

We experimentally generated the truncated initial spectrum (5 waves) from Eq. 6.1 by using the Waveshaper to adjust the amplitude and phase of the waves. The parameters of the input spectrum are then the following: $P_p = 470\,mW$, signal/idler to pump ratio of $-17.7\,dB$, harmonics to pump ratio of $-18.7\,dB$, $\varphi_p = -0.68\,rad$, $\varphi_s = 0.26\,rad$, $\varphi_h = 2.82\,rad$ (note that the spectrum is symmetric compared to the pump so we state only the parameters of the signal and its harmonics and not the idler and its harmonics). The results are displayed in Fig. 6.2. Figs.6.2(a,c) show the power and phase evolutions of the pump (in blue), signal (in red) and first harmonic (green), respectively, from numerical simulations (NLSE with initial truncated spectrum). We observe an important pump power depletion of almost 20 dB around $z = 4.4\,km$, distance for which the first harmonic power is maximum and the signal power has also a local minimum. This is the position where the maximum compression point appears in the time domain as we can see in Fig. 6.2(e). Between 0 and about 4 km we observe two "arms" which collide at $z = 4.4\,km$ and give rise to a high-amplitude pulse with a peak power of $6.5\,W$ and then two "arms" again. Note that the position of the maximum compression point is exactly equal here to $|\xi_1| = |\xi_2|$ which is the point where the two initial breathers are supposed to nonlinearly superpose synchronously. As highlighted in Fig. 6.2(e), the period between two maximum compression points is equal to $1/f_1$. Experimental recording are displayed in Fig. 6.2(b,d,f,h). Parameters were the same than for the simulations except for a slightly different signal and harmonic frequencies: $f_1 = 26.3\,GHz$ and $f_2 = 52.6\,GHz$ (to be compared with $26.6\,GHz$ and $53.2\,GHz$). [2] As we can see, despite this slight change of initial conditions, the power and phase evolutions [Figs. 6.2(b,d)] are in good agreement with numerical simulations except around the end of the fibre, where the pump power decreases in experiment while it keeps increasing in numerical simulations. Moreover, we notice that in experiments the pump minimum appears around $z = 3.7\,km$ instead of $z = 4.4\,km$ in simulations.

[2] This frequency difference is due to technical limitations. Indeed, for certain frequencies of RF signal delivered to the PM by the association of the synthesizer and frequency doubler (see Fig.3.1), the optical spectrum at the output of the PM was not symmetric even though it is supposed to be. A slight change of frequency can fix the issue.

The reason for this disagreement is not exactly known. In fact, it was checked numerically that the structures generated should be robust to small perturbations of the initial conditions, whether on the pump and sideband powers or phases. The calculated (via the inverse Fourier transform from the five waves) spatio-temporal evolution of the field intensity and phase [Fig. 6.2(f,h)] also shows a relatively good agreement with simulations. We notice that the maximum compression points in Fig. 6.2(f) are almost split into two parts longitudinally. It was checked numerically that this is an effect of the truncation, such as explained in Chapter 4. Ideally, one would need to perform the inverse Fourier transform from at least seven waves in this case to avoid this kind of discrepancy but this requires improvements which would greatly enhance the complexity of the experimental setup.

6.3.2 $\xi_1 = -3.87$ & $\xi_2 = -2.87$

We then reproduced similar experiments and numerical simulations for a different set of (ξ_1, ξ_2): $\xi_1 = -3.87$ and $\xi_2 = -2.87$. Similarly to Fig. 6.1, we deduce from the calculated analytical spectrum at $\xi = 0$ (see Fig. 6.3) the input truncated spectrum that we are going to use in numerical simulations and experiments: $P_p = 420\,mW$, signal/idler to pump ratio of $-10.4\,dB$, harmonics to pump ratio of $-22.6\,dB$, $\varphi_p = -0.66\,rad$, $\varphi_s = 0.33\,rad$, $\varphi_h = 2.07\,rad$. As in the previous case $f_1 = 26.3\,GHz$ and $f_2 = 52.6\,GHz$ in experiments ($26.6\,GHz$ and $53.2\,GHz$ in numerical simulations).

The results are displayed in Fig. 6.4. In this case, we observe in simulations [Fig. 6.4(a)] a pump minimum at $z = 2.2\,km$ and a maximum of the signal and the harmonic around this point. Moreover, a small dip of the pump, associated to a local maximum of the harmonic can also be noticed close to $z = 5.8\,km$. In the time domain [Fig. 6.4(e)] we observe a maximum compression point around $z = 2.2\,km$ followed by two "arms" with a local maxima around $z = 5.8km$. Note that because ξ_2 has not been changed but ξ_1 is smaller than in the previous case (-3.87 compared to -2.87), it was expected that the maximum compression point would appear sooner in the propagation, as observed here ($2.2\,km$ compared to $4.4\,km$). Moreover, one can notice that the highest peak power achieved is this case is $5.5\,W$, smaller than the $6.5\,W$ observed in the previous case. This is because ξ_1 differs from ξ_2 so the two breathers do not fully superpose synchronously. Concerning the experimental results, they are displayed in Fig. 6.4(b,d,f,h). We get a relatively good agreement

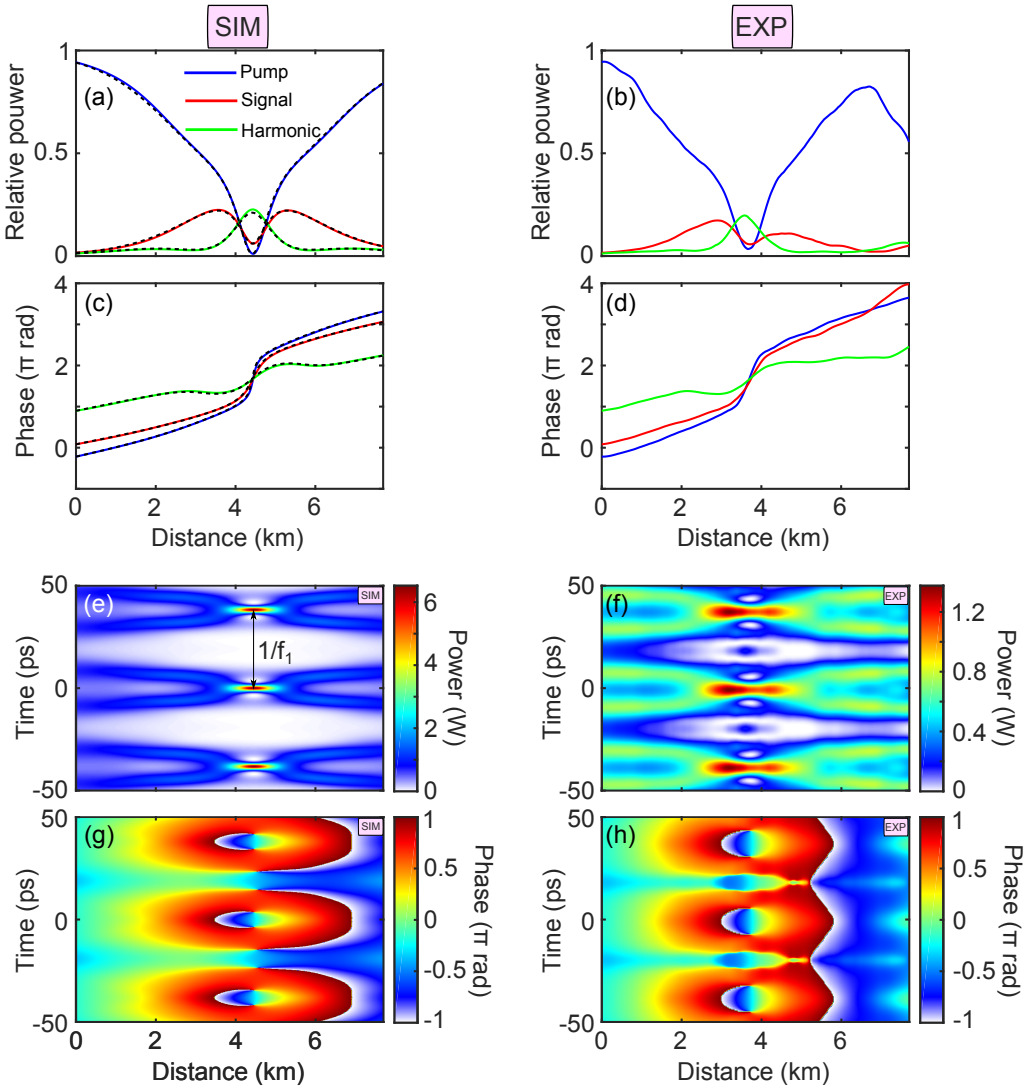

Figure 6.2: Relative pump, signal and harmonic power and phase evolutions, respectively, from (a,c) numerical simulations with a five-wave input and (b,d) from experiments. . Blue lines correspond to the pump, red ones to the signal and green ones to the harmonic. Dashed black lines in (a,c) correspond to the analytical solution from Eq. 6.1. Spatio-temporal evolution of the field power and phase (e,g) from numerical simulations and (f,h) from experiments. The spatio-temporal plot of (f,h) are obtained through the inverse Fourier transform of fives waves. Parameters: $P_p = 470\,mW$, signal/idler to pump ratio of $-17.7\,dB$, harmonics to pump ratio of $-18.7\,dB$, $\varphi_p = -0.68\,rad$, $\varphi_s = 0.26\,rad$, $\varphi_h = 2.82\,rad$, $f_1 = 26.6\,GHz$ and $f_2 = 53.2\,GHz$ ($f_1 = 26.3\,GHz$ and $f_2 = 52.6\,GHz$ in experiments)

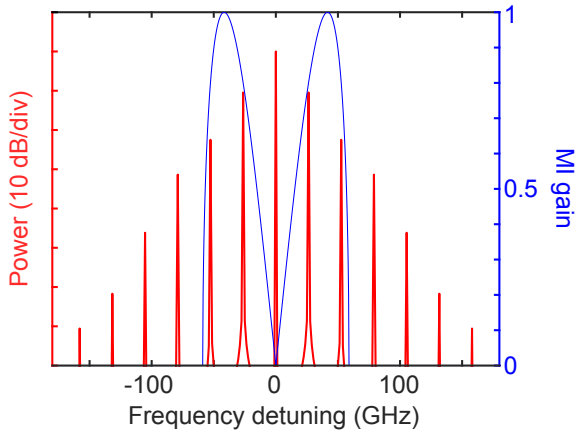

Figure 6.3: Same than Fig. 6.1 but with $\xi_1 = -3.87$ and $\xi_2 = -2.87$.

with numerical simulations despite some discrepancies at the end of the fibre and local maxima/minima which appear a bit sooner in experiments. In particular the pump minima is observed here at $z = 1.9\,km$. This position corresponds to the position of a longitudinally split pulse in the time domain [Fig. 6.4(g)]. While we observe a separation in two arms as expected, those latter have an higher amplitude than expected around $z = 5\,km$. This can be attributed mainly to the harmonic power and phase recordings. Indeed, we noticed that the small pulse used for the calibration of the harmonics experiences an unusual drop around this point (not shown here). Because we perform a ratio to correct the fading effect, this artificially amplifies the harmonic power at this point and also impacts the phase. Note that the experiment was repeated a few times and the drop was observed in every cases.

6.3.3 $\xi_1 = -1.87$ & $\xi_2 = -2.87$

Finally we set $\xi_1 = -1.87$ and $\xi_2 = -2.87$ and calculated the analytical spectrum at $\xi = 0$ (see Fig. 6.5) which gives us the five-wave input with the following parameters: $P_p = 480\,mW$, signal/idler to pump ratio of $-24.7\,dB$, harmonics to pump ratio of $-17.7\,dB$, $\varphi_p = -0.69\,rad$, $\varphi_s = 0.25\,rad$, $\varphi_h = 2.89\,rad$. As in the previous cases $f_1 = 26.3\,GHz$ and $f_2 = 52.6\,GHz$ in experiments ($26.6\,GHz$ and $53.2\,GHz$ in numerical simulations).

The results are displayed in Fig. 6.6. Numerical simulations show a pump minimum around $z = 6.7\,km$ [Fig. 6.6(a)]. In the time domain, one can notice two

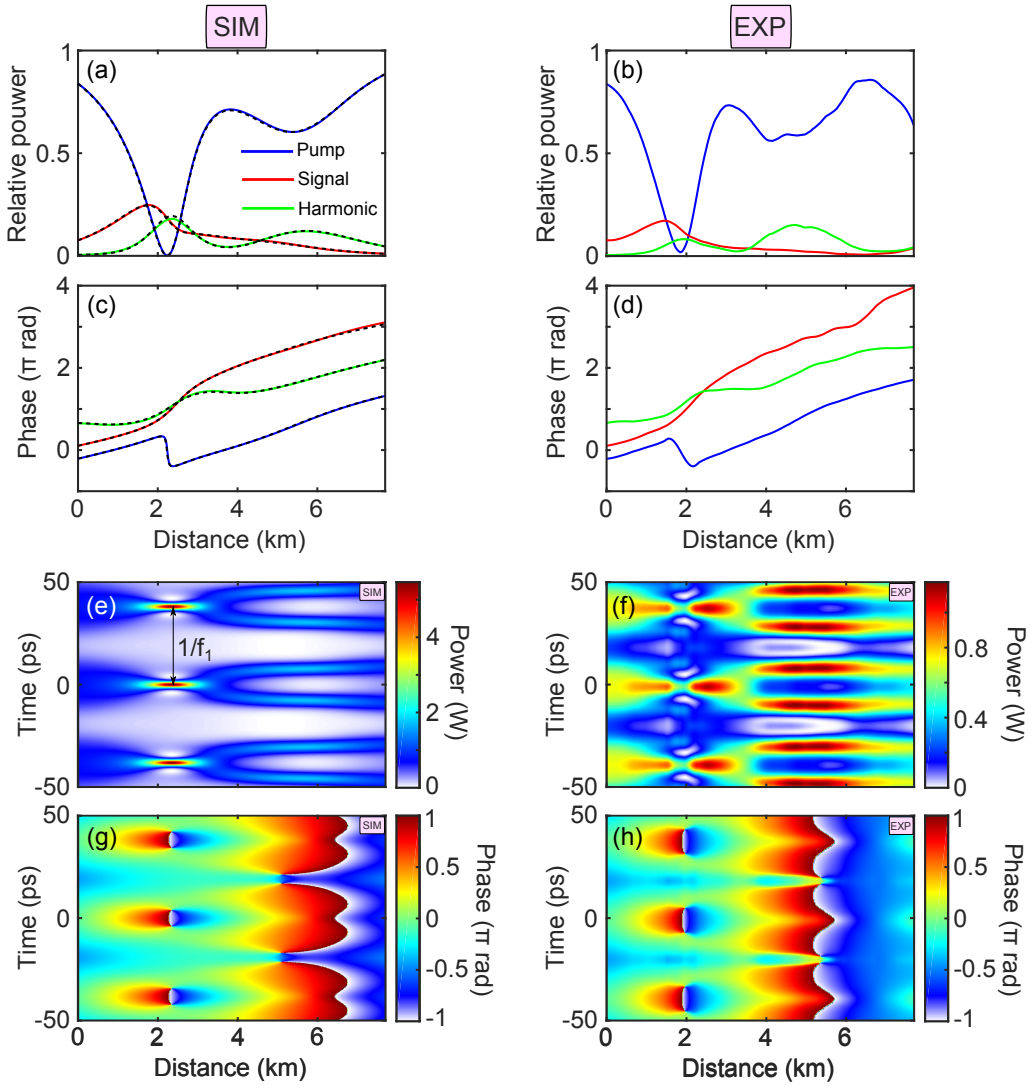

Figure 6.4: Same than Fig. 6.2 but with the following parameters: $P_p = 420\,mW$, signal/idler to pump ratio of $-10.4\,dB$, harmonics to pump ratio of $-22.6\,dB$, $\varphi_p = -0.66\ rad$, $\varphi_s = 0.33\ rad$, $\varphi_h = 2.07\ rad$, $f_1 = 26.6\ GHz$ and $f_2 = 53.2\ GHz$ ($f_1 = 26.3\,GHz$ and $f_2 = 52.6\,GHz$ in experiments).

"arms" colliding around this point [Fig. 6.6(e)] and the highest peak power is 5.3 W. Once again, it was expected that the maximum compression point would appear later in the propagation than for the two previous cases because ξ_2 is unchanged but ξ_1 is larger. The experimental results are in a relatively good agreements with these simulations. As previously, the trend of the power evolutions of the pump, signal and harmonics [Fig. 6.6(b)] is similar to the simulations, even if the local

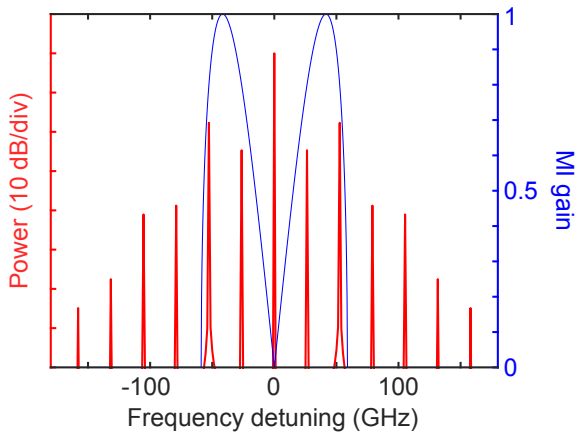

Figure 6.5: Same than Fig. 6.1 but with $\xi_1 = -1.87$ and $\xi_2 = -2.87$.

maxima/minima appear sooner (the minimum of the pump power is located around $z = 5.5\,km$). In the time domain [Fig. 6.6(f)] we also observe two "arms" with a maximum compression point around $z = 4.8\,km$. One can distinguish that the maximum compression point is in fact still split (the position of the split corresponds to the position of the pump minima) in two parts longitudinally but the "left part" is a far bigger amplitude than the "right part", which we attribute to the reconstruction.

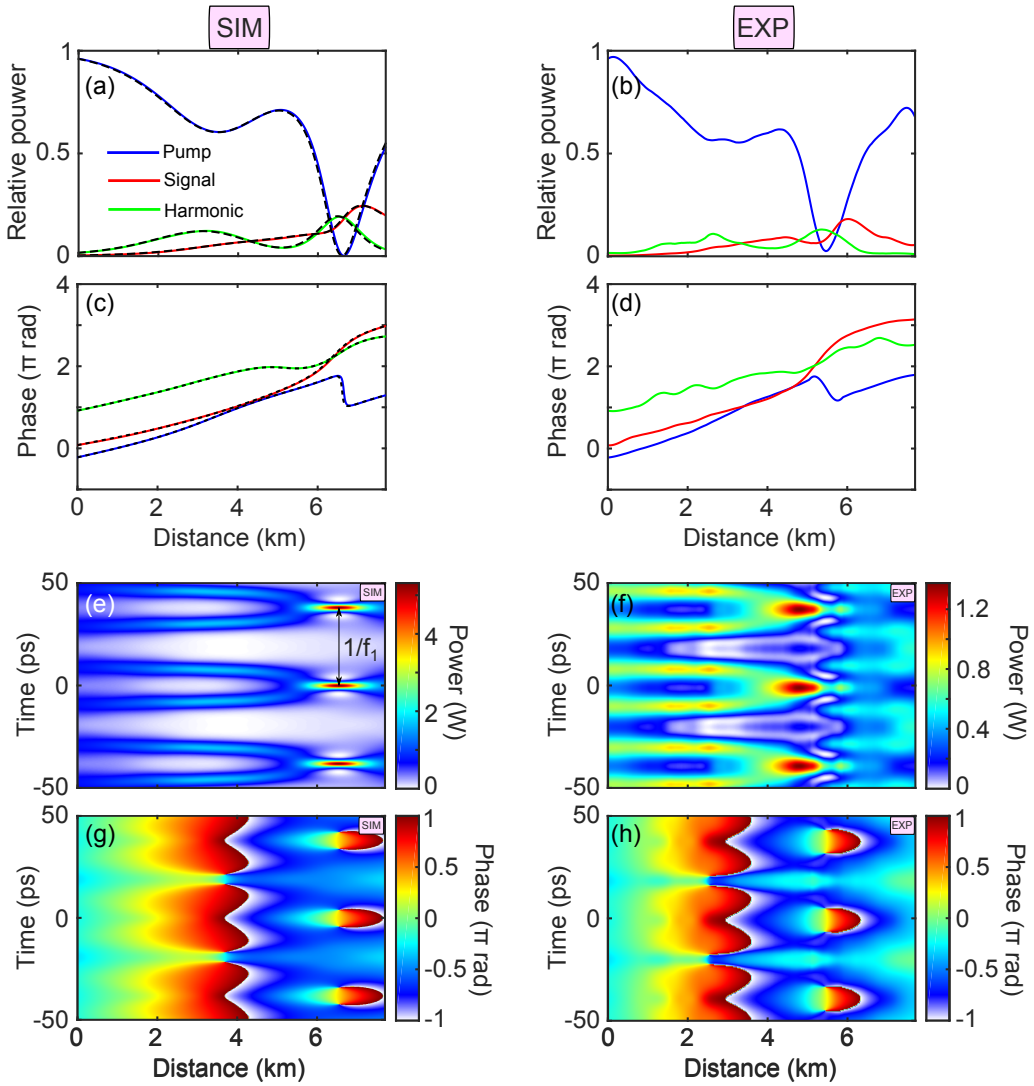

Figure 6.6: Same than Fig. 6.2 but with the following parameters: $P_p = 480\,mW$, signal to pump ratio of $-24.7\,dB$, harmonics to pump ratio of $-17.7\,dB$, $\varphi_p = -0.69\,rad$, $\varphi_s = 0.25\,rad$, $\varphi_h = 2.89\,rad$, $f_1 = 26.6\,GHz$ and $f_2 = 53.2\,GHz$ ($f_1 = 26.3\,GHz$ and $f_2 = 52.6\,GHz$ in experiments).

Summary

- We reported the experimental characterisation of second-order breathers via the intensity and phase measurements of their five main frequency components.
- The calculation of the spatio-temporal evolution of the field from the inverse Fourier transform of the five waves is in good qualitative agreement with numerical simulations, despite the truncation.

Conclusion

In this thesis, we investigated nonlinear phenomena related to the nonlinear stage of modulation instability in optical fibres, namely the Fermi-Pasta-Ulam-Tsingou recurrence process and breather dynamics. In particular, we focused on their experimental distributed characterisation along an optical fibre. In fact, we developed an experimental setup enabling the non-invasive distributed characterisation in intensity and phase of the main discrete frequency components of a pulse with a 20 m longitudinal resolution. This setup consists in an heterodyne optical-time domain reflectometer. It is associated to an active scheme based on Raman amplification in order to compensate for the fibre losses. Moreover, we detailed a simple post-processing method to retrieve the temporal evolution at the picosecond scale from the measurements performed in the frequency domain. The main results obtained thanks to this setup are summarised thereafter:

- Using carefully designed three-wave inputs (pump, signal and idler) with a precise control of intensity and phase, we were able to observe and characterise two Fermi-Pasta-Ulam-Tsingou recurrences cycles in the frequency and time domain. In particular, we outlined in the spectral domain two-types of qualitatively different phase-plane trajectories (inner and outer orbits) depending on the initial relative phase between the signal/idler and pump waves [42]. This is a signature of the symmetry-breaking of the recurrent process. In the time domain, we observed that this symmetry-breaking is characterised by unshifted or π-shifted maximally compressed pulse trains [43]. Following these observations, the impact of the initial modulation sidebands phase and intensity on the recurrent process was characterised quantitatively [44]. In particular, we focused on the positions of first two pump power minima/maximally compressed pule trains. Our results were found to be in a good agreement

with numerical simulations from the NLSE as well as with recent analytical estimates from Grinevich and Santini [45].

- Using a carefully designed five-wave input based on the analytical formulas describing second-order breathers, we showed that it was possible to generate similar structures experimentally. In particular, we emphasised that second-order breathers correspond to two first-order breathers nonlinearly interacting and that it was possible to control the strength of this interaction via the initial five-waves amplitude and phase. Three different cases were characterised in the frequency and time domain and found in relatively good agreement with numerical simulations and analytical predictions.

The work presented in this thesis paves the way for many future developments and investigations

- An upgrade of the Raman compensation scheme would enable the use of longer fibres, the length of about 8 km mostly used in this thesis being the optimal trade-off to obtain a good compensation of the losses with the current scheme. This would be useful as it would allow the observation of more recurrences and the investigation of such phenomena such as the noise-induced thermalisation of the recurrence process as discussed in Chapter 2 and in Ref. [97]. Investigations on the possible improvement for the loss compensation scheme have already begun with the recent internship of Guillaume Vanderhaegen (who will start its PhD in September 2019 and will pursue the work presented in this thesis). Using complex numerical simulations taking into account the depletion of the Raman pump [124, 125], the potential of a bi-directional pumping scheme rather than a contra-propagative one was highlighted for the observation of recurrences in a 20 km long SMF-28 fibre with a typical three-wave input used in experiments: $P_p = 450\,mW$, $\beta_2 = -19 \times 10^{-27} s^2/m$, $\gamma = 1.3 \times 10^{-3}/W/m$, initial signal/idler to pump ratio of -8.5 dB, $\omega = 1.25$ (sideband detuning from the pump of 35 GHz) and $\Delta\Phi_{init} = \pi/2$. This is illustrated by the power plots (pump in blue, signal in red) displayed in Figs. 6.7(a,b). For the same total Raman pump power (700 mW), two cases were considered, a contra-propagative one [Fig. 6.7(a)] where the Raman pump is launched at the output of the fibre and a bi-directional one [Fig. 6.7(b)] where 50% of the

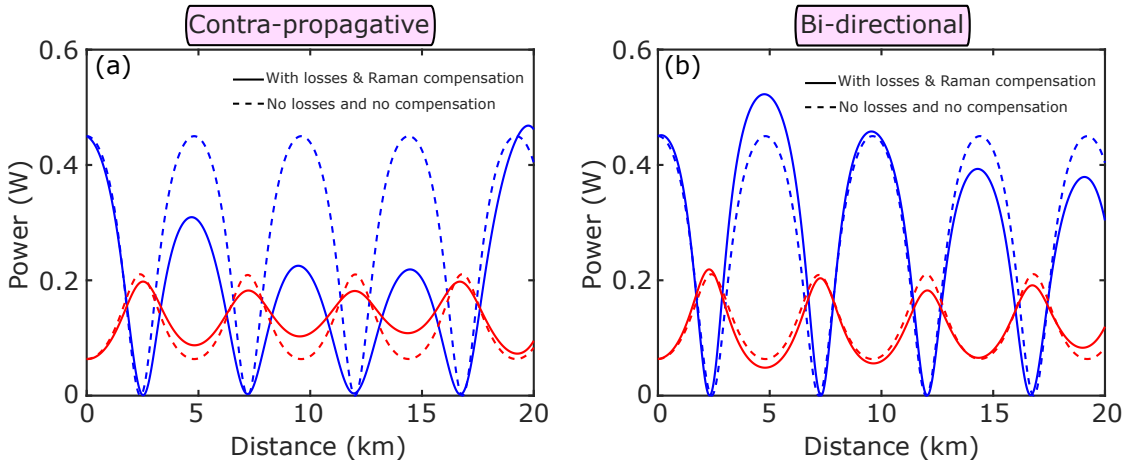

Figure 6.7: Evolution of the pump (blue) and signal (red) powers from numerical simulation taking into accounts the linear attenuation and the Raman compensation (solid lines) and in the ideal case without losses (dashed lines). A contra-propagative Raman scheme was considered in (a) and a bi-directional one in (b).

Raman pump is launched at the input of the fibre and the other 50% at this output. As we can see, up to five quasi-recurrences can be observed in both cases but the agreement between the bi-directional and the ideal case is far better than for the contra-propagative one.

- Another possible upgrade concerns the way the strong and weak pulse input spectra are tailored by the Waveshaper. With the current setup both spectra are identical except for a 13 dB attenuation on all components for the weak one because the Waveshaper cannot switch rapidly enough between two different designed filters. As we consider mostly triangular spectra, this means that we are limited currently to five waves (pump, signal/idler, first-order harmonics) because the higher-order harmonics of the weak pulse are too weak to be detected. Yet, our post-processing calibration technique does not require the weak pulse spectrum to have also a triangular shape. All its components have just to be weak enough in order to assume that the weak pulse only experiences linear effects. Hence, a solution could be to use two separates Waveshaper to tailor the input spectra of the strong and weak pulse as illustrated by the sketch in Fig. 6.8. Thanks to an optical switch one pulse over two could be sent to Waveshaper 1 to get the desired three-wave input (or else) and the

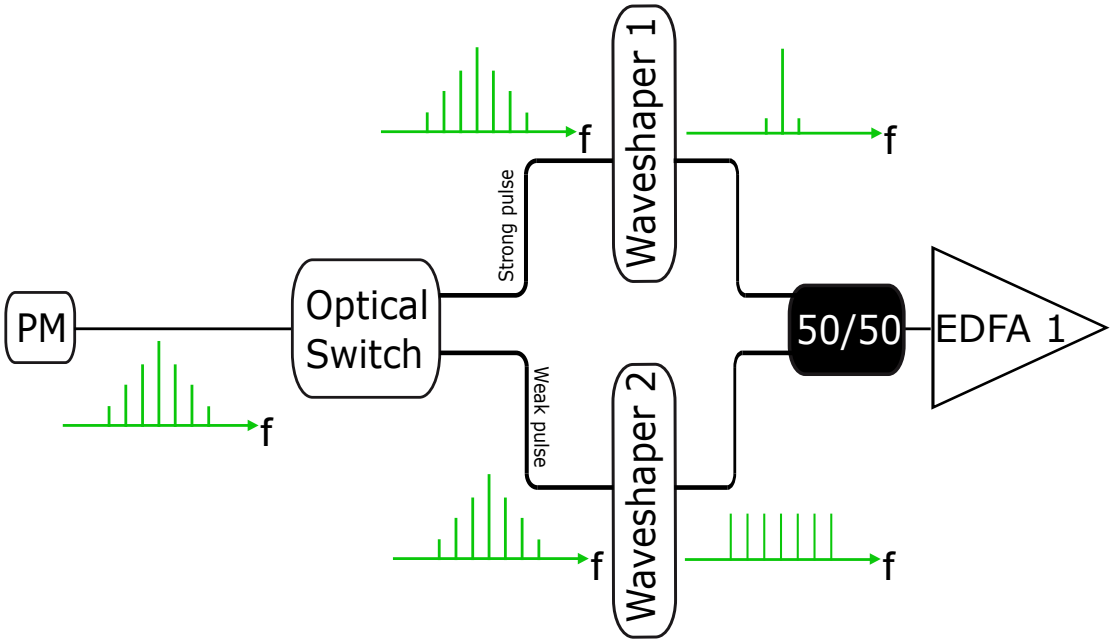

Figure 6.8: Sketch of a possible input spectrum tailoring scheme

following pulse would be sent to Waveshaper 2 to get a comb of equal sidebands (and more importantly to attenuate the more powerful spectral components). Then the two different paths would be recombined, the rest of the setup being unchanged. Ideally this upgrade would induce a 13 dB improvement of the SNR. That would potentially allow to detect seven waves or even nine and then improve greatly the temporal evolutions retrieved via inverse Fourier transform, which would be very useful for the study of higher-order breathers in particular.

- An interesting topic would be the experimental study of FPUT recurrences in the normal dispersion regime. Indeed, as mentioned in Chapter 2, MI can potentially arise in this regime if a degree of freedom is added to fulfill the phase-matching relation and if is seeded, FPUT recurrences can be triggered. For instance, MI have been observed and recurrences have been predicted in dispersion oscillating fibres (DOFs) with a sinusoidal dispersion profile [126, 127]. MI has also been experimentally demonstrated in the weak normal dispersion regime of dispersion-shifted fibres thanks to the influence of the fourth-order

dispersion [71] and preliminary simulations show the appearance of FPUT recurrences in such system if the process is seeded. In experiment, the main challenge to observe recurrences in the two previous cases consists in the generation of a suitable local oscillator. Indeed, the frequency detuning required (compared to the pump frequency) are typically in the THz range, which is far too large for a generation via a simple modulator. Yet, to perform our measurements, we have to ensure a fixed phase relationship between the spectral components of the local oscillator. Thus, a solution could be the generation of a broad frequency comb via two steps. First, the generation of an electro-optic (EO) comb via a an intensity modulator followed by a cascade of phase modulators [128]. This EO comb would then be enlarged thanks to the propagation in a highly nonlinear fibre.

- We draw the attention of the reader on the the work described in Appendix B, which paves the way for the observation of Lorenz chaos in passive optical fibre-ring cavities [129, 130].

Appendix A : First-order solutions of the nonlinear Schrödinger equation

We report here the expressions of exact first-order solutions of the NLSE first derived by Akhmediev *et al*. in 1987 [24]. These solutions have been recently derived again by Matteo Conforti, with some modifications.

The real and imaginary part of first-order solutions being linearly related this implies the following form of the solution:

$$\Psi(\xi,\tau) = [Q(\xi,\tau) + i\delta(\xi)]\, e^{i\phi(\xi)} \tag{6.3}$$

Two classes of solution depending on three parameters appear. The first one (type A), describes the standard recurrences and is controlled by three real parameters. The second one (type B) describes shifted recurrences and depends on a real and two complex conjugate parameters.

Type A solution

The solution depends on three real parameters $\alpha_3 > \alpha_2 > \alpha_1 > 0$. The expression for the δ function is the following:

$$\delta(\xi) = \frac{\sqrt{\alpha_1\alpha_3}sn(\mu\xi)}{\sqrt{\alpha_3 - \alpha_1 cn^2(\mu\xi,k)}} \tag{6.4}$$

where the elliptic modulus is $m = k^2 = \frac{\alpha_1(\alpha_3-\alpha_2)}{\alpha_2(\alpha_3-\alpha_1)}$ and $\mu = 2\sqrt{\alpha_2(\alpha_3-\alpha_1)}$.

For the ϕ function we have the following expression:

$$\phi(\xi) = (\alpha_1 + \alpha_2 - \alpha_3)\xi + \frac{2\alpha_3}{\mu}\Pi(am(\mu\xi), n, k) \tag{6.5}$$

where $n = \frac{\alpha_1}{\alpha_1 - \alpha_3}$ and $\Pi(am(\mu\xi), n, k)$ is the incomplete elliptic integral of the third kind [131].

For the Q function we have the following expression:

$$Q(\xi, \tau) = \frac{Q_A(Q_B - Q_D) + Q_D(Q_A - Q_B)sn^2(p\tau, k_q)}{(Q_B - Q_D) + (Q_A - Q_B)sn^2(p\tau, k_q)} \tag{6.6}$$

where the elliptic modulus is $m_q = k_q^2 = \dfrac{\alpha_2 - \alpha_1}{\alpha_3 - \alpha_1}$ and $p = \sqrt{\alpha_3 - \alpha_1}$. The parameters $Q_A(\xi) > Q_B(\xi) > Q_C(\xi) > Q_D(\xi)$ have the following expressions:

$$Q_A = s\sqrt{\alpha_1 - x} + \sqrt{\alpha_2 - x} + \sqrt{\alpha_3 - x} \tag{6.7}$$

$$Q_B = -s\sqrt{\alpha_1 - x} - \sqrt{\alpha_2 - x} + \sqrt{\alpha_3 - x} \tag{6.8}$$

$$Q_C = -s\sqrt{\alpha_1 - x} - \sqrt{\alpha_2 - x} - \sqrt{\alpha_3 - x} \tag{6.9}$$

$$Q_D = s\sqrt{\alpha_1 - x} - \sqrt{\alpha_2 - x} - \sqrt{\alpha_3 - x} \tag{6.10}$$

with $x(\xi) = \delta^2(\xi)$ and $s(\xi) = sign(\frac{\partial\delta}{\partial\xi}) = sign(cn(\mu\xi, k))$. Note that the expressions (6.7)-(6.10) differ from the original one reported in [24] due to the presence of the sign function.

The period in ξ, let's say L and the period in τ, let's say Θ can be calculated as follows :

$$L = \frac{4K(k)}{\mu},\ \Theta = \frac{2K(k_q)}{p} \tag{6.11}$$

where K is the complete elliptic integral of the first kind.

Type B solution

The solution depends on three real parameters $\alpha_3 > 0, \rho, \kappa$ (which amounts to define $\alpha_1 = \alpha_2^* = \rho + i\kappa$). The expression for the δ function is the following:

$$\delta(\xi) = \sqrt{\frac{\alpha_3}{2}(1 - \upsilon)\frac{1 + dn(\mu\xi, k)}{1 + \nu cn(\mu\xi, k)}}sn(\mu\xi/2, k) \tag{6.12}$$

where

$$m = k^2 = \frac{1}{2}\left(1 - \frac{\kappa^2 + \rho(\rho - \alpha_3)}{AB}\right) \tag{6.13}$$

$$A = \sqrt{(\alpha_3 - \rho)^2 + \kappa^2} \tag{6.14}$$

$$B = \sqrt{\rho^2 + \kappa^2} \tag{6.15}$$

$$\nu = \frac{A - B}{A + B} \tag{6.16}$$

$$\mu = 4\sqrt{AB} \tag{6.17}$$

For the ϕ function we have the following expression:

$$\phi(\xi) = \left(2\rho + \frac{\alpha_3}{\nu}\right)\xi - \frac{\alpha_3}{\mu\nu}\left[\Pi(am(\mu\xi), n, k) - \nu\sigma tan^{-1}\left(\frac{sd(\mu\xi, k)}{\sigma}\right)\right] \tag{6.18}$$

where $n = \dfrac{\nu^2}{\nu^2 - 1}$, $\sigma = \sqrt{\dfrac{1 - \nu^2}{k^2 + (1 - k^2)\nu^2}}$ and $sd(\mu\xi, k) = \dfrac{sn(\mu\xi, k)}{dn(\mu\xi, k)}$.

Formula 6.18 is different from the one presented in [24].

For the Q function we have the following expression:

$$Q(\xi, \tau) = sb - c_+ \frac{r + cn(p\tau, k_q)}{1 + rcn(p\tau, k_q)} \tag{6.19}$$

where

$$
\begin{aligned}
s &= sign(cn(\mu\xi/2, k)) \\
b &= \sqrt{\alpha_3 - x} \\
r &= \frac{M-N}{M+N} \\
p &= \sqrt{MN} = 2\sqrt[4]{(\alpha_3-\rho)^2+\kappa^2} \\
M^2 &= (2sb + c_+)^2 + c_-^2 \\
N^2 &= (2sb - c_+)^2 + c_-^2 \\
c_\pm &= \sqrt{2\left[\sqrt{(x-\rho)^2+\kappa^2} \pm (\rho - x)\right]} \\
k_q^2 &= \frac{1}{2} + 2\frac{\rho-\alpha_3}{p^2}
\end{aligned}
$$

The period in ξ (L) and τ (Θ) can be calculated as follows:

$$L = \frac{8K(k)}{\mu}, \Theta = \frac{4K(k_q)}{p} \tag{6.20}$$

We test how both types of solution match with a three-wave input evolution by comparing them to numerical simulations of the NLSE with parameters similar to the one used in Chapter 4 : $P_p = 450\,mW$, $\beta_2 = -19 \times 10^{-27} s^2/m$, $\gamma = 1.3 \times 10^{-3}/W/m$, signal/idler to pump ratio of -8.5 dB, $f = 35\,GHz$ and $\Delta\Phi_{init} = 0$ (type A solution) or $\Delta\Phi_{init} = -\pi/2$ (type B solution). In order to find the analytical solution fitting the best with a three-wave input we use a Gauss-Newton algorithm which gives us the set of three parameters ($[\alpha_1\ \alpha_2\ \alpha_3]$or $[\rho\ \kappa\ \alpha_3]$) for which the three central waves of an analytical solution perfectly match with our three-wave input as displayed in Fig. A.1(d,i). In the case with $\Delta\Phi_{init} = -\pi/2$, we observe that the analytical input spectrum [Fig. A.1(i)] contains only 6 sidebands. Noteworthy, the even-th order sidebands have a zero amplitude. The harmonics sidebands are then more than 30 dB lower than the signal and idler, giving an analytical temporal input (dashed line) which matches almost perfectly with the cosine modulation (cyan line) [see Fig. A.1(h)]. This leads to an almost perfect match between the simulated and analytical evolution, as can be seen with the analytical and simulated spatio-temporal evolution in Fig. A.1(f,g) and the longitudinal pump and signal power evolution in Fig. A.1(j) (solid lines for simulation and dashed ones for theory). This

closeness between the three-wave input and the type B solution explains why the recurrence seems always "better" in simulation and experiments with a three-wave input with $\Delta\Phi_{init} = \pm\pi/2$ even when the initial modulation is relatively strong. For $\Delta\Phi_{init} \neq \pm\pi/2$ the even-th order sidebands are not zero anymore and the initial condition can differ strongly from the three-wave input. In fact, for $\Delta\Phi_{init} = 0$, we observe that the input analytical solution (black lines) consists in a triangular spectrum involving many sidebands (22 in a 80 dB range). Hence, the analytical temporal input (dashed line) strongly differs from the simulated cosine modulation (cyan line) in Fig. A.1(c) and the evolution of the three-wave input does not consist of perfect recurrences as we observe in Fig. A.1(a,e).

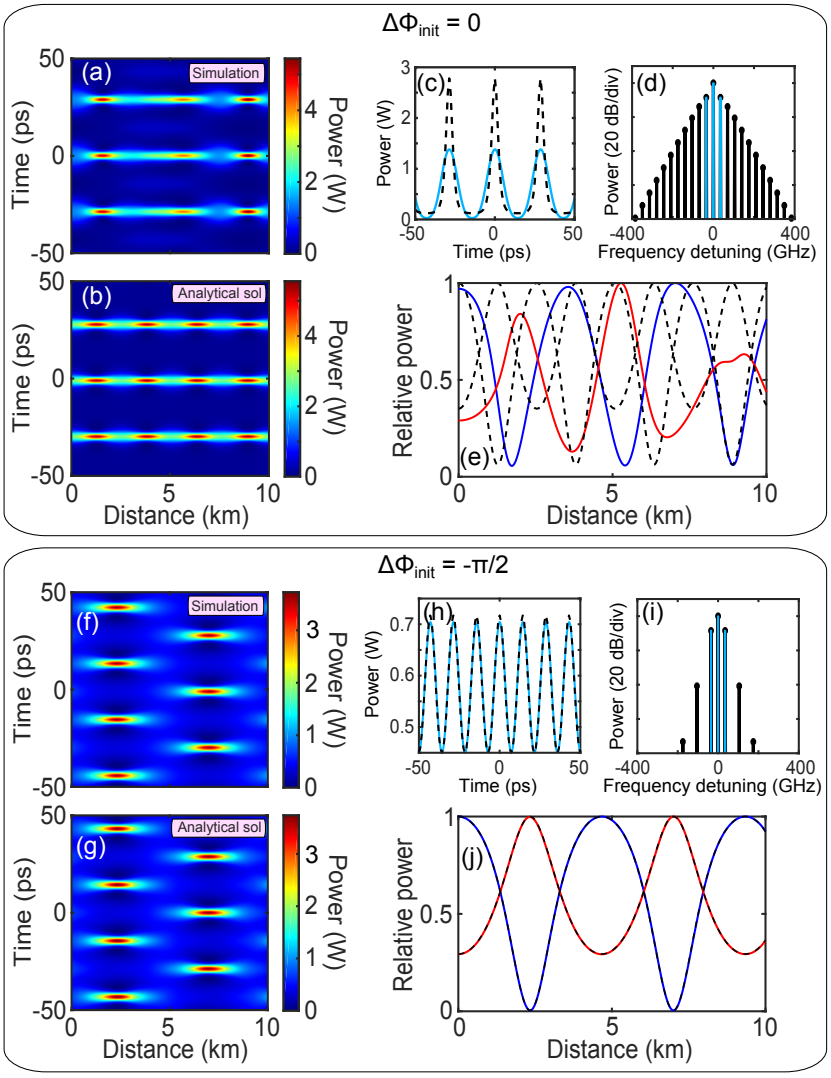

Figure A.1: (a,b) Spatio-temporal evolution from numerical simulation of the NLSE and from the type A solution, respectively. (c,d) Initial temporal and spectral profile, respectively, with cyan lines for simulations and black ones for analytical formula. (e) Evolution of the pump (blue line) and signal (red line) power along the fibre. The dashed black lines correspond to type A solution. Parameters : $P_p = 450\,mW$, $\beta_2 = -19 \times 10^{-27} s^2/m$, $\gamma = 1.3 \times 10^{-3}/W/m$, signal/idler to pump ratio of -8.5 dB, $f = 35\,GHz$ and $\Delta\Phi_{init} = 0$.(f-j) Same than previously except for $\Delta\Phi_{init} = -\pi/2$ and type B solution instead of type A.

Appendix B : Phase-dependence of seeded modulation instability in passive optical fibre-ring cavities

The work presented in this appendix results from a collaboration with another PhD student of the team, Florent Bessin, whose thesis focuses on passive optical fibre-ring cavities. Thus, Florent Bessin took care of the theoretical and numerical aspects of this work. Experiments were performed by both of us and data processing by myself. Then, only the experimental setup implemented and its operation are described here, with some results to highlight its performances. To know more about the dynamics of passive optical fibre-ring resonators, in particular about the theoretical and numerical aspects of the problem investigated here, we redirect then the reader to the thesis of Florent Bessin (in writing).

Passive optical cavities are system of great interest which can exhibit very rich nonlinear dynamics [132]. The boundary conditions can significantly impact the dynamics. For instance, the conditions to observe MI in such systems [133, 134] are not the same than in the single-pass configuration, as described previously in this thesis (see Chapter 2). Moreover, it can also exhibit completely new features such as bistability. The primary goal of this collaboration was to implement an experimental setup allowing the round-trip to round-trip full-field characterisation of the intra-cavity field in order to observe Lorenz chaos [129] in the bistable regime. In fact, using a three-wave truncation of the Lugiato-Lefever equation (which is a mean-field equation used to describe the dynamics in cavities, see Ref. [132] for more details), Haelterman and coworkers [130] showed that it was in theory possible to observe different attractor dynamics in a phase-plane configuration. In particular

they showed the existence of regimes with the evolution towards a single attractor (corresponding to a steady-state) or two attractors with the characteristic "butterfly" trajectory, in the phase-plane, of Lorenz chaos [129]. However, to characterise such phenomenon, one has to be able to measure the round-trip to round-trip evolution of the complex field, which is not easily accessible. Indeed the dynamics is often too rapid (the picosecond typically) and the repetition rate too high (the MHz) for direct photo-detection. Thus, most of the investigations rely on ultrafast techniques such as time lens [119] to study the temporal dynamics or dispersive Fourier transform for the spectral dynamics [118, 135, 136]. Taken apart, these techniques only give information on the amplitude and not on the phase. One has to combine both techniques and use reconstruction algorithm to retrieve the phase from the temporal and spectral intensity [99, 121] or add supplemental method such as spectral interferometry [137]. Another approach for phenomenon with discrete line spectra (i.e time-periodic signals), as previously studied in this thesis, is heterodyne detection in the frequency domain. Here, this is particularly suitable as the characterisation of the pump and signal waves would be enough to characterise the chaos in phase-planes [130]. Hence, this was the detection method chosen for our experiment.

Although our goal is ultimately to observe chaos, it presents other challenges than the detection, especially its generation. As a first step toward this objective, we then focused on another process related to MI dynamics in passive cavities which is phase-sensitive amplification. Using three-wave inputs (i.e a pump, signal and idler waves), we investigated how the initial relative phase $\Delta\Phi_{init}$ between these waves affects the MI process in the monostable regime. Indeed, theory and numerical simulations show that the dynamics is very rich, with a gain highly-dependent on the initial relative phase and in particular an absence of gain for discrete values of $\Delta\Phi_{init}$. Note that, in this appendix, the relative phase $\Delta\Phi$ is defined in the opposite way than previously. Here, it reads $\Delta\Phi = [\varphi_s + \varphi_i - 2\varphi_p + \beta_2\Omega^2 z]/2$, which gives for initial symmetric sidebands $\Delta\Phi_{init} = \varphi_s - \varphi_p$.

Experimental setup and data processing

The aim of this experimental setup [see Fig. B.1] is to perform round-trip to round-trip intensity and phase measurements of the intra-cavity pump and signal components. Because a heterodyne detection scheme is adequate to perform such measurements we used parts of the HOTDR setup described previously in this thesis (see Chapter 3). In particular, we used the same lasers as well as a similar detection channel. The phase-locking scheme has also been unchanged, apart for a different reference frequency which is here set at 1.7 GHz (compared to 800 MHz). This is because we use 10 ns pulses in this experiment, shorter than the 50 ns pulses previously used. The cavity used in this experiment is composed of a 170 m long standard telecommunication fibre with a GVD of $\beta_2 = -19 \times 10^{-27} s^2/m$ and a nonlinear coefficient $\gamma = 1.3 \times 10^{-3}/W/m$. It has a finesse of about 22.

Here we will focus first on the driving-field generation. Then we will detail how the the cavity is stabilised thanks to a control beam. Finally we will describe how the datas are processed.

Driving field generation

In order to generate a suitable three wave-input Laser 1 is phase modulated to create a comb which is then tailored by a Waveshaper. An intermediate intensity modulator (IM1), driven by a RF signal from a pulse generator, is used to create sequence of 10 ns pulses at a repetition rate of about 1.2 MHz, which corresponds to the free spectral range (FSR) of the 170 m long cavity. To observe the desired nonlinear effects, it is indeed necessary for the cavity to be synchronously pumped. Note that theses pulses are pre-amplified by SOA1 before the Waveshaper. 20% of the output of the Waveshaper is then amplified by an EDFA before passing through an acousto-optic modulator (AO1). The role of this AO, used as a temporal gate, is two-fold. First, it allows to remove the excess noise of the CW background between the pulses in order to mitigate SBS. Secondly, it periodically kills a certain number of consecutive pulses, thus allowing the generation of bursts. These bursts are essential to the experiment. Indeed, in the case of the dynamic we are going to investigate, a steady-state is usually reached after a hundred round-trip. In order to repeat the experiment, it is then necessary to empty the cavity, which can be done by not

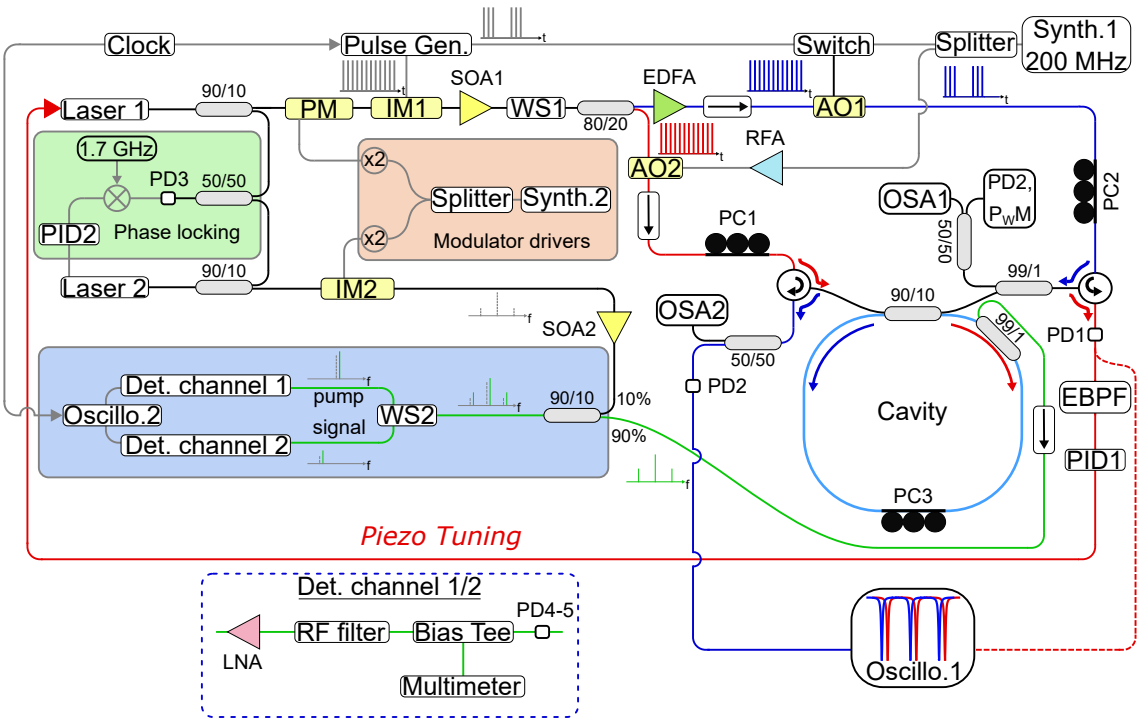

Figure B.1: The experimental setup. Laser 1 is a narrow linewidth (100 Hz at FWHM) CW laser and laser 2 is a continuous distributed feedback laser diode. IM: intensity modulator, PM: phase modulator, EDFA: erbium doped fibre amplifier, AO: acousto-optic modulator, SOA: semiconductor optical amplifier, PID: proportional, integral, derivative controller, PD: photo-detector, PC: polarisation controller; RF: radio frequency, LNA: low-noise radio frequency amplifier, EBPF: electronic band-pass filter, PwM: powermeter. *Courtesy of Florent Bessin*

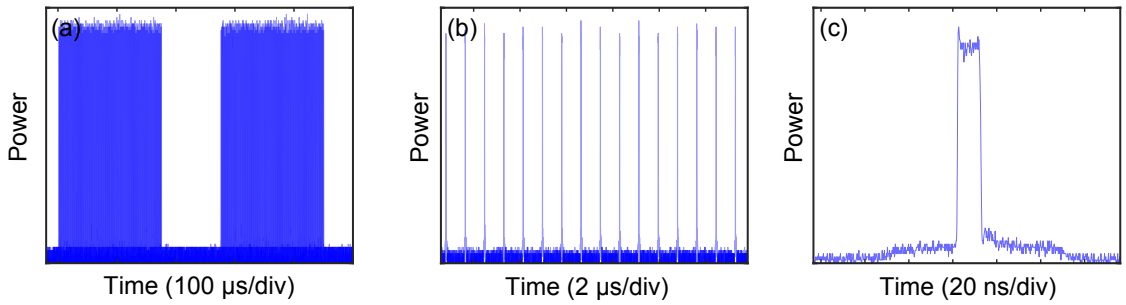

Figure B.2: (a) Recording of two consecutive bursts. (b) Zoom on a burst. (c) Temporal profile of an input pulse.

pumping the cavity for a certain amount of time. The bursts used in our experiment consisted then in sequence of 210 consecutive pulses, followed by 120 "dead pulses", which refer to the input pulses suppressed by AO1, as displayed in B.2(a) which shows two consecutive bursts. In the Fourier domain, the parameters of the three-wave input generated are the following: $P_p = 200\,mW$, signal/idler to pump ratio of -20.5 dB, frequency detuning $f = 54\,GHz$. Concerning $\Delta\Phi_{init}$, it will be varied in order to investigate its impact on the dynamics.

Stabilisation of the cavity

Due to the interferometric nature of driven optical cavities, it is necessary to be able to control the linear phase ϕ_0 accumulated by the wave every round-trips, which has a big impact on the dynamics [132]. In order to maintain this parameter fixed, it is necessary to isolate the cavity from external perturbations. Indeed, this linear phase can be expressed as $\phi_0 = 2\pi cnL/\lambda_P$ where c is the velocity of light, n the refractive index of the propagating medium, L the length of the cavity and λ_P the pump wavelength. Then, external sounds or thermal fluctuations can impact the length L and hence ϕ_0. However, although the isolation of cavity does help (it is placed in a specific box in our case) it is usually not sufficient enough and an active stabilisation scheme is required in order to finely tune either L or λ_P to adjust ϕ_0. In our case this is done by using a feedback loop, which works as follows. Before its amplification by the EDFA, a fraction of Laser 1 is deducted. This is the control beam. The control beam is then injected into the cavity but from the other input port compared to the previous driving field. Thus, it contra-propagates but experiences the same

linear phase accumulation. Note that due to the presence of AO1, the driving field experiences a 200 MHz frequency shift. Hence, to ensure that the control beam has the same frequency (or wavelength) than the driving field and experiences the same linear phase accumulation, we introduced another acousto-optic (AO2) on the path of the control beam before its entrance in the cavity. This acousto-optic is only used to induce a 200 MHz frequency shift and not to perform any modulation of the control beam. At the output of the cavity, the control beam is then detected by the photo-detector PD1 and serve as a reference for PID1. This PID controls then the integrated laser piezoelectric module of Laser 1, tuning the pump wavelength with a larger bandwidth (16 kHz) than external perturbation frequencies. In particular, this system allows to scan the pump wavelength in order to scan the resonances of the cavity and to fix a setpoint (For more details on the principles of this stabilisation scheme one can refer to Ref. [138]). Note that during this procedure, the sideband generation (via the phase-modulator) is shut-off.

The linear phase is usually expressed via the detuning parameter which reads as $\delta_0 = 2k\pi - \phi_0$ (k integer). In our case, the chosen setpoint gives a detuning of $\delta_0 = 0.05$, which is very small and ensures that we operate in the monostable regime.

Data processing

Once the detuning is fixed and the pump power adjusted ($P_p = 200\,mW$), one can notice MI sidelobes arising from noise on the optical spectrum of the output of the cavity (OSA1), as displayed in Fig. B.3. Here the maximum of these lobes are located at $f = \pm 54\,GHz$. The sidebands generation is then switched-on in order to generate sidebands at these frequencies. Previously in section 4.7, we said that we were limited to $f = 40\,GHz$ which is the maximum RF signal frequency that can be provided by the association of the synthesizer and the frequency doubler. Thus Laser 1 is modulated here at $27\,GHz$. Because the phase-modulation generates a triangular comb, this generates in particular sidebands at $\pm 2 \times 27 GHz = \pm 54 GHz$. These sidebands have a weak amplitude compared to those at $\pm 27\,GHz$ and the pump but this is not an issue as this experiment does not require an initial strong signal/idler. Apart from the pump and the sidebands at $f = \pm 54\,GHz$ all others sidebands are filtered out by the Waveshaper and the signal/idler to pump ratio

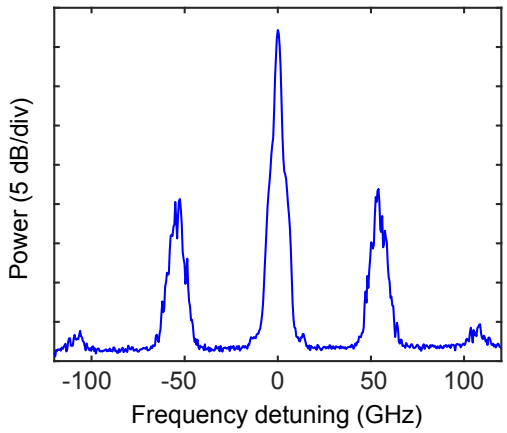

Figure B.3: Optical spectrum of MI arising from noise once the setpoint is fixed in experiments

is fixed at -20.5 dB. The data acquisition and processing can then start. Thanks to a 99/1 coupler placed into the cavity 1% of the intra-cavity field is extracted every round-trip and sent to the detection scheme where it is mixed with the local oscillator and detected. Because we operate with train of pulses, we detect then train of beatings on the oscilloscope. After the application of a 200 ns gaussian window (with a 20 ns FWHM) on each of these beatings, the power and phase at 1.5 GHz are evaluated with a FFT. Once again, the demodulation is performed at this frequency and not 1.7 GHz because one has to take into account the 200 MHz frequency shift induced on the driving field by AO1. Fig. B.4(a) displays a typical temporal trace of a beating between the signal component and the local oscillator. Its FFT after the application of the gaussian window is shown in Fig. B.4(b). One can clearly notice a periodic pattern on the temporal trace and peaks at $\pm 1.5\,GHz$ on the FFT spectrum.

The results for $\Phi_{init} = \pi/2$ are displayed in Fig. B.5. Fig. B.5(a) shows the power evolutions (pump in blue and signal in red) over a single burst. As can be seen, both powers increases strongly for about 20 round-trips at first. This is because this is approximately the number of round-trips needed to "fill" the cavity (we recall that its finesse is about 22). Both powers reach then a quasi steady-state after about 40 round-trips. However one can notice important fluctuations of several dB which are attributed to an imperfect stabilisation. A similar observation can be made on the relative phase evolution in Fig. B.5(b) with important fluctuations

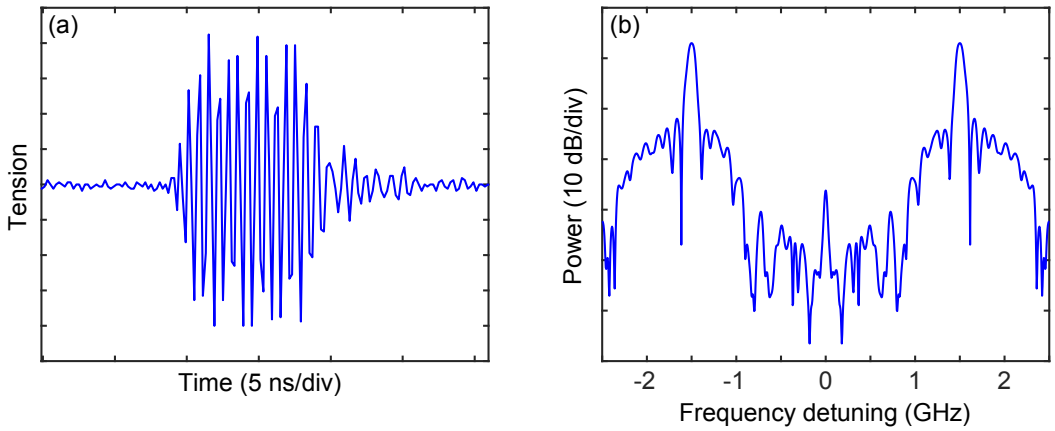

Figure B.4: (a) Temporal trace of beating between the signal component and the local oscillator (zoom). (b) FFT of this beating after application of the gaussian window.

around the steady-state. Fig. B.5(c) shows then the associated phase plane which corresponds to an attractor. However, due to the important fluctuations experienced by the signal power and the relative phase, this attractor is rather big, whereas it should ideally be a point. This issue is mainly solved by implementing averaging in the data processing. Instead of recording and processing a single burst, we record 16 consecutive bursts and perform averaging. This clearly allows to reduce the fluctuations as can be seen in Fig. B.5(d,e) so the attractor is more confined and looks better [Fig. B.5(f)]. Note that we also measured the intracavity spectrum for this case in order to calibrate the two detection channels (pump and signal). This spectrum is shown in Fig. B.6. On this spectrum the signal/idler to pump ratio is -6.5 dB. This was then used to roughly calibrate our system by stating that the signal to pump ratio detected once the steady-state is reached is -6.5 dB.

Noteworthy, the acquisition and processing have been conceived to be short (typically one or two seconds). This is very advantageous as it allows to continuously displays the results while running the experiments. In particular it allows us to see if an adjustment of the frequency detuning f is needed. Indeed, this frequency detuning has to be set at a very precise level (a few hundreds of Hz) so the signal component experiences exactly the same detuning than the pump. If it is not done, the linear phase accumulated every round-trip by the pump and the signal are different, which affects the dynamics. This is easily noticeable as it results in

important linear evolutions of $\Delta\Phi$.

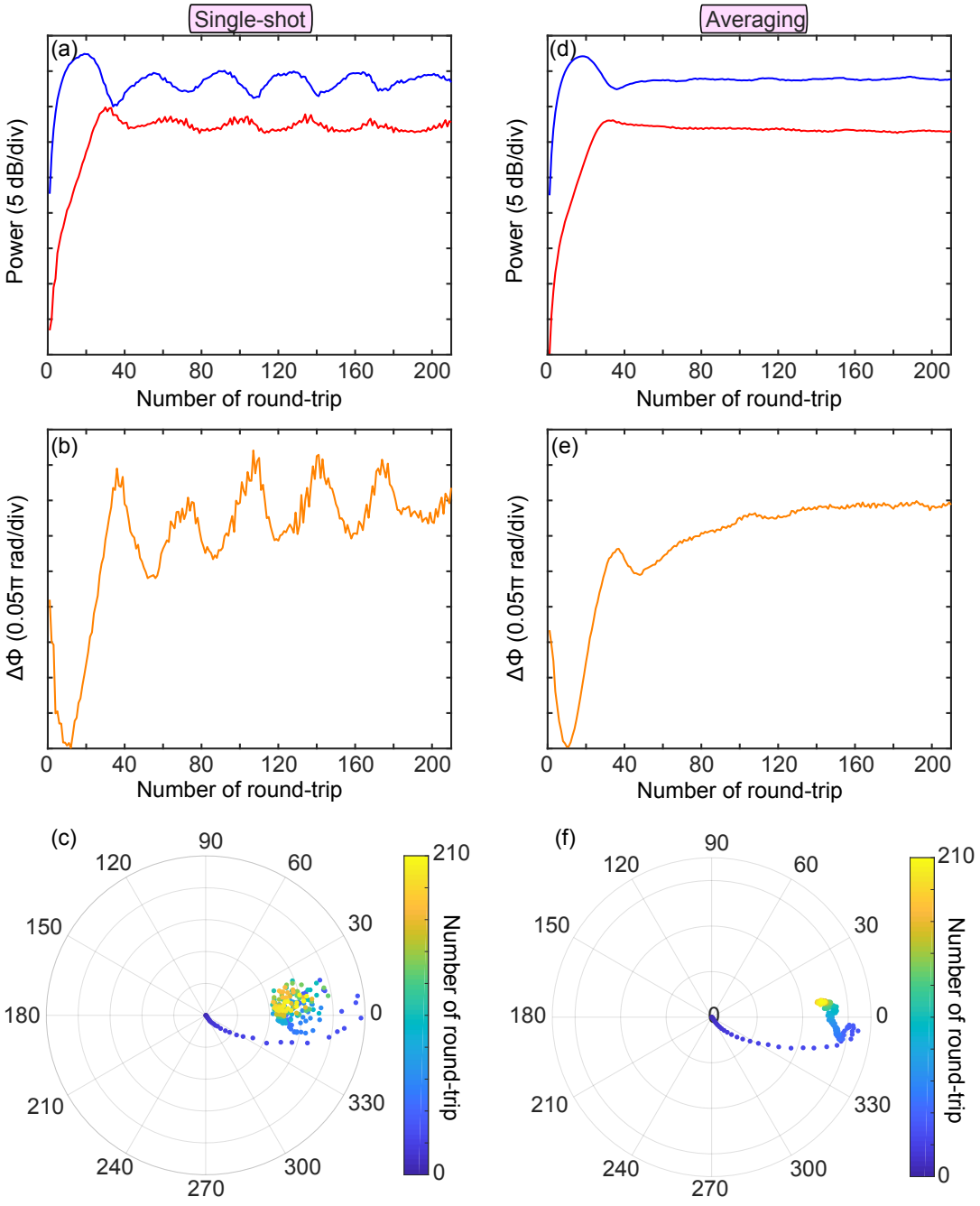

Figure B.5: (a) Single-shot of the pump (blue) and signal (red) power evolutions and (b) relative phase evolution for $\Phi_{init} = \pi/2$ and a single burst. (c) Corresponding phase-plane. (d,e,f) Same but after averaging over 16 consecutives bursts.

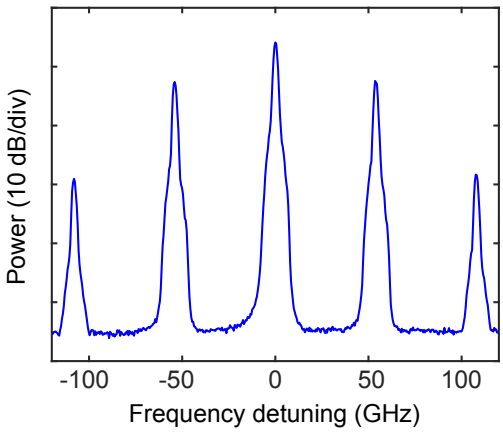

Figure B.6: Intra-cavity spectrum for $\Delta\Phi_{init} = \pi/2$

Experimental Results

Using the same data processing technique than for the previous results, the experiment was repeated 21 times with different values of $\Delta\Phi_{init}$ in the range of $[0, 2\pi]$. To illustrate our results, we display in Fig. B.7 the power evolution curves and the associated phase-planes for three values of $\Delta\Phi_{init}$: 0.95π, 0.85π and 0.70π. As we can see with the power curves in Fig. B.7(a), the pump power evolutions are rather similar for the three different values of $\Delta\Phi_{init}$ but this is not the case for the signal power curves. First, the number of round-trips needed to reach the steady-state varies. For $\Delta\Phi_{init}$ =0.70π (green line) it is around 30 round-trips, while it is around 70 round-trips for $\Delta\Phi_{init}$ =0.85π (red line) and more than 100 round-trips for $\Delta\Phi_{init}$ =0.95π (blue lines). This clearly shows that the initial relative phase have a big impact on the transient stage of the MI process. Moreover, the steady-state signal power are also different. Thus, in addition to having the longest transient stage, the case with $\Delta\Phi_{init}$ =0.95π is characterised by a steady-state signal power about 8 dB lower than for the case with $\Delta\Phi_{init}$ =0.70π. Concerning the phase-plane trajectories [see Fig. B.7(b)], we observe that different values of $\Delta\Phi_{init}$ induce different attractor positions. Once again we redirect the reader to the thesis of Florent Bessin for a detailed discussion on the physics involved with comparison to theory and numerical simulations.

.

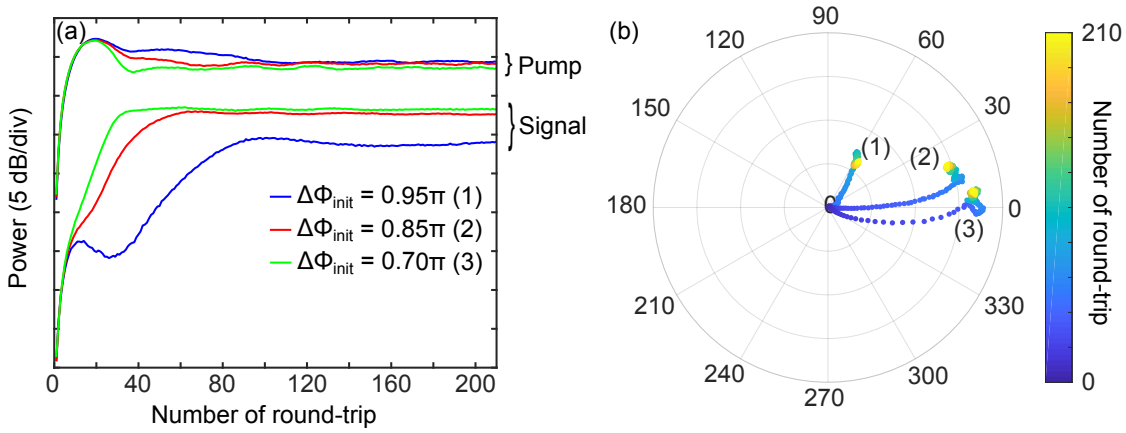

Figure B.7: (a) Pump and signal power evolutions. (b) Corresponding phase-planes.

Summary

- We have adapted the experimental setup previously described in this thesis in order to study the dynamics of seeded MI in a new system: a passive optical fibre-ring cavity.
- Using this new setup, we were able to demonstrate the evolution of the intracavity field towards an attractor in the phase-plane and to highlight the dependence of the process on the initial relative phase of the three-wave input.
- This work paves the way for the experimental investigation of more complex dynamics such as Lorenz chaos [129, 130].

Bibliography

[1] T. Maiman, "Optical and microwave-optical experiments in ruby," *Physical review letters*, vol. 4, no. 11, p. 564, 1960. (document)

[2] J. P. Gordon, H. J. Zeiger, and C. H. Townes, "The maser: new type of microwave amplifier, frequency standard, and spectrometer," *Physical Review*, vol. 99, no. 4, p. 1264, 1955. (document)

[3] P. Franken, A. E. Hill, C. e. Peters, and G. Weinreich, "Generation of optical harmonics," *Physical Review Letters*, vol. 7, no. 4, p. 118, 1961. (document)

[4] K. Kao and G. A. Hockham, "Dielectric-fibre surface waveguides for optical frequencies," in *Proceedings of the Institution of Electrical Engineers*, vol. 113, pp. 1151–1158, IET, 1966. (document)

[5] F. Kapron, D. B. Keck, and R. D. Maurer, "Radiation losses in glass optical waveguides," *Applied Physics Letters*, vol. 17, no. 10, pp. 423–425, 1970. (document)

[6] R. H. Stolen, E. Ippen, and A. Tynes, "Raman oscillation in glass optical waveguide," *Applied Physics Letters*, vol. 20, no. 2, pp. 62–64, 1972. (document), 1.3.2

[7] E. Ippen and R. Stolen, "Stimulated Brillouin scattering in optical fibers," *Applied Physics Letters*, vol. 21, no. 11, pp. 539–541, 1972. (document), 3.2.6

[8] R. Stolen and A. Ashkin, "Optical Kerr effect in glass waveguide," *Applied Physics Letters*, vol. 22, no. 6, pp. 294–296, 1973. (document)

[9] R. Stolen, J. Bjorkholm, and A. Ashkin, "Phase-matched three-wave mixing in silica fiber optical waveguides," *Applied Physics Letters*, vol. 24, no. 7, pp. 308–310, 1974. (document)

[10] R. Stolen, "Phase-matched-stimulated four-photon mixing in silica-fiber waveguides," *IEEE Journal of Quantum Electronics*, vol. 11, no. 3, pp. 100–103, 1975. (document), 2.2

[11] R. Stolen and C. Lin, "Self-phase-modulation in silica optical fibers," *Physical Review A*, vol. 17, no. 4, p. 1448, 1978. (document)

[12] L. F. Mollenauer, R. H. Stolen, and J. P. Gordon, "Experimental observation of picosecond pulse narrowing and solitons in optical fibers," *Physical Review Letters*, vol. 45, no. 13, p. 1095, 1980. (document)

[13] K. Tai, A. Hasegawa, and A. Tomita, "Observation of modulational instability in optical fibers," *Physical review letters*, vol. 56, no. 2, p. 135, 1986. (document), 2.2

[14] V. E. Zakharov and L. Ostrovsky, "Modulation instability: the beginning," *Physica D: Nonlinear Phenomena*, vol. 238, no. 5, pp. 540–548, 2009. (document), 2, 2.2

[15] T. Taniuti and H. Washimi, "Self-trapping and instability of hydromagnetic waves along the magnetic field in a cold plasma," *Physical review letters*, vol. 21, no. 4, p. 209, 1968. (document), 2.2

[16] K. E. Strecker, G. B. Partridge, A. G. Truscott, and R. G. Hulet, "Formation and propagation of matter-wave soliton trains," *Nature*, vol. 417, no. 6885, p. 150, 2002. (document), 2.2

[17] T. B. Benjamin and J. Feir, "The disintegration of wave trains on deep water part 1. theory," *Journal of Fluid Mechanics*, vol. 27, no. 3, pp. 417–430, 1967. (document), 2.2

[18] M. E. Marhic, *Fiber optical parametric amplifiers, oscillators and related devices*. Cambridge university press, 2008. (document), 2.2, 2.3.1

[19] N. Akhmediev, A. Ankiewicz, J. Soto-Crespo, and J. M. Dudley, "Universal triangular spectra in parametrically-driven systems," *Physics Letters A*, vol. 375, no. 3, pp. 775–779, 2011. (document), 2.3.2

[20] M. A. Porter, N. J. Zabusky, B. Hu, and D. K. Campbell, "Fermi, Pasta, Ulam and the birth of experimental mathematics: A numerical experiment that Enrico Fermi, John Pasta, and Stanislaw Ulam reported 54 years ago continues to inspire discovery," *American Scientist*, vol. 97, no. 3, pp. 214–221, 2009. (document), 2.1

[21] E. Fermi, P. Pasta, S. Ulam, and M. Tsingou, "Studies of the nonlinear problems," tech. rep., Los Alamos Scientific Lab., N. Mex., 1955. (document), 2.1

[22] N. J. Zabusky and M. D. Kruskal, "Interaction of" solitons" in a collisionless plasma and the recurrence of initial states," *Physical review letters*, vol. 15, no. 6, p. 240, 1965. (document), 2.1

[23] N. J. Zabusky, "Fermi–Pasta–Ulam, solitons and the fabric of nonlinear and computational science: history, synergetics, and visiometrics," *Chaos: An Interdisciplinary Journal of Nonlinear Science*, vol. 15, no. 1, p. 015102, 2005. (document), 2.1

[24] N. Akhmediev, V. Eleonskii, and N. Kulagin, "Exact first-order solutions of the nonlinear Schrödinger equation," *Theoretical and mathematical physics*, vol. 72, no. 2, pp. 809–818, 1987. (document), 2.3.2, 6.3.3, 6.3.3, 6.3.3

[25] D. Solli, C. Ropers, P. Koonath, and B. Jalali, "Optical rogue waves," *Nature*, vol. 450, no. 7172, p. 1054, 2007. (document)

[26] N. Akhmediev, J. M. Soto-Crespo, and A. Ankiewicz, "Extreme waves that appear from nowhere: on the nature of rogue waves," *Physics Letters A*, vol. 373, no. 25, pp. 2137–2145, 2009. (document)

[27] N. Akhmediev, J. M. Dudley, D. Solli, and S. Turitsyn, "Recent progress in investigating optical rogue waves," *Journal of Optics*, vol. 15, no. 6, p. 060201, 2013. (document), 2.3.2

[28] J. M. Dudley, F. Dias, M. Erkintalo, and G. Genty, "Instabilities, breathers and rogue waves in optics," *Nature Photonics*, vol. 8, no. 10, p. 755, 2014. (document), 1.4, 2.3.2, 2.3.2, 4.3.2

[29] N. Akhmediev, B. Kibler, F. Baronio, M. Belić, W.-P. Zhong, Y. Zhang, W. Chang, J. M. Soto-Crespo, P. Vouzas, P. Grelu, *et al.*, "Roadmap on optical rogue waves and extreme events," *Journal of Optics*, vol. 18, no. 6, p. 063001, 2016. (document), 2.3.2

[30] J. M. Dudley, G. Genty, F. Dias, B. Kibler, and N. Akhmediev, "Modulation instability, Akhmediev breathers and continuous wave supercontinuum generation," *Optics express*, vol. 17, no. 24, pp. 21497–21508, 2009. (document), 2.3.2

[31] G. Van Simaeys, P. Emplit, and M. Haelterman, "Experimental demonstration of the Fermi-Pasta-Ulam recurrence in a modulationally unstable optical wave," *Physical review letters*, vol. 87, no. 3, p. 033902, 2001. (document), 2.1, 3.1

[32] B. M. Lake, H. C. Yuen, H. Rungaldier, and W. E. Ferguson, "Nonlinear deep-water waves: theory and experiment. part 2. evolution of a continuous wave train," *Journal of Fluid Mechanics*, vol. 83, no. 1, pp. 49–74, 1977. (document), 2.1

[33] D. Jäger, "Soliton propagation along periodic-loaded transmission line," *Applied physics*, vol. 16, no. 1, pp. 35–38, 1978. (document), 2.1

[34] A. Kobyakov, M. Sauer, and D. Chowdhury, "Stimulated Brillouin scattering in optical fibers," *Advances in optics and photonics*, vol. 2, no. 1, pp. 1–59, 2010. (document), 3.2.6

[35] N. N. Akhmediev, "Nonlinear physics: Déjà vu in optics," *Nature*, vol. 413, no. 6853, p. 267, 2001. (document), 2.1

[36] A. Chabchoub, N. Hoffmann, and N. Akhmediev, "Rogue wave observation in a water wave tank," *Physical Review Letters*, vol. 106, no. 20, p. 204502, 2011. (document)

[37] O. Kimmoun, H. Hsu, H. Branger, M. Li, Y. Chen, C. Kharif, M. Onorato, E. Kelleher, B. Kibler, N. Akhmediev, *et al.*, "Modulation instability and phase-shifted Fermi-Pasta-Ulam recurrence," *Scientific reports*, vol. 6, p. 28516, 2016. (document), 2.1, 2.3.2, 2.4, 4, 4.1

[38] A. Mussot, A. Kudlinski, M. Droques, P. Szriftgiser, and N. Akhmediev, "Fermi-Pasta-Ulam recurrence in nonlinear fiber optics: the role of reversible and irreversible losses," *Physical Review X*, vol. 4, no. 1, p. 011054, 2014. (document), 2.1, 2.4, 3.1

[39] B. Kibler, J. Fatome, C. Finot, G. Millot, F. Dias, G. Genty, N. Akhmediev, and J. M. Dudley, "The Peregrine soliton in nonlinear fibre optics," *Nature Physics*, vol. 6, no. 10, p. 790, 2010. (document), 2.3.2, 3.1

[40] B. Kibler, J. Fatome, C. Finot, G. Millot, G. Genty, B. Wetzel, N. Akhmediev, F. Dias, and J. M. Dudley, "Observation of Kuznetsov-Ma soliton dynamics in optical fibre," *Scientific reports*, vol. 2, p. 463, 2012. (document), 2.3.2

[41] B. Frisquet, B. Kibler, and G. Millot, "Collision of Akhmediev breathers in nonlinear fiber optics," *Physical Review X*, vol. 3, no. 4, p. 041032, 2013. (document), 2.3.2, 5.2.2, 6

[42] A. Mussot, C. Naveau, M. Conforti, A. Kudlinski, F. Copie, P. Szriftgiser, and S. Trillo, "Fibre multi-wave mixing combs reveal the broken symmetry of Fermi–Pasta–Ulam recurrence," *Nature photonics*, vol. 12, no. 5, p. 303, 2018. (document), 2.3.1, 2.3.2, 3, 3.2.5, 4.3.2, 6.3.3

[43] C. Naveau, P. Szriftgiser, A. Kudlinski, M. Conforti, S. Trillo, and A. Mussot, "Full-field characterization of breather dynamics over the whole length of an optical fiber," *Optics letters*, vol. 44, no. 4, pp. 763–766, 2019. (document), 2.3.2, 3.2.5, 6.3.3

[44] C. Naveau, P. Szriftgiser, A. Kudlinski, M. Conforti, S. Trillo, and A. Mussot, "Experimental characterization of recurrences and separatrix crossing in modulation instability," to be published in Optics Letters. (document), 2.3.2, 6.3.3

[45] P. Grinevich and P. Santini, "The exact rogue wave recurrence in the NLS periodic setting via matched asymptotic expansions, for 1 and 2 unstable modes," *Physics Letters A*, vol. 382, no. 14, pp. 973–979, 2018. (document), 2.3.2, 5, 5.1, 5.2.2, 5.2.2, 6.3.3

[46] M. J. Adams, *An introduction to optical waveguides*, vol. 14. Wiley New York, 1981. 1.1

[47] G. Agrawal, "Nonlinear fiber optics 5th ed," 2012. 1.1, 1.3.1, 1.3.2, 1.4, 1.4, 1.4

[48] J. Stone and G. E. Walrafen, "Overtone vibrations of OH groups in fused silica optical fibers," *The Journal of Chemical Physics*, vol. 76, no. 4, pp. 1712–1722, 1982. 1.2.1

[49] B. Lee, "Review of the present status of optical fiber sensors," *Optical fiber technology*, vol. 9, no. 2, pp. 57–79, 2003. 1.2.1

[50] M. Nakazawa, "Rayleigh backscattering theory for single-mode optical fibers," *JOSA*, vol. 73, no. 9, pp. 1175–1180, 1983. 1.2.1

[51] Corning, *SMF-28 Ultra Optical Fiber*, 2014. 1.2.1, 1.2.2, 3.2.6

[52] Y. Tamura, H. Sakuma, K. Morita, M. Suzuki, Y. Yamamoto, K. Shimada, Y. Honma, K. Sohma, T. Fujii, and T. Hasegawa, "Lowest-ever 0.1419-db/km loss optical fiber," in *Optical Fiber Communication Conference*, pp. Th5D–1, Optical Society of America, 2017. 1.2.1

[53] P. Russell, "Photonic crystal fibers," *Science*, vol. 299, no. 5605, pp. 358–362, 2003. 1.2.2

[54] J. C. Knight, "Photonic crystal fibres," *Nature*, vol. 424, no. 6950, p. 847, 2003. 1.2.2

[55] D. Strickland and G. Mourou, "Compression of amplified chirped optical pulses," *Optics communications*, vol. 55, no. 6, pp. 447–449, 1985. 1.2.2

[56] C. V. Raman and K. S. Krishnan, "A new type of secondary radiation," *Nature*, vol. 121, no. 3048, p. 501, 1928. 1.3.2

[57] C. Headley and G. Agrawal, *Raman amplification in fiber optical communication systems*. Academic press, 2005. 1.3.2, 3.2.5

[58] D. Hollenbeck and C. D. Cantrell, "Multiple-vibrational-mode model for fiber-optic Raman gain spectrum and response function," *JOSA B*, vol. 19, no. 12, pp. 2886–2892, 2002. 1.1

[59] T. Dauxois, "Fermi, Pasta, Ulam and a mysterious lady," *arXiv preprint arXiv:0801.1590*, 2008. 2

[60] E. Fermi, J. Pasta, and S. Ulam, *Collected Papers of Enrico Fermi*, vol. 2. Univ. Chicago Press, 1965. 2.1

[61] Y. V. Lvov and M. Onorato, "Double scaling in the relaxation time in the β-Fermi-Pasta-Ulam-Tsingou model," *Physical review letters*, vol. 120, no. 14, p. 144301, 2018. 2.1

[62] M. Onorato, L. Vozella, D. Proment, and Y. V. Lvov, "Route to thermalization in the α-Fermi–Pasta–Ulam system," *Proceedings of the National Academy of Sciences*, vol. 112, no. 14, pp. 4208–4213, 2015. 2.1

[63] J. Beeckman, X. Hutsebaut, M. Haelterman, and K. Neyts, "Induced modulation instability and recurrence in nematic liquid crystals," *Optics express*, vol. 15, no. 18, pp. 11185–11195, 2007. 2.1

[64] D. Pierangeli, M. Flammini, L. Zhang, G. Marcucci, A. Agranat, P. Grinevich, P. Santini, C. Conti, and E. DelRe, "Observation of Fermi-Pasta-Ulam-Tsingou recurrence and its exact dynamics," *Physical Review X*, vol. 8, no. 4, p. 041017, 2018. 2.1, 2.3.2, 5

[65] G. Van Simaeys, P. Emplit, and M. Haelterman, "Experimental study of the reversible behavior of modulational instability in optical fibers," *JOSA B*, vol. 19, no. 3, pp. 477–486, 2002. 2.1, 3.1

[66] K. Hammani, B. Wetzel, B. Kibler, J. Fatome, C. Finot, G. Millot, N. Akhmediev, and J. M. Dudley, "Spectral dynamics of modulation instability described using Akhmediev breather theory," *Optics letters*, vol. 36, no. 11, pp. 2140–2142, 2011. 2.1, 2.3.2, 3.1

[67] X. Hu, W. Chen, Y. Lu, Z. Yu, M. Chen, and Z. Meng, "Distributed measurement of Fermi–Pasta–Ulam recurrence in optical fibers," *IEEE Photonics Technology Letters*, vol. 30, no. 1, pp. 47–50, 2018. 2.1, 3.1

[68] T. Torounidis, P. A. Andrekson, and B.-E. Olsson, "Fiber-optical parametric amplifier with 70-db gain," *IEEE Photonics Technology Letters*, vol. 18, no. 10, pp. 1194–1196, 2006. 2.2

[69] R. Malik, A. Kumpera, M. Karlsson, and P. A. Andrekson, "Demonstration of ultra wideband phase-sensitive fiber optical parametric amplifier," *IEEE Photonics Technology Letters*, vol. 28, no. 2, pp. 175–177, 2015. 2.2

[70] T. Torounidis and P. Andrekson, "Broadband single-pumped fiber-optic parametric amplifiers," *IEEE Photonics Technology Letters*, vol. 19, no. 9, pp. 650–652, 2007. 2.2

[71] S. Pitois and G. Millot, "Experimental observation of a new modulational instability spectral window induced by fourth-order dispersion in a normally dispersive single-mode optical fiber," *Optics communications*, vol. 226, no. 1-6, pp. 415–422, 2003. 2.2, 6.3.3

[72] S. Murdoch, R. Leonhardt, and J. Harvey, "Polarization modulation instability in weakly birefringent fibers," *Optics letters*, vol. 20, no. 8, pp. 866–868, 1995. 2.2

[73] M. Droques, A. Kudlinski, G. Bouwmans, G. Martinelli, and A. Mussot, "Experimental demonstration of modulation instability in an optical fiber with a periodic dispersion landscape," *Optics letters*, vol. 37, no. 23, pp. 4832–4834, 2012. 2.2

[74] K. Krupa, A. Tonello, A. Barthélémy, V. Couderc, B. M. Shalaby, A. Bendahmane, G. Millot, and S. Wabnitz, "Observation of geometric parametric instability induced by the periodic spatial self-imaging of multimode waves," *Physical review letters*, vol. 116, no. 18, p. 183901, 2016. 2.2

[75] S. Trillo and S. Wabnitz, "Dynamics of the nonlinear modulational instability in optical fibers," *Optics letters*, vol. 16, no. 13, pp. 986–988, 1991. 2.3, 2.3.1, 4

[76] G. Cappellini and S. Trillo, "Third-order three-wave mixing in single-mode fibers: exact solutions and spatial instability effects," *JOSA B*, vol. 8, no. 4, pp. 824–838, 1991. 2.3, 2.3.1, 2.3.1

[77] J. Hansryd, P. A. Andrekson, M. Westlund, J. Li, and P.-O. Hedekvist, "Fiber-based optical parametric amplifiers and their applications," *IEEE Journal of Selected Topics in Quantum Electronics*, vol. 8, no. 3, pp. 506–520, 2002. 2.3.1

[78] M. E. Marhic, P. A. Andrekson, P. Petropoulos, S. Radic, C. Peucheret, and M. Jazayerifar, "Fiber optical parametric amplifiers in optical communication systems," *Laser & photonics reviews*, vol. 9, no. 1, pp. 50–74, 2015. 2.3.1

[79] E. I. Butikov, "The rigid pendulum-an antique but evergreen physical model," *European Journal of Physics*, vol. 20, no. 6, p. 429, 1999. 2.3.1

[80] A. Shabat and V. Zakharov, "Exact theory of two-dimensional self-focusing and one-dimensional self-modulation of waves in nonlinear media," *Soviet physics JETP*, vol. 34, no. 1, p. 62, 1972. 2.3.2

[81] V. E. Zakharov and A. B. Shabat, "A scheme for integrating the nonlinear equations of mathematical physics by the method of the inverse scattering problem. i," *Functional analysis and its applications*, vol. 8, no. 3, pp. 226–235, 1974. 2.3.2

[82] V. E. Zakharov and A. B. Shabat, "Integration of nonlinear equations of mathematical physics by the method of inverse scattering. ii," *Functional Analysis and Its Applications*, vol. 13, no. 3, pp. 166–174, 1979. 2.3.2

[83] N. Akhmediev and A. Ankiewicz, *Dissipative solitons: from optics to biology and medicine*, vol. 751. Springer Science & Business Media, 2008. 2.3.2

[84] N. Akhmediev and V. Korneev, "Modulation instability and periodic solutions of the nonlinear Schrödinger equation," *Theoretical and Mathematical Physics*, vol. 69, no. 2, pp. 1089–1093, 1986. 2.3.2, 2.3.2

[85] D. Peregrine, "Water waves, nonlinear Schrödinger equations and their solutions," *The ANZIAM Journal*, vol. 25, no. 1, pp. 16–43, 1983. 2.3.2

[86] E. Kuznetsov, A. Rubenchik, and V. E. Zakharov, "Soliton stability in plasmas and hydrodynamics," *Physics Reports*, vol. 142, no. 3, pp. 103–165, 1986. 2.3.2

[87] Y.-C. Ma, "The perturbed plane-wave solutions of the cubic Schrödinger equation," *Studies in Applied Mathematics*, vol. 60, no. 1, pp. 43–58, 1979. 2.3.2

[88] N. Akhmediev, A. Ankiewicz, and J. Soto-Crespo, "Rogue waves and rational solutions of the nonlinear Schrödinger equation," *Physical Review E*, vol. 80, no. 2, p. 026601, 2009. 2.3.2

[89] N. Devine, A. Ankiewicz, G. Genty, J. M. Dudley, and N. Akhmediev, "Recurrence phase shift in Fermi–Pasta–Ulam nonlinear dynamics," *Physics Letters A*, vol. 375, no. 46, pp. 4158–4161, 2011. 2.3.2

[90] M. Erkintalo, G. Genty, B. Wetzel, and J. M. Dudley, "Akhmediev breather evolution in optical fiber for realistic initial conditions," *Physics Letters A*, vol. 375, no. 19, pp. 2029–2034, 2011. 2.3.2, 2.3.2, 5.1

[91] P. Grinevich and P. Santini, "The finite gap method and the analytic description of the exact rogue wave recurrence in the periodic NLS Cauchy problem. 1," *Nonlinearity*, vol. 31, no. 11, p. 5258, 2018. 2.3.2

[92] M. Erkintalo, K. Hammani, B. Kibler, C. Finot, N. Akhmediev, J. M. Dudley, and G. Genty, "Higher-order modulation instability in nonlinear fiber optics," *Physical review letters*, vol. 107, no. 25, p. 253901, 2011. 2.3.2

[93] D. J. Kedziora, A. Ankiewicz, and N. Akhmediev, "Second-order nonlinear Schrödinger equation breather solutions in the degenerate and rogue wave limits," *Physical Review E*, vol. 85, no. 6, p. 066601, 2012. 2.3.2, 6.1

[94] A. Chabchoub, N. Hoffmann, M. Onorato, and N. Akhmediev, "Super rogue waves: observation of a higher-order breather in water waves," *Physical Review X*, vol. 2, no. 1, p. 011015, 2012. 2.3.2

[95] V. E. Zakharov and A. Gelash, "Nonlinear stage of modulation instability," *Physical review letters*, vol. 111, no. 5, p. 054101, 2013. 2.3.2

[96] B. Kibler, A. Chabchoub, A. Gelash, N. Akhmediev, and V. E. Zakharov, "Superregular breathers in optics and hydrodynamics: omnipresent modulation instability beyond simple periodicity," *Physical Review X*, vol. 5, no. 4, p. 041026, 2015. 2.3.2

[97] S. Wabnitz and B. Wetzel, "Instability and noise-induced thermalization of Fermi–Pasta–Ulam recurrence in the nonlinear Schrödinger equation," *Physics Letters A*, vol. 378, no. 37, pp. 2750–2756, 2014. 2.4, 6.3.3

[98] C. Cambournac, H. Maillotte, E. Lantz, J. M. Dudley, and M. Chauvet, "Spatiotemporal behavior of periodic arrays of spatial solitons in a planar waveguide with relaxing kerr nonlinearity," *JOSA B*, vol. 19, no. 3, pp. 574–585, 2002. 2.4

[99] G. Xu, K. Hammani, A. Chabchoub, J. M. Dudley, B. Kibler, and C. Finot, "Phase evolution of Peregrine-like solitons in nonlinear fiber optics," in *Conference on Lasers & Electro-Optics Europe*, 2019. 3.1, 4.3, 6.3.3

[100] L. Thévenaz, "Review and progress in distributed fiber sensing," in *Optical fiber sensors*, p. ThC1, Optical Society of America, 2006. 3.1

[101] A. Vedadi, D. Alasia, E. Lantz, H. Maillotte, L. Thévenaz, M. Gonzalez-Herraez, and T. Sylvestre, "Brillouin optical time-domain analysis of fiber-optic parametric amplifiers," *IEEE Photonics Technology Letters*, vol. 19, no. 3, pp. 179–181, 2007. 3.1

[102] F. Alishahi, A. Vedadi, M. A. Shoaie, M. A. Soto, A. Denisov, K. Mehrany, L. Thévenaz, and C.-S. Brès, "Power evolution along phase-sensitive parametric amplifiers: an experimental survey," *Optics letters*, vol. 39, no. 21, pp. 6114–6117, 2014. 3.1

[103] M. Wuilpart, G. Ravet, P. Megret, and M. Blondel, "Distributed measurement of raman gain spectrum in concatenations of optical fibres with otdr," *Electronics letters*, vol. 39, no. 1, pp. 88–89, 2003. 3.1

[104] G. Ravet, A. Mussot, M. Wuilpart, A. Kudlinski, C. Caucheteur, and P. Mégret, "Distributed measurement of modulation instability along optical fibers,"

in *IEEE Photonics Society Summer Topicals 2010*, pp. 166–167, IEEE, 2010. 3.1

[105] R. Hontinfinde, S. Coulibaly, P. Megret, M. Taki, and M. Wuilpart, "Nondestructive distributed measurement of supercontinuum generation along highly nonlinear optical fibers," *Optics letters*, vol. 42, no. 9, pp. 1716–1719, 2017. 3.1

[106] E. Ip, A. P. T. Lau, D. J. Barros, and J. M. Kahn, "Coherent detection in optical fiber systems," *Optics express*, vol. 16, no. 2, pp. 753–791, 2008. 3.2

[107] F. Friederich, G. Schuricht, A. Deninger, F. Lison, G. Spickermann, P. H. Bolívar, and H. G. Roskos, "Phase-locking of the beat signal of two distributed-feedback diode lasers to oscillators working in the mhz to thz range," *Optics express*, vol. 18, no. 8, pp. 8621–8629, 2010. 3.2.3

[108] P. Healey, "Fading in heterodyne OTDR," *Electronics letters*, vol. 20, no. 1, pp. 30–32, 1984. 3.2.4

[109] H. Izumita, S.-I. Furukawa, Y. Koyamada, and I. Sankawa, "Fading noise reduction in coherent OTDR," *IEEE Photonics Technology Letters*, vol. 4, no. 2, pp. 201–203, 1992. 3.2.4

[110] G. Yang, X. Fan, B. Wang, Q. Liu, and Z. He, "Polarization fading elimination in phase-extracted OTDR for distributed fiber-optic vibration sensing," in *2016 21st OptoElectronics and Communications Conference (OECC) held jointly with 2016 International Conference on Photonics in Switching (PS)*, pp. 1–3, IEEE, 2016. 3.2.4

[111] G. Xu, M. Conforti, A. Kudlinski, A. Mussot, and S. Trillo, "Dispersive dam-break flow of a photon fluid," *Physical review letters*, vol. 118, no. 25, p. 254101, 2017. 3.2.5

[112] A. E. Kraych, P. Suret, G. El, and S. Randoux, "Nonlinear evolution of the locally induced modulational instability in fiber optics," *Physical review letters*, vol. 122, no. 5, p. 054101, 2019. 3.2.5

[113] H. T. Moon, "Homoclinic crossings and pattern selection," *Physical review letters*, vol. 64, no. 4, p. 412, 1990. 4

[114] M. J. Ablowitz and B. Herbst, "On homoclinic structure and numerically induced chaos for the nonlinear Schrödinger equation," *SIAM Journal on Applied Mathematics*, vol. 50, no. 2, pp. 339–351, 1990. 4

[115] R. Trebino, *Frequency-resolved optical gating: the measurement of ultrashort laser pulses*. Springer Science & Business Media, 2012. 4.3

[116] C. Iaconis and I. A. Walmsley, "Spectral phase interferometry for direct electric-field reconstruction of ultrashort optical pulses," *Optics letters*, vol. 23, no. 10, pp. 792–794, 1998. 4.3

[117] I. A. Walmsley and C. Dorrer, "Characterization of ultrashort electromagnetic pulses," *Advances in Optics and Photonics*, vol. 1, no. 2, pp. 308–437, 2009. 4.3

[118] K. Goda and B. Jalali, "Dispersive Fourier transformation for fast continuous single-shot measurements," *Nature Photonics*, vol. 7, no. 2, p. 102, 2013. 4.3, 6.3.3

[119] R. Salem, M. A. Foster, and A. L. Gaeta, "Application of space–time duality to ultrahigh-speed optical signal processing," *Advances in Optics and Photonics*, vol. 5, no. 3, pp. 274–317, 2013. 4.3, 6.3.3

[120] A. Tikan, S. Bielawski, C. Szwaj, S. Randoux, and P. Suret, "Single-shot measurement of phase and amplitude by using a heterodyne time-lens system and ultrafast digital time-holography," *Nature Photonics*, vol. 12, no. 4, p. 228, 2018. 4.3

[121] P. Ryczkowski, M. Närhi, C. Billet, J.-M. Merolla, G. Genty, and J. Dudley, "Real-time full-field characterization of transient dissipative soliton dynamics in a mode-locked laser," *Nature Photonics*, vol. 12, no. 4, p. 221, 2018. 4.3, 6.3.3

[122] C. Lei and K. Goda, "The complete optical oscilloscope," *Nature Photonics*, vol. 12, no. 4, p. 190, 2018. 4.3

[123] S. Boscolo and C. Finot, *Shaping light in nonlinear optical fibers*. John Wiley & Sons, 2017. 6.1

[124] X. Liu and B. Lee, "A fast and stable method for Raman amplifier propagation equations," *Optics express*, vol. 11, no. 18, pp. 2163–2176, 2003. 6.3.3

[125] M. Santagiustina, "Exact integral solution of saturation and depletion in forward and backward optical fiber Raman amplifiers," *Optics letters*, vol. 32, no. 20, pp. 3023–3025, 2007. 6.3.3

[126] M. Conforti, A. Mussot, A. Kudlinski, S. R. Nodari, G. Dujardin, S. De Biévre, A. Armaroli, and S. Trillo, "Heteroclinic structure of parametric resonance in the nonlinear Schrödinger equation," *Physical review letters*, vol. 117, no. 1, p. 013901, 2016. 6.3.3

[127] A. Mussot, M. Conforti, S. Trillo, F. Copie, and A. Kudlinski, "Modulation instability in dispersion oscillating fibers," *Advances in Optics and Photonics*, vol. 10, no. 1, pp. 1–42, 2018. 6.3.3

[128] V. Torres-Company and A. M. Weiner, "Optical frequency comb technology for ultra-broadband radio-frequency photonics," *Laser & Photonics Reviews*, vol. 8, no. 3, pp. 368–393, 2014. 6.3.3

[129] E. N. Lorenz, "Deterministic nonperiodic flow," *Journal of the atmospheric sciences*, vol. 20, no. 2, pp. 130–141, 1963. 6.3.3, 6.3.3, 6.3.3

[130] M. Haelterman, S. Trillo, and S. Wabnitz, "Low dimensional modulational chaos in diffractive nonlinear cavities," *Optics communications*, vol. 93, no. 5-6, pp. 343–349, 1992. 6.3.3, 6.3.3, 6.3.3

[131] P. F. Byrd and M. D. Friedman, *Handbook of elliptic integrals for engineers and physicists*, vol. 67. Springer, 2013. 6.3.3

[132] P. Grelu, *Nonlinear optical cavity dynamics: from microresonators to fiber lasers*. John Wiley & Sons, 2015. 6.3.3, 6.3.3

[133] M. Haelterman, S. Trillo, and S. Wabnitz, "Dissipative modulation instability in a nonlinear dispersive ring cavity," *Optics communications*, vol. 91, no. 5-6, pp. 401–407, 1992. 6.3.3

[134] M. Haelterman, S. Trillo, and S. Wabnitz, "Additive-modulation-instability ring laser in the normal dispersion regime of a fiber," *Optics letters*, vol. 17, no. 10, pp. 745–747, 1992. 6.3.3

[135] A. F. Runge, N. G. Broderick, and M. Erkintalo, "Observation of soliton explosions in a passively mode-locked fiber laser," *Optica*, vol. 2, no. 1, pp. 36–39, 2015. 6.3.3

[136] G. Herink, B. Jalali, C. Ropers, and D. Solli, "Resolving the build-up of femtosecond mode-locking with single-shot spectroscopy at 90 Mhz frame rate," *Nature Photonics*, vol. 10, no. 5, p. 321, 2016. 6.3.3

[137] J. Hammer, P. Hosseini, C. R. Menyuk, P. S. J. Russell, and N. Y. Joly, "Single-shot reconstruction of spectral amplitude and phase in a fiber ring cavity at a 80 Mhz repetition rate," *Optics letters*, vol. 41, no. 20, pp. 4641–4644, 2016. 6.3.3

[138] F. Copie, *Modulation instabilities in dispersion oscillating passive fiber-ring cavities*. PhD thesis, University of Lille 1, 2017. 6.3.3

List of author's publications

Publications in peer-reviewed international journals:

- A. Mussot, C.Naveau, M. Conforti, A. Kudlinski, F. Copie, P. Szriftgiser, and S. Trillo, "Fibre multi-wave mixing combs reveal the broken symmetry of Fermi--Pasta--Ulam recurrence", Nature Photonics 12, 5 (2018), pp. 303-308.

- C. Naveau, P. Szriftgiser, A. Kudlinski, M. Conforti, S. Trillo, and A. Mussot, "Full-field characterization of breather dynamics over the whole length of an optical fiber", Optics letters 44, 4 (2019), pp. 763-766.

- C. Naveau, P. Szriftgiser, A. Kudlinski, M. Conforti, S. Trillo, and A. Mussot, "Experimental characterization of recurrences and separatrix crossing in modulation instability", to be published in Optics Letters.

Posters in peer-reviewed international conferences:

- **C. Naveau**, P. Szriftgiser, M. Conforti, A. Kudlinski, S. Trillo, and A. Mussot, "Spatio temporal observation of the Fermi Pasta Ulam recurrence in optical fibers", Frontier in Optics, Washington DC, USA (2018).

- **C. Naveau**, P. Szriftgiser, A. Kudlinski, M. Conforti, S. Trillo, and A. Mussot, "Spatio-temporal characterization of the electric field of breathers in an optical fiber", CLEO Europe/EQEC, Munich, Germany (2019).

Oral in peer-reviewed international conferences:

- **C. Naveau**, P. Szriftgiser, F. Copie, M. Conforti, A. Kudlinski, S. Trillo, and A. Mussot, "Non-invasive distributed characterization in phase and intensity

of the nonlinear stage of modulation instability", Optical Fiber Conference, San Diego, USA (2018).

- **C. Naveau**, P. Szriftgiser, A. Kudlinski, M. Conforti, S. Trillo, and A. Mussot, "Experimental validation in optical fibers of multiple Fermi- Pasta-Ulam-Tsingou recurrences theory", CLEO Europe/EQEC, Munich, Germany (2019).

Invited oral in peer-reviewed international conferences:

- **A. Mussot**, P. Szriftgiser, C. Naveau, A. Kudlinski, M. Conforti, F. Copie and S. Trillo, "Non-destructive phase and intensity distributed measurements of the nonlinear stage of modulation instability in optical fibers", SPIE Photonics West LASE, San Francisco, USA (2018).

- **A. Mussot**, C. Naveau, F. Bessin, P. Szriftgiser, M. Conforti, A. Kudlinski, and S. Trillo, "Full characterisation in phase and amplitude of the Fermi Pasta Ulam recurrence process in optical fibers", Days on Diffraction, St Petersburg, Russia (2018).

- **A. Mussot**, C. Naveau, F. Bessin, P. Szriftgiser, M. Conforti, A. Kudlinski, and S. Trillo, "Full characterisation in phase and amplitude of the Fermi Pasta Ulam recurrence process in optical fibers", International Conference on Laser Optics, St Petersburg, Russia (2018).

- **A. Mussot**, C. Naveau, P. Szriftgiser, M. Conforti, A. Kudlinski, and S. Trillo, "Observation of the symmetry breaking of the Fermi-Pasta-Ulam recurrence in optical fibers", Nonlinear Photonics, Zurich, Switzerland (2018).

- **A. Mussot**, C. Naveau, F. Bessin, P. Szriftgiser, M. Conforti, A. Kudlinski, and S. Trillo, "Observation of the symmetry breaking of the Fermi-Pasta-Ulam recurrence in nonlinear optical fibers", OSA Latin America Optics and Photonics Conference, Lima, Peru (2018).

- **A. Mussot**, C. Naveau, F. Bessin, P. Szriftgiser, M. Conforti, A. Kudlinski, and S. Trillo, "New Insights on Modulation Instability in Optical Fibers", Optical Fiber Conference, San Diego, USA (2019).

- **S. Trillo**, C. Naveau, P. Szriftgiser, M. Conforti, A. Kudlinski, F. Copie and A. Mussot, "Nonlinear Modulational Instability: Recurrences, Broken Symmetry, and Breathers", Nonlinear Optics (NLO), Hawaii, USA (2019).

- **S. Trillo**, C. Naveau, P. Szriftgiser, M. Conforti, A. Kudlinski, F. Copie, S. Li, G. Biondini, A. Mussot, "Nonlinear stage of modulational instability", Progress In Electromagnetic Research Symposium (PIERS) Conference, Rome, Italy (2019).

Post-deadline paper in peer-reviewed international conference:

- A. Mussot, P. Szriftgiser, **C. Naveau**, A. Kudlinski, M. Conforti, F. Copie, and S. Trillo, "Observation of broken symmetry in the modulation instability recurrence", CLEO Europe/EQEC, Munich, Germany (2017)

The name of the speaker is in bold letters.

Abstract: This work deals with the investigation of the modulation instability process in optical fibres and in particular its nonlinear stage. This process can induce a complex coupling dynamics between the pump and sidebands waves, with a single or multiple returns to the initial state if it is seeded. This phenomenon is referred as Fermi-Pasta-Ulam-Tsingou recurrences. In this thesis, we describe the implementation of a novel experimental technique based on heterodyne optical time-domain reflectometry and active compensation of losses. It allows fast and non-invasive distributed characterisation along a fibre of the amplitude and phase of the main frequency components of a pulse. Furthermore, we detail a simple post-processing method which enable us to retrieve the complex field evolution in the time domain. Using these tools, we reported the observation of two Fermi-Pasta-Ulam-Tsingou recurrences and their symmetry-breaking nature, both in the frequency and time domain. Then, we quantitatively studied the influence of the initial three-wave input conditions on the recurrence positions, in regards with recent theoretical predictions. Finally, we investigated the dynamics of higher-order nonlinear structures, namely second-order breathers.

Keywords: nonlinear fiber optics; modulation instability,
Fermi-Pasta-Ulam-Tsingou recurrences, breathers

Résumé: Ce travail porte sur l'étude du processus d'instabilité de modulation dans les fibres optiques et notamment son étape nonlinéraire. Ce procesus peut induire une dynamique complexe de couplage nonlinéaire entre une onde de pompe et des bandes latérales, notamment un, voire de multiples, retours à l'état initial si il est amorcé activement. Ce phénomène est connu sous le nom de récurrences de Fermi-Pasta-Ulam-Tsingou. Dans cette thèse, nous décrivons la mise en place d'un montage expérimental se basant sur la déctection hétérodyne d'un signal rétrodiffusé et une compensation active des pertes. Il permet une caractérisation distribuée rapide et non-invasive tout le long d'une fibre de l'amplitude et la phase des principales composantes spectrales d'une impulsion. En outre, nous détaillons une méthode de post-traitement qui nous permet de retrouver l'évolution du champ complexe dans le domaine temporel. Mettant en oeuvre ces outils, nous avons rapporté l'observation de deux récurrences de Fermi-Pasta-Ulam-Tsingou et leur brisure de symétrie, à la fois dans les domaines fréquentiel et temporel. Suite à cela, nous avons quantitativement examiné l'influence des conditions initiales des trois ondes envoyées dans la fibre sur la position des récurrences, en comparaison avec de récentes prédictions théoriques. Finalement, nous avons étudié la dynamique de structures nonlinéraies d'orde supérieur, à savoir les breathers du deuxième ordre.

Mots-clés: optique nonlinéaire fibrée; instabilité de modulation; récurrences de Fermi-Pasta-Ulam-Tsingou, breathers